Title
Integration of biochemical and physical signals during directed cell migration

Permalink
https://escholarship.org/uc/item/4r48b0pn

Author
Brunetti, Rachel

Publication Date
2021

Peer reviewed|Thesis/dissertation

Integration of biochemical and physical signals during directed cell migration

by
Rachel Brunetti

DISSERTATION
Submitted in partial satisfaction of the requirements for degree of
DOCTOR OF PHILOSOPHY

in

Biophysics

in the

GRADUATE DIVISION
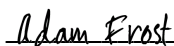of the
UNIVERSITY OF CALIFORNIA, SAN FRANCISCO

Approved:

Orion Weiner	
	Chair
David Drubin	
Sophie Dumont	
Adam Frost	
Manuel Leonetti	
	Committee Members

ACKNOWLEDGEMENTS

Graduate school has brought me full circle. College converted me from a biologist to a physicist and graduate school converted me from a physicist back to a biologist. Yet, I am far from where I started. I went from knowing little to knowing how little I actually know. Jokes aside, I am so grateful for the people I have shared this exciting and often humbling journey with.

First, I must thank Orion Weiner for shaping me into the scientist I am today. When applying to UCSF, Orion's lab was my top choice. However, when we met during interviews, I found that we had very different approaches to science. I was tool driven. In my own research, I used atomic force microscopy to probe cells the way others would probe asphalt. Meanwhile Orion was interested in the cells themselves and the tools as just that, tools to understand biology. Given this, I decided not to rotate in Orion's lab and ultimately found my way back only through the suggestion of my rotation mentors Steve Altschuler and Lani Wu. I got lucky. Not only did I have an amazing rotation where we made some truly transformative observations but I also found my home. Thank you Orion for seeing past that misguided interviewee and helping me realize what is means to be an interdisciplinary cell biologist. At the end of it all, I had a lot of fun in the lab. Thank you for creating an environment where learning and excitement are so intertwined.

Of course, this property does not just come from Orion but also from the people he attracts. There are so many great people in the Weiner lab who have helped me

did. Mom, thank you for distilling your love of learning. I have never met someone who consumes books like you do, and you have inspired me to be a life-long learner. Dad, you are my number one cheerleader. You are the least scientifically inclined of us and yet the most interested in hearing about my research. Thank you for pushing me forward when I doubted myself. Anna and Nikki, thank you for being my examples. Anna, you have taught me that anything is possible—like moving across the world and being completely self-sufficient. I am convinced you can do anything. Nikki, you are my second mom. I love that we had those typical sister fights but that I never had to doubt whether someone was in my corner. And Matt Wong, you belong here too. Thanks for choosing to be a part of my family.

STATEMENT REGARDING AUTHOR CONTRIBUTIONS

Chapter 2 is an updated manuscript draft of:

Anne Pipathsouk, Rachel M. Brunetti, Jason P. Town, Artù Breuer, Patrina A. Pellett, Kyle Marchuk, Ngoc-Han T. Tran, Matthew F. Krummel, Dimitrios Stamou, Orion D. Weiner. WAVE complex self-organization templates lamellipodial formation. bioRxiv. doi:10.1101/836585 (Preprint posted November 9, 2019).

This works was recently accepted for publication by the *Journal of Cell Biology*. Anne Pipathsouk conceived, designed, and performed the experiments and wrote the manuscript under the guidance of Orion Weiner. I assisted with initial super-resolution microscopy experiments and performed revision experiments under the guidance of Orion Weiner and Anne Pipathsouk. For the paper, I contributed endogenously-tagged HL-60 and HEK293T cell lines and prepared transgenic primary macrophages. These various lines are used in Figures 3E, 7, and S1 and S5. Jason Town performed image analysis and 3D imaging, Brian Graziano established the macrophage culturing in our lab and performed Western blots, Artù Breuer helped establish the HUVEC TEMs system, Patrina Pellett assisted with OMX SIM imaging, Kyle Marchuk assisted with lattice light sheet imaging, and Han Tran assisted with electron microscopy experiments. Orion Weiner and Dimitrios Stamou offered supervision and oversaw the manuscript.

Chapter 3 is a manuscript draft intended for publication:

Rachel M. Brunetti, Gabriele Kockelkoren, Preethi Raghavan, George R. R. Bell, Derek Briatin, Natasha Puri, Sean R. Collins, Manuel D. Leonetti, Dimitrios Stamou, Orion D.

Weiner. WASP links substrate topology and cell polarity to guide neutrophil migration. bioRixv. doi: 10.1101/2021.05.12.443722 (Preprint posted May 14, 2021).

I conceived, designed, and performed all experiments (excepting the STED) and wrote the manuscript under the guidance of Orion Weiner. Gabriele Kockelkoren performed all STED experiments and analysis, Preethi Raghavan significantly contributed to the method for endogenous tagging in HL-60 cells, George Bell provided cell lines and helped interpret experimental results, Derek Britain assisted with experimental design and microscopy, and Natasha Puri laid the foundations for our endogenous tagging in HL-60 cells. Orion Weiner, Dimitrios Stamou, Manuel Leonetti, and Sean Collins offered supervision and oversaw the manuscript. This work is currently under review.

Chapter 4 focuses on unpublished work using high-throughput endogenous tagging of HEK293T cells to determine the Rho GEFs and GAPs involved in cell polarity. I conceived, designed, and performed the experiments described under the guidance of Orion Weiner and Manuel Leonetti.

ABSTRACT

Integration of biochemical and physical signals during directed cell migration

Rachel Brunetti

Neutrophils are professional migrators within our body, moving from the bloodstream through dense forests of extracellular matrix to reach sites of infection and initiate an immune response. While we have long appreciated the role of biochemical signals in neutrophil recruitment, increasing attention is being given to the role of physical signals during this process. For example, membrane tension and membrane shape changes arise as neutrophils navigate complex 3D environments *in vivo*, which can impact the path cells take through tissue. However, how this information is relayed back to the cytoskeleton has remained largely unexplored. In this thesis we probe the link between biochemical and physical inputs to better understand how neutrophils integrate environmental signals to ensure robust directed migration.

In Chapter 2 we establish how intrinsic protein self-organization and external membrane curvature work together to pattern the actin nucleation promoting factor WAVE. Using super-resolution microscopy, we find that WAVE forms rings at the saddle-shaped necks of membrane invaginations in the absence of actin polymer. Dual inputs from WAVE's propensity to oligomerize and curvature sensitivity explain this enrichment pattern and inform our understanding of WAVE propagation in the presence of actin. Specifically, we find that WAVE localizes to the saddle-shaped lagging regions of the leading edge to support a uniformly advancing cell front. Elucidation of the mechanisms underpinning WAVE organization has provided initial insights into the integration of

internal biochemical signals with external cell shape in organizing the actin cytoskeleton.

In Chapter 3 we continue on this theme and highlight how WASP, another actin nucleation promoting factor, uses a modification of these behaviors to link cell shape and cell polarity during neutrophil migration. Unlike WAVE, WASP persistently enriches to substrate-induced invaginations in the presence of actin. Additionally, WASP assembles into focal structures rather than linear structures. We find that these properties allow WASP to link sites of local membrane deformation to the cytoskeleton by promoting actin polymerization and aligned migration in textured environments. Strikingly, this property requires concomitant inputs from cell shape and cell polarity. WASP only engages with curved membranes at the cell front, which supports forward advance. We show that WASP is essential for integration of substrate features with directed migration, which could have implications for migration through collagen meshworks *in vivo*.

Finally, Chapter 4 presents unpublished work exploring the molecular mechanisms of cell polarity through GTPase regulation by Rho GEFs and GAPs using HEK293T cells as a model system. Using CRISPR we endogenously label highly expressed GEFs and GAPs. We describe a system for polarizing HEK293T cells and report candidate GEFs and GAPs that enrich to induced cell protrusions. Finally, we supply a protocol for phenotyping the migration of HEK293T GEF or GAP knockout cell lines and provide a positive control in the form of Rac1 knockout. Ultimately, GEFs and GAPs exhibiting

loss of function phenotypes would be followed up in the consitituively polarized, highly

motile neutrophil cell line HL-60.

TABLE OF CONTENTS

LIST OF FIGURES

CHAPTER 2

CHAPTER 3

CHAPTER 4

LIST OF TABLES

CHAPTER 4

CHAPTER ONE

INTRODUCTION

Motile cells must balance different actin networks to achieve directed migration (Blanchoin et al., 2014). During migration, a cell produces an actin-rich front that supports forward locomotion while also maintaining other actin dependent processes like cargo uptake, trafficking, and secretion (Kaksonen et al., 2005). While we understand actin as a universal building block, *how* actin is assembled into functionally and morphologically distinct networks is unclear.

Branched actin organization is mediated by a class of proteins known as nucleation promoting factors, or NPFs. Different NPFs exhibit distinct spatial organizations that influence the shape of the actin networks they generate (Pollitt and Insall, 2009; Rottner et al., 2017). For example, the WAVE complex forms broad propagating waves that give rise to flat, lamellipodial actin networks (Weiner et al., 2007; Veltman et al., 2012; Leithner et al., 2016). Meanwhile, the NFPs WASP and N-WASP exhibit a punctate distribution that gives rise to finger-like actin networks suited for invasive structures like invadopodia (Yamaguchi et al., 2005; Yu and Machesky, 2012; Yu et al., 2012) and for the scission of endocytic vesicles (Kessels and Qualmann, 2002; Merrifield et al., 2004; Benesch et al., 2005). In this thesis we explore the organizing principles that pattern different NPFs and determine how the distinct distributions of NPFs can inform actin network shape and function.

NPFs involved in cell migration like WAVE and WASP sit in a polarized signaling cascade (Yang et al., 2016). The front-biased activity of their respective upstream Rho GTPases, Rac and Cdc42, are reflected in the cell-level localization of these NPFs.

However, these proteins exhibit unexplained local organization. Why does WAVE complex form ridges and WASP forms points when their upstream regulators form only broad, front-biased permissive zones? In this thesis we focus in on two possible hypotheses to explain this: self-organization and membrane curvature sensing.

First, in Chapter 2, we examine the effect of these factors on WAVE complex patterning. The WASP homologue N-WASP undergoes phase separation in cells and *in vitro* through multivalent interactions between its polyproline motifs and the SH3 domains of its binding partners (Li et al., 2012; Banjade and Rosen, 2014; Case et al., 2019). WAVE2 has similar polyproline stretches and shares many SH3 domain-containing binding partners with N-WASP (source: BIOGRID). It has been shown removal of actin-mediated recycling (via depolymerization of the actin cytoskeleton) causes the WAVE complex to accumulate as puncta on the cell membrane (Weiner et al., 2007). Therefore, does the WAVE complex similarly phase separate? Revisiting this experiment with super-resolution microscopy, we find that the WAVE complex does not appear to undergo phase separation but instead self-organizes into diffraction-limited rings. WAVE oligomerization could help explain its linear distribution and provide insight into how it patterns actin for lamellipod formation. We show that this self-organization is further templated by local membrane geometry. WAVE rings form at the saddle-shaped necks of membrane invaginations, which arise upon depolymerization of the actin cytoskeleton. Following from this observation, we find that WAVE complex transiently enriches to sites of saddle curvature in non-perturbed conditions – both at lagging regions of the leading edge and at transendothelial macroapertures. From this work we

conclude that self-organization and local membrane topology work together to pattern the WAVE complex and WAVE-dependent actin polymerization.

Given our observation that membrane curvature can inform the patterning of NPFs and their actin networks, we next sought to extend these findings to the NPF WASP (Chapter 3). Despite the phase separation of N-WASP, WASP behaves similar to WAVE upon depolymerization of the actin cytoskeleton and forms rings. While these rings could still be phase separated, they are diffraction-limited, making typical means of assaying this property (like fluorescence recovery after photobleaching and droplet merging (Brangwynne, 2009; Hyman et al., 2014)) difficult. Therefore, we leave the self-organization of WASP as an open question and instead choose to focus on whether membrane curvature affects WASP like it does WAVE. We find that WASP also enriches to sites of saddle curvature. However, WASP does not exhibit the self-extinguishing properties of WAVE complex and instead stably enriches to the necks of membrane invaginations in the presence of an intact actin cytoskeleton. We hypothesize that WASP's persistent enrichment could serve to couple environmental features (via local membrane deformation) with the cytoskeleton to support migration. Indeed, we find that WASP-null cells are defective at sensing the nanoscale features of their environment and exhibit defects when migrating on textured substrates. In this chapter we present differences in the preferred membrane features of WAVE and WASP, which may explain how these NPFs can take in similar signaling inputs yet yield morphologically and functionally distinct actin networks.

While we present membrane curvature sensitivity as a promising mechanism to pattern

NPFs, it does not appear to act alone. We observe that WASP curvature sensitivity is

modulated by its physical location within the cell; WASP only enriches to membrane

invaginations at the cell front. Recruitment of WASP therefore depends on both physical

inputs (membrane topology) as well as biochemical inputs (cell polarity). To further

probe the cooperativity between these types of inputs, we used CRISPR to target the

polarized Rho GTPase upstream of WASP. However, we find that Cdc42 is dispensable

for WASP polarity. While this result is surprising, it arises from the complexity of cell

polarity. Multiple Rho GTPases are polarized towards the front of motile neutrophils and

each can communicate with multiple NPFs. Additionally, we only superficially

understand the regulation of polarized GTPases, due in part to the expression of many

different regulators, including more than one hundred GEFs and GAPs. In the final part

of this thesis, we present initial results from a project aimed at elucidating the Rho GEFs

and GAPs involved in neutrophil polarity. Increased understanding of neutrophil polarity

establishment and maintenance can help us understand how GTPase signaling is

integrated with NPF membrane curvature sensitivity.

For this final project we leverage high rates of homology-directed repair in HEK293T

cells to endogenously tag ~50 highly expressed Rho GEFs and GAPs. We report a

method for polarizing HEK293T cells and use image arithmetic to detect GEF and GAP

enrichment to the cell membrane (active state) and to protrusions. We arrive at eight

candidate Rho GEFs and GAPs that enrich to the membrane/protrusions in polarized

HEK293T cells. This work is ongoing, but we provide an outline of next steps that

include overexpression of candidates in neutrophil-like HL-60 cells and targeted knockout of candidates that polarize. This project strives, through an unbiased CRISPR-based approach, to elucidate the Rho GEFs and GAPs that regulate cell polarity.

Through this thesis work, we investigate the organizing principles underlying NPF patterning and find that membrane topology sensing represents a promising mechanism that can both span and differentiate NPFs. Both WAVE and WASP enrich to sites of saddle curvature. However, WAVE transiently enriches to lagging regions of the leading edge and to transendothelial macroapertures to create lamelipodia while WASP persistently enriches to membrane invagination to leverage surface imperfections for advance. Surprisingly, we find that cell polarity influences WASP's curvature sensitivity. Additionally, we find that this behavior is independent of its upstream GTPase Cdc42. This observation challenges current models for WASP signaling (Rohatgi et al., 2000; Tsujita et al., 2015) and has inspired us to further explore polarized Rho GTPase regulation. We present candidate Rho GEFs and GAPs that may play a role in tuning cell polarity, which could, in turn, help us better understand the integration of this biochemical property with physical signals for actin patterning.

REFERENCES

Banjade, S., and M.K. Rosen. 2014. Phase transitions of multivalent proteins can promote clustering of membrane receptors. *Elife*. 3:e04123.

Benesch, S., S. Polo, F.P. Lai, K.I. Anderson, T.E.B. Stradal, J. Wehland, and K. Rottner. 2005. N-WASP deficiency impairs EGF internalization and actin assembly at clathrin-coated pits. *J. Cell Sci.* 118:3103–3115. doi:10.1242/jcs.02444.

Blanchoin, L., R. Boujemaa-Paterski, C. Sykes, and J. Plastino. 2014. Actin dynamics, architecture, and mechanics in cell motility. *Physiol. Rev.* 94:235–263. doi:10.1152/physrev.00018.2013.

Brangwynne, C.P. 2009. Germline P granules are liquid droplets that localize by controlled dissolution/condensation. *Science*. 324:1729–1732.

Case, L.B., X. Zhang, J.A. Ditlev, and M.K. Rosen. 2019. Stoichiometry controls activity of phase-separated clusters of actin signaling proteins. *Science*. 363:1093–1097. doi:10.1126/science.aau6313.

Hyman, A.A., C.A. Weber, and F. Julicher. 2014. Liquid-liquid phase separation in biology. *Annu. Rev. Cell Dev. Biol.* 30:39–58.

Kaksonen, M., C.P. Toret, and D.G. Drubin. 2005. A modular design for the clathrin- and actin-mediated endocytosis machinery. *Cell*. 123:305–320. doi:10.1016/j.cell.2005.09.024.

Kessels, M.M., and B. Qualmann. 2002. Syndapins integrate N-WASP in receptor-mediated endocytosis. *EMBO J.* 21:6083–94. doi:10.1093/emboj/cdf604.

Leithner, A., A. Eichner, J. Müller, A. Reversat, M. Brown, J. Schwarz, J. Merrin, D.J.J. de Gorter, F. Schur, J. Bayerl, I. de Vries, S. Wieser, R. Hauschild, F.P.L. Lai, M.

Moser, D. Kerjaschki, K. Rottner, J.V. Small, T.E.B. Stradal, and M. Sixt. 2016. Diversified actin protrusions promote environmental exploration but are dispensable for locomotion of leukocytes. *Nat. Cell Biol.* 18:1253–1259. doi:10.1038/ncb3426.

Li, P., S. Banjade, H.-C. Cheng, S. Kim, B. Chen, L. Guo, M. Llaguno, J. V. Hollingsworth, D.S. King, S.F. Banani, P.S. Russo, Q.-X. Jiang, B.T. Nixon, and M.K. Rosen. 2012. Phase transitions in the assembly of multivalent signalling proteins. *Nature*. 483:336–340. doi:10.1038/nature10879.

Merrifield, C.J., B. Qualmann, M.M. Kessels, and W. Almers. 2004. Neural Wiskott Aldrich Syndrome Protein (N-WASP) and the Arp 2/3 complex are recruited to sites of clathrin-mediated endocytosis in cultured fibroblasts. *Eur. J. Cell Biol.* 83:13–18. doi:10.1078/0171-9335-00356.

Pollitt, A.Y., and R.H. Insall. 2009. WASP and SCAR/WAVE proteins: the drivers of actin assembly. *J. Cell Sci.* 122:2575–2578. doi:10.1242/jcs.023879.

Rohatgi, R., H.Y.H. Ho, and M.W. Kirschner. 2000. Mechanism of N-WASP activation by CDC42 and phosphatidylinositol 4,5-bisphosphate. *J. Cell Biol.* 150:1299–1309. doi:10.1083/jcb.150.6.1299.

Rottner, K., J. Faix, S. Bogdan, S. Linder, and E. Kerkhoff. 2017. Actin assembly mechanisms at a glance. *J. Cell Sci.* 130:3427–3435. doi:10.1242/jcs.206433.

Tsujita, K., T. Takenawa, and T. Itoh. 2015. Feedback regulation between plasma membrane tension and membrane-bending proteins organizes cell polarity during leading edge formation. *Nat. Cell Biol.* 17:749–758. doi:10.1038/ncb3162.

Veltman, D.M., J.S. King, L.M. Machesky, and R.H. Insall. 2012. SCAR knockouts in
Dictyostelium: WASP assumes SCAR's position and upstream regulators in
pseudopods. *J. Cell Biol.* 198:501–508. doi:10.1083/jcb.201205058.

Weiner, O.D., W.A. Marganski, L.F. Wu, S.J. Altschuler, and M.W. Kirschner. 2007. An
actin-based wave generator organizes cell motility. *PLoS Biol.* 5:e221.
doi:10.1371/journal.pbio.0050221.

Yamaguchi, H., M. Lorenz, S. Kempiak, C. Sarmiento, S. Coniglio, M. Symons, J.
Segall, R. Eddy, H. Miki, T. Takenawa, and J. Condeelis. 2005. Molecular
mechanisms of invadopodium formation: The role of the N-WASP-Arp2/3 complex
pathway and cofilin. *J. Cell Biol.* 168:441–452. doi:10.1083/jcb.200407076.

Yang, H.W., S.R. Collins, and T. Meyer. 2016. Locally excitable Cdc42 signals steer
cells during chemotaxis. *Nat. Cell Biol.* 18:191–201. doi:10.1038/ncb3292.

Yu, X., and L.M. Machesky. 2012. Cells assemble invadopodia-like structures and
invade into matrigel in a matrix metalloprotease dependent manner in the circular
invasion assay. *PLoS One*. 7:e30605. doi:10.1371/journal.pone.0030605.

Yu, X., T. Zech, L. McDonald, E.G. Gonzalez, A. Li, I. Macpherson, J.P. Schwarz, H.
Spence, K. Futó, P. Timpson, C. Nixon, Y. Ma, I.M. Anton, B. Visegrády, R.H.
Insall, K. Oien, K. Blyth, J.C. Norman, and L.M. Machesky. 2012. N-WASP
coordinates the delivery and F-actin-mediated capture of MT1-MMP at invasive
pseudopods. *J. Cell Biol.* 199:527–544. doi:10.1083/jcb.201203025.

CHAPTER TWO

THE WAVE COMPLEX ASSOCIATES WITH SITES OF SADDLE MEMBRANE CURVATURE

SUMMARY

How local interactions of actin regulators yield large-scale organization of cell shape and movement is not well understood. Here we investigate how the WAVE complex organizes sheet-like lamellipodia. Using super-resolution microscopy, we find that the WAVE complex forms actin-independent 230 nanometer-wide rings that localize to regions of saddle membrane curvature. This pattern of enrichment could explain several emergent cell behaviors, such as expanding and self-straightening lamellipodia and the ability of endothelial cells to recognize and seal transcellular holes. The WAVE complex recruits IRSp53 to sites of saddle curvature but does not depend on IRSp53 for its own localization. Although the WAVE complex stimulates actin nucleation via the ARP2/3 complex, sheet-like protrusions are still observed in ARP2-null, but not WAVE complex-null, cells. Therefore, the WAVE complex has additional roles in cell morphogenesis beyond ARP2/3 complex activation. Our work defines organizing principles of the WAVE complex lamellipodial template and suggests how feedback between cell shape and actin regulators instructs cell morphogenesis.

INTRODUCTION

Cells manipulate the shape of their plasma membranes to execute physiological

functions ranging from building the protrusions that drive cell motility to coordinating the

membrane deformations that enable endocytosis. Actin polymerization plays a major

role in coordinating these processes, but how cells specify the proper pattern of actin

assembly to achieve these distinct shapes is not known. Cells use nucleation promoting

factors (NPFs) to spatially and temporally control their patterns of actin polymerization

(Takenawa and Suetsugu, 2007; Chesarone and Goode, 2009). For example, neural

Wiskott-Aldrich syndrome protein (N-WASP) and WASP-family verprolin homologous

protein (WAVE) activate the actin-related protein 2/3 (ARP2/3) complex to seed actin

nucleation (Machesky and Insall, 1998; Pollard and Borisy, 2003; Machesky et al.,

1999).

N-WASP and WAVE are nested in similar signaling topologies — both are stimulated by

phosphoinositides, Rho GTPases, and curvature-sensitive Bin-amphiphysin-Rvs (BAR)

domain proteins, both activate the ARP2/3 complex, both are recycled in an actin-

dependent fashion, and both show evidence of oligomerization at the membrane

(Takenawa and Suetsugu, 2007; Pollard and Borisy, 2003; Rohatgi et al., 1999; Oikawa

et al., 2004; Weiner et al., 2007; Ho et al., 2004; Koronakis et al., 2011; Suetsugu et al.,

2006; Abou-Kheir et al., 2008; Etienne-Manneville and Hall, 2002) (Fig. 1A). Despite

these similarities, the morphological structures they build are distinct: N-WASP typically

participates in spiky filopodial protrusions, invadopodia, and endocytic vesicles

(Takenawa and Suetsugu, 2007; Miki et al., 1998; Bu et al., 2009; Naqvi et al., 1998;

Yamaguchi et al., 2005; Yu and Machesky, 2012; Yu et al., 2012; Benesch et al., 2005; Taylor et al., 2011; Veltman et al., 2012), whereas WAVE participates in broad, sheet-like lamellipodial protrusions (Hall, 1998; Weiner et al., 2006; Leithner et al., 2016; Graziano et al., 2019). Though these are their typical actin structures, WASP can compensate for the lack of Scar/WAVE in building lamellipodia in some cell types like Dictyostelium (Veltman et al., 2012; Zhu et al., 2016), but not in neutrophils or dendritic cells (Graziano et al., 2019; Leithner et al., 2016). The rules for instructing filopodial versus lamellipodial cell morphologies are not understood.

Biochemical reconstitutions have provided insights into how different patterns of actin nucleation lead to different morphological structures. Activation of the ARP2/3 complex in the absence of membranes produces a branched dendritic morphology (Mullins et al., 1998). Activation of the ARP2/3 complex on the surface of giant unilamellar vesicles produces filopodial-like structures (Liu et al., 2008). In contrast, spatially organizing ARP2/3 complex activation in a linear geometry via glass rods (Carlier et al., 2003) or UV micropatterned surfaces (Boujemaa-Paterski et al., 2017) produces lamellipodial-like structures. These data suggest that while spiky, finger-like actin structures are the default morphology for the ARP2/3 complex activation on membranes, lamellipodium formation requires a linear structural template of actin nucleators (Fritz-Laylin et al., 2017b). What forms the basis of the linear template for lamellipodia in living cells is not known.

In cells, N-WASP forms the focal structure expected for finger-like protrusions (Yu et al., 2012; Benesch et al., 2005; Case et al., 2019), and the WAVE complex propagates as linear waves at the edges of lamellipodia (Weiner et al., 2007; Fritz-Laylin et al., 2017a; Steffen et al., 2004; Davidson et al., 2018; Hahne et al., 2001; Huang et al., 2013; Zallen et al., 2002; Leithner et al., 2016). In the case of N-WASP, biochemical reconstitutions recapitulate its in vivo distribution: N-WASP and its multivalent binding partners generate biomolecular condensates (Case et al., 2019; Banjade and Rosen, 2014) that result in focal accumulation of the nucleator. In the presence of the ARP2/3 complex and actin, these puncta-shaped condensates promote focal bursts of F-actin that produce spiky protrusions (Banjade and Rosen, 2014). In contrast, we do not know the basis of the WAVE complex's linear organization in cells (Fig. 1B).

The WAVE complex is required for proper cell migration and regulation of cell shape across eukaryotes including mammals, amoeba, and plants (Pollard and Borisy, 2003; Weiner et al., 2007; Leithner et al., 2016; Fritz-Laylin et al., 2017a; Ibarra et al., 2006; Szymanski, 2005; Rakeman and Anderson, 2006; Kunda et al., 2003). As a pentameric heterocomplex, the WAVE complex contains the subunits WAVE/SCAR, Abi, HSPC300, Sra1/Cyfip1, and Nap1/Hem1 (Weiner et al., 2006; Eden et al., 2002; Innocenti et al., 2004). In neutrophils and other motile cells, the dynamics of the WAVE complex closely corresponds to the leading edge's morphology and pattern of advance (Weiner et al., 2007; Steffen et al., 2004; Davidson et al., 2018; Hahne et al., 2001; Huang et al., 2013; Zallen et al., 2002; Leithner et al., 2016; Fritz-Laylin et al., 2017a). The WAVE complex is required for the formation of lamellipodia and efficient chemotaxis in a range of

immune cells (Weiner et al., 2006; Leithner et al., 2016; Graziano et al., 2019; Park et al., 2008; Evans et al., 2013; Kheir et al., 2005).

Here, we investigate the features of WAVE complex organization that may instruct the generation and dynamics of lamellipodia. Using super-resolution microscopy, we find that the WAVE complex forms actin-independent 230 nanometer-wide rings that localize to regions of saddle membrane curvature. To identify a potential mechanism of membrane curvature recognition, we explored the WAVE complex's partnering interactions with IRSp53, an inverse BAR domain protein, and found that IRSp53 depends on its interactions with the WAVE complex to recognize lamellipodial and saddle curvature geometries, but the WAVE complex can localize to these structures without IRSp53. While WAVE complex-null cells fail to form sheet-like protrusions, ARP2/3-disrupted cells can do so, highlighting the central role of the WAVE complex in this process. We propose that the WAVE complex's nanoscale organization could explain emergent behaviors of cell morphogenesis including expanding and self-straightening lamellipodia and the recognition and closure of transcellular holes.

RESULTS

The WAVE complex forms nanoscale, oligomeric rings in the absence of actin polymer

In neutrophil-like dHL60 cells and a range of other motile cells, the WAVE complex can be seen propagating as a linear "wave" structure at the edges of membrane ruffles and lamellipodia (Oikawa et al., 2004; Weiner et al., 2007; Veltman et al., 2012; Leithner et al., 2016; Rakeman and Anderson, 2006) (Fig. 1C, Video 1). This dynamic propagation arises from an excitable feedback network with positive feedback (WAVE complex recruits more WAVE complex) and negative feedback loops (WAVE complex stimulates actin polymerization, which inhibits WAVE complex's association with the membrane) (Weiner et al., 2007; Millius et al., 2012). One source of negative feedback is the force of actin polymerization that strips the WAVE complex off the plasma membrane (Millius et al., 2012). In contrast, the mechanism and spatial organization of positive feedback, i.e. WAVE complex recruiting more WAVE complex, are not well understood. We were particularly interested in understanding whether the linear patterns of the WAVE complex in lamellipodia are dependent on an interaction between these positive and negative feedback loops, as is the case for other excitable networks (Allard and Mogilner, 2013), or whether the WAVE complex's oligomerization at the plasma membrane has a specific geometric organization in the absence of the actin-based negative feedback loop (Fig. 2A). We can use inhibitors of actin polymerization to deplete F-actin to distinguish between the two models.

When we previously visualized the pattern of the WAVE complex organization (via fluorescently-tagged hematopoietic protein 1 [Hem1], a subunit of the WAVE complex)

16

in the absence of the actin cytoskeleton, standard total internal reflection fluorescence (TIRF) microscopy showed amorphous punctate structures of the WAVE complex (Weiner et al., 2007). For our current study, we revisited this experiment with super-resolution microscopy, specifically TIRF-structured-illumination microscopy (TIRF-SIM), a technique that enables a 2-fold increase in resolution in the TIRF plane. When the F-actin inhibitor latrunculin A was acutely added to dHL60 cells to deplete F-actin, TIRF-SIM imaging of Hem1-eGFP revealed that the WAVE complex organizes into highly stereotyped 230 nm-wide ring structures (Fig. 2B-D, Video 2). Importantly, super-resolution microscopy was required to resolve the nanometer-scale rings because they otherwise appear as amorphous blob-like structures by conventional TIRF (Fig. 2C). The WAVE complex rings were not an artifact of overexpressing a tagged subunit, as any subunit protein not incorporated into the multiprotein complex gets degraded (Fig. S1A) (Kunda et al., 2003; Weiner et al., 2006; Litschko et al., 2017; Graziano et al., 2019). Moreover, endogenously labeled WAVE2 also formed rings upon F-actin inhibition (Fig. S1B-C). Furthermore, the WAVE complex rings are devoid of F-actin: phalloidin staining of cells treated with latrunculin show that the rings lack detectable residual filamentous actin (Fig. S1D).

The WAVE complex rings were observed across a range of F-actin inhibitors and concentrations (Fig. S2A-B), super-resolution modalities (Fig. S2C), tagged fluorescent proteins (Fig. S2D), cell types, and specific WAVE complex subunits (Fig. S2E). The rings may represent the favored oligomeric organization of the WAVE complex when freed from the constraints of the cytoskeleton and/or tension in the plasma membrane

(Diz-Muñoz et al., 2016; Lieber et al., 2013). These experiments suggest that the WAVE complex forms nanoscale, F-actin-free, oligomeric rings at the plasma membrane.

The formation of WAVE complex rings is dependent on upstream signals

While WAVE complex activation is dependent on upstream regulators (Lebensohn and Kirschner, 2009; Leng et al., 2005), it was unclear whether these activators are also required for its formation of nanoscale rings (Fig. 3A). We found that stimulation of F-actin inhibited cells with chemoattractant increased the membrane-bound WAVE complex signal, indicating facilitation by chemoattract receptor-mediated activation (Fig. 3B). To test the role of Rho GTPases (Rac, Cdc42, and Rho), we inhibited them all by treating cells with Clostridium difficile toxin B (Just et al., 1995) and found that the number of the WAVE complex rings formed after F-actin inhibition decreased significantly (Fig. 3C). Furthermore, Pak-PBD, a biomarker for active Rac, broadly spatially overlaps with the WAVE complex's discrete localization (Fig. 3D), potentially representing a permissive zone for WAVE complex recruitment. These data suggest that WAVE collaborates with upstream activators such as Rac in forming rings. We also explored whether the WAVE complex rings are templated by other ring-forming proteins such as clathrin and septins. Neither clathrin rings nor septin rings significantly colocalized with the WAVE complex rings (Fig. 3E-F). Strikingly, septins and the WAVE complex have mutually exclusive localization at the cell periphery (Fig. 3F), potentially representing complementary curvature preferences.

WAVE complex rings associate with saddle-shaped membrane geometry

Next, we wondered how these WAVE complex rings are organized relative to the

morphology of the plasma membrane. During cell migration, the WAVE complex is

closely associated with the propagating edge of lamellipodial protrusions (Fig. 1C). Dual

imaging of the WAVE complex and the plasma membrane in the absence of F-actin

revealed that the WAVE complex rings localized to the boundary where coverslip-

opposed membrane leaves the TIRF field (Fig. 4A, Video 3). This membrane

distribution suggests an association of the WAVE complex to the necks of membrane

invaginations (Fig. 4B), and electron microscopy experiments are consistent with this

plasma membrane geometry (Galkina et al., 2018) (Fig. 4C-D). Although we do not

know the molecular composition of these invaginations, the WAVE complex's propensity

to enrich around the necks of plasma membrane invaginations may give insight into its

membrane geometry preferences. The necks of membrane invaginations exhibit saddle

curvature: principal curvatures that are positive in one axis (the curve around the

invagination neck) and negative in the other axis (the curve perpendicular to the

invagination neck) (Fig. 4E). Intriguingly, the negative curvature at the neck of an

invagination is comparable to that at the tip of a protrusion (Fig. 4F). In addition to

upstream activators, saddle membrane geometry could potentially be another factor to

proper WAVE complex localization.

The WAVE complex enriches to saddle-shaped transendothelial tunnels

To further explore the possible role of saddle curvature recognition in the emergent

control of cell shape, we took advantage of transendothelial cell macroaperture tunnel

physiology. As leukocytes undergo diapedesis out of the blood vessel, they can migrate either in between endothelial cells or they can generate a transendothelial cell macroaperture, a transcellular hole, to migrate through endothelial cells (Carman and Springer, 2008). To heal the transcellular hole and prevent pathogen dissemination, the affected endothelial cell seals the macroaperture (Boyer et al., 2006; Lemichez et al., 2010; Maddugoda et al., 2011). The sealing process requires the recognition of the macroaperture, which exhibits saddle curvature, and subsequent closure of the hole (Maddugoda et al., 2011) (Fig. 5A). Closure is an ARP2/3 complex-mediated process, but the relevant ARP2/3 complex activator has not been identified (Maddugoda et al., 2011; Ng et al., 2017).

To study transendothelial cell macroapertures (TEMs), we imaged the WAVE complex (via fluorescently-tagged Nap1, a homologue of Hem1) in HUVECs (Carman and Springer, 2008; Maddugoda et al., 2011; Boyer et al., 2006; Ng et al., 2017) and found that it enriched to closing transendothelial cell macroapertures (Fig. 5B, Video 4). This is another example of the WAVE complex's association to saddle membrane geometry. An advantage of the transendothelial cell macroaperture saddle system is that it maintains a fixed lamellipodial-like negative curvature in the Z-plane while it scans a range of positive curvatures throughout its closure (Maddugoda et al., 2011; Stefani et al., 2017). Therefore, we can use this range of hole sizes to evaluate the positive curvature preference for the WAVE complex (Fig. 5C). A saddle geometry sensor presented with fixed negative curvature in one axis and a range of positive curvatures in the other axis would increase its local concentration until the TEM closure reaches the

sensor's preferential positive curvature. From analyzing the WAVE complex signal throughout TEM closure, its local concentration per unit TEM perimeter increases at a rate significantly different from that of the membrane (Fig. 5D-E). The WAVE complex's progressive enrichment to smaller and smaller transendothelial cell macroapertures suggests that it can tolerate a range of positive curvatures but prefers smaller positive curvatures; this is consistent with our initial finding that the WAVE complex spontaneously forms sub-diffraction rings upon actin depolymerization (Fig. 2).

Furthermore, we found that the WAVE complex enrichment correlates with membrane velocity; regions of membrane with more WAVE complex correlate with higher velocity for both advancing neutrophil leading edges and closing transendothelial macroapertures (Fig. S3A-B). As membranes protrude in these cases, some regions may transiently fall behind or "lag." In order to maintain a coherent advancing front, the lagging portion, which exhibits positive curvature, must become less positively curved, i.e. flatten/straighten, and accelerate to "catch up." The WAVE complex preferentially enriches to transendothelial macroaperture membrane regions that are flattening compared to those that are becoming more curved (Fig. S3C). These data suggest that the WAVE complex prefers nanoscale saddle geometry in a range of cellular and physiological contexts and support a self-straightening role for WAVE-mediated protrusions.

The WAVE complex recruits IRSp53 to lamellipodia and saddle curvature
Next, we sought to understand how the WAVE complex localizes to saddle geometries.

Though the WAVE complex has membrane-binding motifs (Oikawa et al., 2004), it lacks

any well-characterized curvature sensing motifs. However, the WAVE complex does

directly interact with IRSp53 (insulin receptor tyrosine kinase substrate protein of 53

kDa; human ortholog is BAIAP2 [brain-specific angiogenesis inhibitor 1-associated

protein 2]), a member of the inverse BAR (I-BAR) domain family of curvature-sensitive

proteins that associates with lamellipodia and filopodia (Suetsugu et al., 2006; Abou-

Kheir et al., 2008; Miki et al., 2000; Scita et al., 2008; Frost et al., 2009; Zhao et al.,

2011; Mattila et al., 2007) (Fig. 6A).

To compare their localization patterns, we imaged IRSp53 and the WAVE complex in

dHL60 cells. Full-length IRSp53 localized to multiple areas of negative curvature:

lamellipodia (Suetsugu et al., 2006; Abou-Kheir et al., 2008; Miki et al., 2000; Nakagawa

et al., 2003; Robens et al., 2010), filopodia-like tubules (Nakagawa et al., 2003; Robens

et al., 2010; Krugmann et al., 2001; Sudhaharan et al., 2019), and rings (Figs. 6B, S4A).

IRSp53 and the WAVE complex only co-localized at protruding lamellipodia during cell

migration; WAVE complex was absent at filopodial-like tubules (Fig. 6B top, Video 5).

When cells were treated with a F-actin inhibitor, both the WAVE complex and IRSp53

co-localized to rings (Fig. 6B bottom), consistent with both proteins showing saddle

curvature enrichment. Strikingly, high expression of IRSp53 induces ring structures

even without F-actin inhibition (Fig. S4A, Video 6), suggesting a potential functional

interaction of these two proteins at sites of saddle curvature. IRSp53 rings (+/- F-actin

inhibitor) had comparable diameters to the WAVE complex rings (+ F-actin inhibitor)

(Fig. S4B). This characteristic size suggests a preferred geometry for IRSp53 and the

WAVE complex's membrane recruitment in cells. While IRSp53 localized to multiple sites displaying negative curvature, the WAVE complex was specifically enriched to lamellipodia and regions of saddle curvature.

Since the WAVE complex and IRSp53 colocalize in a subset of cell structures, we wondered whether IRSp53's localization pattern may be partially dependent on its interactions with the WAVE complex. IRSp53 consists of several functional domains that could contribute to its localization, in particular an I-BAR domain that senses negative curvature and an SH3 domain that interacts with the WAVE complex (Suetsugu et al., 2006; Abou-Kheir et al., 2008; Miki et al., 2000). To investigate how these domains contribute to the overall pattern of IRSp53 enrichment, we generated two structure/function constructs tagged with eGFP at the C-terminus: an "I-BAR" only domain that consisted of IRSp53's first 250 amino acids and a "C-term" only construct that lacks the I-BAR domain but contains the region that interacts with the WAVE complex (Figs. 6A, S4C). In chemoattractant stimulated cells, full-length IRSp53 enriched to both lamellipodia and filopodia-like structures, the I-BAR domain preferentially enriched to filopodia-like structures, and the C-term domain remained cytosolic (Fig. 6C). In F-actin inhibited cells, full-length IRSp53 formed rings, whereas the I-BAR and C-term constructs failed to enrich as rings (Fig. 6D). These data suggest that IRSp53 requires both its I-BAR domain and its C-terminal portion, containing its SH3-WAVE complex interacting domain, to properly enrich to lamellipodia and saddle points.

Since IRSp53's SH3 domain interacts with other actin regulators besides the WAVE complex (including Mena (Krugmann et al., 2001), Eps8 (Disanza et al., 2006), and mDia1 (Goh et al., 2012)), we tested whether IRSp53's localization patterns are dependent on the WAVE complex by imaging full-length IRSp53 in WAVE complex-null cells. The WAVE complex was depleted via CRISPR/Cas9-mediated knock out of Hem1, which resulted in the depletion of the other subunits (Leithner et al., 2016; Graziano et al., 2019; Litschko et al., 2017). Upon F-actin inhibition, full-length IRSp53 failed to robustly form rings in the WAVE complex-null cells (Fig. 6E). These data suggest that while IRSp53's I-BAR domain is sufficient to enrich to filopodia-like structures, IRSp53 requires its I-BAR domain and its interactions with the WAVE complex to localize to lamellipodia and saddle geometries. Our data highlights how proteins can partner together to sense complex geometries.

To probe the generality of IRSp53 requiring both its I-BAR domain and its ability to bind to the WAVE complex to sense saddle curvature, we returned to the HUVEC transendothelial cell macroaperture system. A previous study found that IRSp53's isolated I-BAR domain fails to recognize transendothelial cell macroapertures (Maddugoda et al., 2011), and we confirmed these results in our hands (Fig. S4D, Video 4). This is consistent with our observation that the isolated I-BAR construct failed to enrich saddle-shaped membrane invaginations in dHL60s (Fig. 6D). Because full-length IRSp53 recognized saddle curvature in dHL60 cells (Fig. 6D), we expected that full-length IRSp53 would also recognize transendothelial cell macroapertures, and our

observations are consistent with this hypothesis (Fig. S4D, Video 4). These data show that IRSp53 depends on its ability to interact with the WAVE complex to localize to saddle geometries in a range of cellular contexts.

Which WAVE effectors are essential to instruct lamellipodial assembly?

The WAVE complex has several effectors and associated proteins it could use to instruct lamellipodial assembly (Fig. 1A). Here we investigate the role of two such effectors (IRSp53 and the ARP2/3 complex) in lamellipodial formation. IRSp53 requires the WAVE complex to localize to lamellipodia and saddle geometries (Fig. 6C-E). To test whether the converse is true, we imaged the WAVE complex in dHL60 cells following CRISPR/Cas9-mediated knock out of IRSp53 (Fig. S4E). The absence of IRSp53 did not affect the ability of the WAVE complex to localize to lamellipodia or alter the number or size of WAVE complex rings following actin depolymerization (Fig. 6F). These data suggest that the WAVE complex does not depend on its partnering interactions with IRSp53 to localize to lamellipodia and saddle curvature. We do not know if other I-BAR proteins are involved in recruiting the WAVE complex to sites of saddle curvature or if other mechanisms are at play.

Though it is known that the WAVE complex is required to form sheet-like protrusions (Weiner et al., 2006; Leithner et al., 2016; Graziano et al., 2019), it is unclear what aspect of the WAVE complex activity is essential. One of the most well-established links from the WAVE complex to the actin cytoskeleton is its activation of the ARP2/3 complex (Machesky and Insall, 1998; Pollard and Borisy, 2003; Weaver et al., 2003);

25

though the WAVE complex has other ARP2/3 complex-independent links to actin

polymerization (Bieling et al., 2018). To investigate the necessity of this link for sheet-

like protrusions, we compared the TIRF-SIM localization of IRSp53, a marker of both

filopodial and lamellipodial protrusions, in chemoattractant-stimulated WAVE complex-

null and ARP2-null dHL60 cells (Graziano et al., 2019) (Fig. 7A-B, Video 7) as well as in

Arpc2-/- primary mouse bone marrow macrophages (Rotty et al., 2017) (Fig. 7C-D,

Video 8). Depletion of the WAVE complex resulted in the loss of broad, protrusive

lamellipodia structures (Fig. 7A middle). In contrast, cells with ARP2/3 complex

disrupted still form sheet-like structures (Fig. 7A bottom) in which the WAVE complex

localizes to the protruding edges (Fig. 7E, Video 9) ahead of F-actin-rich accumulations

(Fig. 7F). The ARP2-null sheet-like protrusions extend more slowly compared to

wildtype protrusions (Fig. 7B), suggesting that the ARP2/3 complex contributes to the

rate of lamellipodial advancement. To test the generality of the ability of cells to build

sheet-like protrusions in the absence of the Arp2/3 complex, we imaged IRSp53 in

primary macrophages that have an Arpc2/p34 subunit conditional allele (Rotty et al.,

2015, 2017) (Fig. 7C, Video 8). When the macrophages were treated with 4-OHT to

induce the CreER dependent deletion of Arp2c, we observed elongated cell

morphologies that also formed sheet-like protrusions that extend slowly compared to

wildtype cells (Fig. 7C-D). The difference in morphology between WAVE complex-null

and ARP2/3-disrupted cells suggests that the WAVE complex has roles in sheet-like

protrusion formation beyond its activation of the ARP2/3 complex, possibly reflecting the

actin polymerase role of the WAVE complex (Bieling et al., 2018).

To further probe the WAVE complex's Arp2/3 complex-independent roles, we generated an endogenous WAVE2ΔVCA split-GFP knock-in HEK-293T cell line (Fig. S5A-B). We found that WAVE2ΔVCA localizes to the leading edge of sheet-like protrusions (Fig. S5C, Video 10), thus highlighting the WAVE complex's central role in organizing lamellipodia beyond its connection to the Arp2/3 complex.

DISCUSSION

The WAVE complex assembles into a linear, curved oligomer at sites of saddle membrane curvature

In this work, we investigated how the WAVE complex achieves the proper spatial organization for building lamellipodia. We found that the WAVE complex assembles into highly ordered nanoscale rings in the absence of actin polymer (Fig. 2). The WAVE complex rings are dependent on upstream regulators like Rac (Fig. 3) Furthermore, the rings associate with regions of saddle curvature at the plasma membrane (Fig. 4). The WAVE complex's enrichment to membrane saddles is also apparent in closing transendothelial cell macroapertures (Fig. 5). IRSp53 requires its interactions with the WAVE complex to localize to lamellipodia, membrane invaginations, and transendothelial cell macroapertures, but the converse is not true (Fig. 6). Furthermore, sheet-like protrusions form in ARP2/3 complex-disrupted cells but not in WAVE complex-null cells (Fig. 7). This suggests that the WAVE complex's link to lamellipodial assembly is not limited to the activation of the ARP2/3 complex, underscoring the central role of the WAVE complex in generating lamellipodia. The WAVE complex's association with saddle-shaped membrane coupled with its regulation of actin polymerization likely forms the basis for emergent self-organizing behaviors like cell morphogenesis during migration and closure of transcellular holes.

How the WAVE complex achieves its oligomeric association into stereotyped 230 nm rings is unknown. There is no evidence that the purified WAVE complex oligomerizes on its own (Chen et al., 2010). Even in the presence of its known coactivators and with a

complete motility mix (or even the presence of cytosol), there have been no WAVE

complex rings, lines, propagating dynamics, or self-organizing lamellipodia observed

(Koronakis et al., 2011; Lebensohn and Kirschner, 2009; Chen et al., 2010). It is likely

that the WAVE complex requires its interacting partners to form higher-order oligomers,

as is the case for N-WASP (Case et al., 2019; Banjade and Rosen, 2014). It is possible

that the same proteins that activate the nucleation ability of the WAVE complex, such as

phosphoinositides, Rac, and Arf (Koronakis et al., 2011; Lebensohn and Kirschner,

2009; Suetsugu et al., 2006; Chen et al., 2017) or post-translational modifications of the

complex (Ura et al., 2012; Mendoza et al., 2011; Singh and Insall, 2021) may be

needed to activate WAVE complex oligomerization. Consistent with this idea, we

observe an increase in WAVE complex rings following chemoattractant stimulation of

latrunculin-treated cells (Fig. 3B) and Rho family GTPase inhibition inhibits WAVE

complex ring formation (Fig. 3C).

The WAVE complex's oligomerization into rings may contribute to how it recognizes

sites of plasma membrane saddle geometry. Given the stereotypical ring diameter of

230 nm (Fig. S2), the enrichment to membrane saddles with near-diffraction-limited

curvature in the positive axis for closing transendothelial cell macroapertures (Fig. 5E),

and the overexpression of IRSp53 generating similarly sized rings in the presence of an

intact actin cytoskeleton (Fig. S4A-B), these data are consistent with a radius of positive

curvature preference of 115 nm. What is the dimension of the WAVE complex rings in

the negative curvature axis? Although we cannot visualize this directly in our TIRF-SIM

images of F-actin inhibited cells (negative curvature axis is in the Z-plane where TIRF

provides no information), our electron microscopy imaging of membrane invaginations gives a height estimate of ~130 nm, which is consistent with the negative curvature of the edge of lamellipodia in our work (Fig. 4F) and others' work (Abercrombie et al., 1970; Abraham et al., 1999; Urban et al., 2010), and in agreement with the at most ~100 nm resolution of TIRF-SIM imaging of propagating WAVE complex in non-F-actin inhibited cells. This data suggest a radius of negative curvature preference of 65 nm.

Ring formation has been observed for other proteins that sense plasma membrane curvature. For example, septins form rings in vivo following treatment with actin destabilizing drugs, and purified septins form similarly-sized rings in vitro (Kinoshita et al., 2002). The radius of curvature of septin rings reflects septins' intrinsic curvature preference both in vitro and in vivo (Kinoshita et al., 2002; Bridges et al., 2016). Similar to septins, the WAVE complex also forms ring structures upon actin depolymerization, and these rings associate with curved membranes, although the WAVE complex rings fail to colocalize with septin rings (Fig. 3F). Thus, it is possible that the geometry of the WAVE complex's nanoscale rings may predict the WAVE complex's preferred geometry. Whereas septins' curved oligomerization and curvature preference has been shown for purified proteins, this has not been demonstrated for purified WAVE complex (WAVE complex does not oligomerize on its own (Chen et al., 2010). Future experiments will be needed to determine whether the geometry of oligomerization and/or other curvature-sensitive binding partners, and potentially in association with the WAVE complex's activators, underlie the membrane curvature association of the WAVE complex.

The WAVE complex plays a more central role than the ARP2/3 complex and IRSp53 in forming lamellipodia

As an actin nucleation promoting factor, the WAVE complex's well-characterized link to the actin cytoskeleton is its activation of the ARP2/3 complex (Machesky and Insall, 1998; Pollard and Borisy, 2003; Weaver et al., 2003). Thus, it was surprising that the WAVE complex was not dependent on the ARP2/3 complex to build sheet-like protrusions. In the absence of ARP2, neutrophils still formed sheet-like protrusions with the WAVE complex and IRSp53 at their edges, whereas the formation of these protrusions required the WAVE complex; WAVE complex-null cells formed spiky protrusions (Fig. 7A, B, E). We also observed sheet-like protrusions in primary mouse bone marrow macrophages lacking the Arpc2 subunit (Fig. 7C-D). Furthermore, WAVE2 without its Arp2/3 complex-interacting VCA domain also localized to the leading edge of sheet-like protrusions in HEK-293T cells (Fig. S5). These data suggest that the WAVE complex plays a central role in lamellipodial formation beyond its activation of the ARP2/3 complex, possibly reflecting WAVE's polymerase activity. In addition to activating the nucleation of actin filaments through the ARP2/3 complex, WAVE can also accelerate the elongation of actin filaments by shuttling actin monomers onto the ends of uncapped actin filaments (Bieling et al., 2018). Actin polymerization is still required for these Arp2/3 complex-independent protrusions; F-actin is observed behind the WAVE crescents in these conditions (Fig. 7F), and these extending protrusions are not observed in latrunculin-treated cells.

From our IRSp53 experiments, we found that IRSp53 requires its partnering interactions with the WAVE complex to enrich to lamellipodia and sites of saddle curvature, but IRSp53 is dispensable for the WAVE complex's proper localization and patterning of lamellipodia (Fig. 6). Given that BAR domain proteins may have redundant functions (Chou et al., 2017; Tsujita et al., 2013; Insinna et al., 2019; Nkosi et al., 2013; Park et al., 2010), it is possible that other and/or a combination of I-BAR proteins are essential for proper WAVE complex localization. These data further highlight the central role of the WAVE complex in lamellipodial organization.

Saddle curvature recognition of the WAVE complex may yield emergent behaviors, such as self-straightening lamellipodia and sealing of transcellular holes

The coupling of saddle curvature recognition (cell shape) and patterning F-actin polymerization (physical forces) could result in a number of emergent behaviors (Keren et al., 2008; Moreau et al., 2018). For example, if the WAVE complex both recognizes and generates sites of plasma membrane saddle curvature, this could form a feedback loop that organizes the expansion and self-straightening of lamellipodia. Near the initiation of a lamellipodium, a small sheet-like membrane deformation has saddle curvature at its lateral edges. WAVE complex association with these saddles, perhaps in a half-ring-like form, would result in a laterally expanding zone of actin nucleation, where the wave would grow at the sides but be confined to a small region at the tip of the lamellipodium based on the negative curvature sensing. This spatial constraint on the positive feedback arm of the excitable actin nucleation circuit could explain why the domain of activation for this circuit is much thinner than other excitable circuits, such as

32

cortical excitability in Xenopus (Bement et al., 2016) and Min protein oscillations for

bacterial cell division (Loose et al., 2008).

Saddle enrichment would also enable maintenance of a uniform leading edge

advancement — any regions of the lamellipodia that lag behind also display saddle

curvature, and the WAVE complex enrichment here would result in straightening of the

front. Supporting this hypothesis, the WAVE complex preferentially enriches to flattening

portions of closing transendothelial macroapertures (Fig. S3C). Furthermore,

recruitment of the WAVE complex could enable the recognition and actin-based sealing

of saddle-shaped transendothelial macroaperture tunnels (Maddugoda et al., 2011)

(Fig. 5). Simple local rules of protein association could generate a number of the

emergent features of cell shape and movement.

MATERIALS AND METHODS

Cell culture

All cells were cultured in a 37°C/5% CO2 incubator.

HL60s - HL60 cells were cultured in RPMI-1640 with 25 mM HEPES (Corning) with 10% (vol/vol) heat-inactivated fetal bovine serum (FBS; Gibco) and maintained at 0.2-1.0 x 106 cells/mL. Cells were differentiated with 1.5% DMSO (Sigma-Aldrich) in growth media for 4-5 days prior to experiments. All imaging was performed with differentiated HL60s (dHL60s) unless otherwise stated.

HEK-293Ts - HEK-293T cells were cultured in DMEM (Gibco) with 10% FBS. Cells were cultured up to 80% confluency.

HUVECs – HUVEC cells were a kind gift from the MS Conte lab (University of California, San Francisco [UCSF]). HUVECs were cultured in HyClone M-199 media (GE Healthcare) with 1% antibiotics-antimicrobial (Gibco), 15.3 units of heparin (Sigma), 1 vial of endothelial cell growth supplement (EMD Millipore), and 10% FBS. Cells were cultured up to 80% confluency and growth media was replaced every other day. Experiments used cells with fewer than 10 passages.

B16F10 - B16F10 cells were cultured in DMEM (Gibco) with 10% FBS, 1% penicillin-streptomycin (Gibco), and 1% GlutaMax (Life Technologies). Cells were cultured up to 80% confluency.

U2OS - U2OS cells were a kind gift from the M von Zastrow lab (UCSF). U2OS cells were cultured in McCoy's 5A media (Gibco) with 10% FBS. Cells were cultured up to 80% confluency.

Bone marrow-derived macrophages

Macrophage cells were a kind gift from the JD Rotty lab (Uniformed Services University of the Health Sciences). Cells were cultured according to (Rotty et al., 2017). Briefly, macrophages were cultured in 30% L media and 70% DMEM with 10% FBS and 1% Glutamax. L-conditioned media was generated by growing L929 cells until 80% confluency in DMEM with 10% FBS then centrifuging and sterile filtering the supernatant and kept in ~45 mL aliquots at -80°C. To assess purity and maturity, macrophages were stained with two antibody cocktails (cocktail 1 for purity: CD11B, Ly6C, and CD47; cocktail 2 for maturation: CD11B, Ly6C, and F4/80; all at 1:100 in FACS buffer [1x PBS with 1% FBS]). For antibody staining, ~200,000 cells were pelleted and resuspended in antibody cocktail for 10 min at room temperature and then 30 min at 4°C, then washed and resuspended in FACS buffer and analyzed via flow cytometry during the first passage and one week after culturing. To passage the macrophages, cells were washed with 1x PBS, incubated with 3 mL cold 0.5 mM EDTA at 4 °C for 10 min, detached with a cell scraper, and then replated 1:2 – 1:4. To induce recombination and deletion of the Arpc2 allele, cells at 50-70% confluency were treated with a first dose of 2 µM 4-hydroxy-tamoxifen (4-OHT) for 2 days then a second dose for 3 days. Cells were then plated for imaging and imaged the next day.

Plasmids

For stable expression, all constructs were cloned into the pHR lentiviral backbone (provided by the RD Vale lab, UCSF) with a SFFV promoter via standard Gibson assembly or Mammalian Toolkit (Fonseca et al., 2019). The other WAVE complex subunit constructs (eGFP-Abi1, eGFP-Abi2, eGFP-Sra1, eGFP-Nap1, and eGFP-WAVE2) were a kind gift from the G Scita lab (European Institute of Oncology). IRSp53 was from the DNASU Plasmid Repository (pENTR223) and subsequently subcloned into a pHR vector. IRSp531-250 was "I-BAR," the N-terminal 250 amino acids, and IRSp53251-512 was "C-term," the C-terminal 262 amino acids beyond the I-BAR domain. For all IRSp53 constructs, the eGFP was C-terminally tagged.

Cell line generation

Lentivirus

All HL60s, macrophages, and some HUVEC lines were stably expressing the constructs of interest. HEK-293Ts were plated in 6-well plates (Corning) until 70-80% confluency. Cells were transfected with 1.5 μg of the pHR plasmid along with two plasmids containing the lentiviral packaging proteins (0.167 μg of pMD2.G and 1.3 μg of p8.91) with TransIT-293 (Mirus Bio). After 2-3 days of transfection, lentivirus-containing supernatant was collected, filtered with a 0.45 μm filter (EMD Millipore), and concentrated 20x with Lenti-X Concentrator (Takara). Lentivirus was used immediately or stored at -80°C. For HL60 transduction, 3.2 x 105 cells, 4 μg/mL polybrene, and ~130 μL of concentrated virus were incubated overnight. Cells were sorted via FACS (BD Aria2). For eGFP-tagged IRSp53 structure/function constructs, cells were sorted for

comparable fluorescence expression levels (Fig. S4C). For HUVEC transduction, a 50% confluent 6-well was incubated with 4 µg/mL polybrene and ~130 µL of 1x virus overnight. For macrophage transduction, cells at 60-70% confluency were incubated with 4 µg/mL polybrene and 2x virus overnight.

Electroporation

For transient expression of plasmids in HUVEC cells, electroporation was used. For each electroporation condition, 5 x 104 cells were resuspended in 10 µL of Buffer R (Thermo Scientific) with 500 ng of DNA. Electroporations were performed with the Neon Transfection System (ThermoFisher) with 10 µL tips at 1350 V for 30 ms for 1 pulse. Cells recovered in 500 µL of culture media and imaged the next day.

Lipofectamine

For B16F10 and U2OS cell lines, plasmids were transiently expressed with Lipofectamine 2000 or 3000 (Invitrogen) per manufacturer's instructions.

Generation of CRISPR/Cas9 knock in cell lines

Endogenous locus tagging with split-GFP or split-mNeonGreen is described in (Leonetti et al., 2016). For each HL60 electroporation reaction, Cas9 RNP was generated by incubating 270 pmol of purified sgRNA and 90 pmol of purified Cas9 at room temperature for 30 min and electroporated into cells with 100 pmol single stranded homology directed repair (HDR) donor oligo. For each HEK-293T electroporation reaction, 50 pmol of RNP (with 65 pmol sgRNA) was electroporated with 120 pmol

donor. For each HL60 reaction, 2 x 106 cells expressing GFP1-10 or mNeonGreen1-10 (induced via lentivirus transduction) were resuspended in 100 μL of Buffer R with the RNP-donor mix and pulsed at 1350 V for 35 ms for 1 pulse in Buffer E2 with the Neon Transfection System (ThermoFisher). For each HEK-293T reaction, 1.65 x 105 cells expressing GFP1-10 treated with 200 ng/mL nocodazole for 15-18 hrs were resuspended in 10 μL of Buffer R with the RNP-donor mix and pulsed at 1150 V for 20 ms for 2 pulses in Buffer E with the Neon. Cells recovered in 20% FBS media. For full-length WASF2 (WAVE2), the N terminus of exon 2 was targeted with sgRNA 5' CCTCGTTACTAACGGCATGG 3' and repaired with donor 5' GCTTCTAACGCTAGGCA ACGTCTGACGGCACAGGTGCCTTGGCTCGATGTTCCTCGTTACTAACGGGCCGCC CGAACCGCCGCCACCTGTAATCCCAGCAGCATTTACATACTCATGAAGGACCATGT GGTCACGCATGGTGGACCTGCTTCAGGCAATGTTCTGAATGGTGAAAAACAACCTA AAAAAGAAATAACAGG 3'. To generate WAVE2ΔVCA cells, exon 8 was targeted with sgRNA 5' GTCGCTACGGGCATCGCTCA 3' and repaired with donor 5' AAACCCACCA TTGAAATTTACCTTGACGGATGGCTGAAAGCAGGTCGCTACGGGCATCGCTTACTA GCCGCCACCTGTAATCCCAGCAGCATTTACATACTCATGAAGGACCATGTGGTCAC GGCCGCCCGAACCGCCGCCCGAACCCACGGCAGGCAAGGAGGACTTGGGCTTG GTGGTATCAGAAAGCGGTGG 3'. For CLTA, the reverse strand was targeted with sgRNA 5' GAACGGATCCAGCTCAGCCA 3' and repaired with donor 5' CCAGCGCGG GACCGCCAGGGGCGCCGGCAGGGGCGCCGAACGGATCCAGCTCAGCACCACTT CCTGGACCTTGAAACAAAACTTCCAATCCGCCACCCATCATATCGGTAAAGGCCTT TTGCCACTCCTTGAAGTTGAGCTCGGTCATGGCGGGCAACTGAACGGCACGGACA CCAACGGTGAGACAAAAACCAACCGAC 3'.

After cells recovered, clonal cell lines were generated by FACS sorting GFP or mNeonGreen positive cells into 96 well plates. Clones were screened via fluorescence microscopy and TOPO TA sequencing (Invitrogen). For HEK-293T clonal lines, a ~400 base pair sequence spanning the guide targeting the VCA region was PCR amplified with primers containing GENEWIZ adaptor sequences, gel extracted, and MiSeq was performed using the GENEWIZ Amplicon-EZ service. Resulting paired end reads were analyzed for editing using CRISPResso2 (Clement et al., 2019).

Generation of CRISPR/Cas9 knock out cell lines

Wildtype HL60 cells were first transduced with a plasmid expressing a human codon optimized Streptococcus pyrogenes Cas9 with a C-terminal tagBFP fusion where high tagBFP-expressing cells were sorted via FACS. Cas9-expressing cells were then transduced with a plasmid containing a puromycin-selectable gRNA targeting exon 2 of IRSp53/BAIAP2 (5' TCCGGAACTTCATCGCCATG 3'). After 1 week of puromycin selection, clonal cell lines were generated by diluting cells into 96-well plates at a 0.5 cell/well density. Clonal lines were verified by genomic DNA sequencing of the region flanking the Cas9 cut site, TOPO TA cloning (Invitrogen), and immunoblotting. WAVE complex-null and ARP2-null HL60 cells were from (Graziano et al., 2019).

Immunoblotting

For primary antibodies IRSp53 (Abcam #ab37542), β-actin (Cell Signaling Technology #3700), WAVE2 (1:1,000; Cell Signaling Technology #3659) and GAPDH (1:2,000;

Invitrogen #MA5-15738), protein samples from 1 x 106 cells were prepped in 2x

Laemmli sample buffer, subjected to a SDS-PAGE gel with MES running buffer, and

transferred to a nitrocellulose membrane. Membranes were blocked at room

temperature for 30-60 min in 1:1 solution of TBS (20 mM Tris, 500 mM NaCl, pH 7.4)

and Odyssey Blocking Buffer (LI-COR) and then incubated overnight at 4°C with

primary antibodies diluted in 1:1,000 in a solution of 1:1 TBS-T (TBS with 0.2% w/v

Tween-20) and Odyssey Blocking Buffer. Membranes were washed 3 times with TBS-T

and then incubated for 1 hr at room temperature with secondary antibodies diluted

1:20,000 in Odyssey Blocking Buffer. Secondary antibodies used were IRDye 680RD

Goat anti-Mouse (LI-COR) and IRDye 800CW Goat anti-Rabbit (LI-COR). Membranes

were washed 3 times with TBS-T and 1 time with TBS.

For primary antibodies HEM1 (0.4 µg/mL; Novus Biologicals #13643) and GAPDH

(1:2,000; Invitrogen #MA5-15738), 10 x 106 cells/mL samples were lysed in ice-cold 2x

lysis buffer (1x lysis buffer: 25 mM Tris-HCl, 150 mM NaCl, 5 mM MgCl2, 1% NP-40, 1

mM DTT, 5% glycerol, 1 mM PMSF, and cOmplete protease inhibitor cocktail [Roche])

and spun at 21,000 x g for 20 min at 4°C. Supernatant was removed and prepped in 2x

Laemmli sample buffer then subjected to a SDS-PAGE gel with MOPS running buffer

and transferred to a PVDF membrane. Membranes were blocked for 30-60 min in a 1:1

TBS:Odyssey Blocking Buffer solution and then incubated overnight at 4°C with primary

antibodies diluted in a solution of 1:1 TBS-T:Odyssey Blocking Buffer. Membranes were

washed 3 times with TBS-T and then incubated for 1 hr at room temperature with

secondary antibodies diluted 1:10,000 in Odyssey Blocking Buffer. Secondary HRP

conjugated antibodies used were Goat anti-Mouse IgG (Invitrogen #62-6520) and Goat anti-Rabbit IgG (Invitrogen #65-6120). Membranes were washed 3 times with TBS-T and 1 time with TBS. The membranes were treated with a SuperSignal West Femto kit (Thermo Scientific), following manufacturer's instructions, immediately before imaging. For primary antibodies ARPC2 (1:500; EMD Millipore 07-227) and GAPDH (1:1,000; Invitrogen #MA5-15738). Samples lysates were prepped with ice-cold RIPA buffer with protease (cOmplete protease inhibitor cocktail [Roche]) and phosphatase (Phosphatase Inhibitor Mini Tablets [Pierce]) inhibitors, rotated for 15 min at 4°C and spun at 21,000 x g for 10 min at 4°C. ECL Western blots were performed as described above except for a 1:1 solution of PBS-Tween (0.2%) and 5% milk solution for block and antibodies incubation steps.

All blots were imaged with an Odyssey Fc (LI-COR) and analyzed with ImageStudioLite.

Immunostaining

Cells were fixed as described and blocked with 3% BSA and 0.1% Triton X-100 diluted in PBS for 1 hr at room temperature. Primary antibody was diluted in blocking solution at 4°C overnight, washed 3x with PBS, and then incubated with the secondary antibody and washed 3x with PBS. SEPT7 (IBL #18991) primary antibody used at 1:1,000 dilution with secondary antibody Goat anti-Rabbit IgG conjugated to Alexa Fluor 680 (Invitrogen #A-21076) at 1:1,000 dilution.

Imaging

<u>Cell preparation</u>

HL60s

For imaging, differentiated cells were resuspended in imaging media (either Leibovitz's

L-15 [Gibco] with 0.5% FBS or modified Hank's Balanced Salt Solution [mHBSS; 10x

stock consists of 1500 mM NaCl, 40 mM KCl, 10 mM MgCl2, 12 mM CaCl2, 100 mM

glucose, 200 mM HEPES, pH 7.2]). Cells were plated onto fibronectin coated wells (100

µg/mL for 1 hr at room temperature) and incubated (37°C/5% CO2) for at least 7

minutes before 2-3 washes with imaging media. For chemoattractant stimulation, a 2x

stock of 20 nM N-formyl-L-methionyl-L-leucyl-L-phenylalanine (fMLP; Sigma) was

added. For additional chemoattractant stimulation, a 2x stock of 200 nM fMLP was

added. For F-actin inhibition, a 2x stock of 1 µM latrunculin B (EMD

Millipore and Sigma) with 200 nM phorbol 12-myristate 13-acetate (PMA; Sigma; for

persistent Hem1 activation) was used, unless noted otherwise. Other F-actin inhibition

drugs were latrunculin A (EMD Millipore) and cytochalasin B (Sigma). All initial stocks

were dissolved in 100% dry DMSO and freshly diluted in imaging media before

experiments. Clostridium difficile toxin B (Sigma) was added to the cells at a final

concentration of 1 µg/mL for at least 4 hrs.

HUVECs

To induce transendothelial cell macroaperture formation, HUVECs were incubated in 50

µM Y27632 (Tocris and Sigma) for at least 4 hours before imaging. Y27632 was present

throughout imaging.

Membrane labeling

For membrane labeling, Vybrant DiD (Invitrogen) or CellMask Deep Red (Invitrogen) was freshly diluted (50-500 nM) in imaging media. HL60s were labeled in suspension for 30 sec at 37°C and washed 2-3 times with imaging media. Adherent cell lines were labeled for 5 min at 37°C and washed 3-5 times with PBS.

Fixation

Cells were plated in #1.5, 8-well Lab-Tek II chambers (Thermo Fisher Scientific). To fix cells, media was aspirated while simultaneously adding 200 µL of 2% glutaraldehyde (Sigma-Aldrich) for 10 min and washed with phosphate buffered saline (PBS) for 30 sec and 60 sec. Aldehydes were quenched with 0.1% sodium borohydride (Sigma-Aldrich) for 7 min and followed by two-to-three 10 min PBS washes. Samples were imaged immediately or stored at 4°C. All dilutions were prepared fresh in cytoskeleton buffer with sucrose (CBS), a TJ Mitchison lab (Harvard Medical School) recipe: 10 mM MES pH 6.1, 138 mM KCl, 3 mM MgCl, 2 mM EGTA, with 0.32 M sucrose added fresh before use. HUVECs were fixed with 4% PFA in PBS, pH 7.4. All materials were warmed to 37°C.

Phalloidin staining

Cells were fixed as described above and stained with Alexa Fluor 647 phalloidin (5 µL/mL; Invitrogen) in 1x CBS buffer for 15-45 min and washed with CBS buffer. Samples were imaged immediately or stored at 4°C.

<u>Microscopes</u>

TIRF-SIM

TIRF-SIM imaging was performed on DeltaVision OMX SR (GE Healthcare) with a 60x/1.42 numerical aperture (NA) oil Plan Apo objective (Olympus) with 1.516 or 1.518 refractive index oil (Cargille). HL60 experiments were performed at room temperature while adherent cells were performed at 37°C/5% CO2. Images were processed with softWoRx (OMX SI Reconstruction with the default parameters including Wiener filter: 0.001. OMX Align Images with the Legacy Image Registration method). Display of some TIRF-SIM membrane images were smoothed in Fiji.

Spinning disk confocal

Images were acquired on a Nikon Eclipse Ti microscope with a 60x/1.40 NA Plan Apo objective (Nikon), Yokogawa C SU-X1 spinning disk confocal, and a Prime 95B cMOS camera (Photometrics). 405, 488, 561, 640 nm laser lines (Agilent Technologies) and environmental control (37°C/5% CO2; Okolab) was used. Software was controlled with Nikon Elements.

Lattice light sheet and processing

Lattice-light sheet imaging was performed in a manner previously described (Chen et al., 2014) and followed an established protocol (Cai et al., 2017). Briefly, 5 mm round coverslips (Warner Instruments) were plasma cleaned and fibronectin-coated (100 μg/mL for 1 hr). Cells were plated as described above. The coverslip sample was then

loaded into a sample holder and placed into the previously conditioned microscope sample bath with 25 nM chemoattractant and secured. Imaging was performed with a 488 nm laser (MPBC). Camera exposure was 10 ms per frame leading to a temporal resolution of 2.25 sec in single color mode.

Raw image files were deconvolved using the iterative Richardson-Lucy algorithm with the known point spread function for each channel, which were collected prior to each day of imaging (Chen et al., 2014). The code for this process was provided by the E Betzig lab (Janelia Research Campus) originally written in Matlab (The Mathworks) and ported into CUDA (Nvidia) for parallel processing on the graphics processing unit (GPU, Nvidia GeForce GTX Titan X). Each sample area underwent 15 iterations of deconvolution.

Regions of interest within the sampling were cropped down to size and compressed from 32-bit TIFFs to 16-bit TIFFs using in-house Matlab code to allow immigration into the 3D visualization software ChimeraX (UCSF Resource for Biocomputing, Visualization, and Informatics (Goddard et al., 2018)). To highlight intensity ranges, additional channels were created by thresholding.

Transmission electron microscopy
Cells were prepared for conventional EM in two ways: cells were either plated on fibronectin-coated ACLAR discs (TedPella), fixed with glutaraldehyde as described above, and dehydrated and embedded in resin or cells were plated on sapphire disks

and fixed via high pressure freezing/freeze-substitution. For the glutaraldehyde fixation method, cells were treated with 100 nM chemoattractant or 500 nM latrunculin B for 5 min, fixed, stained with uranyl acetate and OsO4, dehydrated with cold ethanol, and embedded with Epon 812 resin. For the high pressure freezing/freeze-substitution method, cells were plated onto 3 mm diameter sapphire disks and treated with 100 nM chemoattractant or 500 nM latrunculin B for 5 min prior to freezing. The sapphire disk was then placed, cells toward the inside of a 100 μm well specimen carriers (Type A, Technotrade International Inc) containing 20% BSA in growth media. The sandwiched cells were frozen using a BalTec HPM 01 high pressure freezer (BalTec). Freeze-substitution in 1% OsO4, 0.1% uranyl acetate, 1% methanol in acetone, containing 3% water (Buser and Walther, 2008; Walther and Ziegler, 2002) was carried out with a Leica AFS2 unit. Following substitution, samples were rinsed in acetone, infiltrated and then polymerized in Eponate 12 resin (Ted Pella). For conventional electron microscopy, serial 50 nm sections were cut with a Leica UCT ultramicrotome using a Diatome diamond knife, picked up on Pioloform coated slot grids and stained with uranyl acetate and Sato's lead (T, 1968). Sections were imaged with a FEI Tecnai T12 TEM at 120 kV using a Gatan 2k x 2k camera. For EM tomography, 200 nm sections were cut, mounted on grids and stained as above for serial thin sections. Tomograms were acquired using an FEI T20 TEM at 200 kV, and tomograms reconstructed using eTomo/IMOD (Kremer et al., 1996; Mastronarde, 1997).

Image analysis and statistics

All image analysis was performed in Fiji and/or Python. Data handling and statistical

tests were performed with Python and Prism 7-8 (GraphPad).

Diameter calculation

After background subtraction (rolling ball), segmentation was performed with Trainable

Weka Segmentation (Arganda-Carreras et al., 2017) machine learning algorithm to

identify ring structures. The diameter of a perfect circle with the same perimeter of the

ring particle was calculated (diameter = C/π; C, circumference).

Membrane curvature and velocity

Fluorescence images were segmented using a 3-step process consisting of Gaussian

smoothing, intensity-based thresholding, and binary erosion. The threshold and degree

of erosion were chosen manually to align the boundary of the binary image with the

apparent edge of the cell membrane. To facilitate temporal analysis of edge properties,

these boundaries were then fit using a spline interpolation consisting of 1,000 points.

Edge velocity at a particular point, P, at time, t, was estimated by calculating the

average of the distance transforms of the binary images at times t-1 and t+1 and

interpolating the value of this function at the coordinates of P. The radius of curvature at

a point, P, was calculated by approximating the radius of the osculating circle, C, along

the boundary at the coordinates of P. To approximate this osculating circle, we chose a

scale parameter, S, then collected the coordinates of the two points at indices S units

away from P. To adjust for the image pixel size, S = 10 for transendothelial cell

macroaperture (TEM) images and S = 44 for the HL60 migrating cell. Given these three points, we calculated the unique equation of a circle passing through them. A sign could then be assigned by comparing the vector between P and the center of circle C and the normal vector of the boundary.

To calculate WAVE complex signal intensity, we expanded the boundary in both directions to create a ring-shaped region and calculated the average background-corrected signal as a function of angle relative to the center of the region. For the TEM data, we calculated the binned average fluorescence signals from 0 to 360 degrees in 7.2 degree increments (for 50 bins total). For the HL60 migrating cell dataset, 1000 bins were used. Normalized WAVE complex intensity is the ratio of background-corrected WAVE signal to the background-corrected membrane signal (which was calculated similarly). To standardize the edge measurements across time and across TEMs, and to make comparisons between geometric and fluorescence features, we employed a similar binning strategy for the geometric features.

Based on simulations that incorporated expected WAVE complex behaviors (for example, residence time on the membrane), we expected that an instantaneous statistical relationship between WAVE signal and curvature would be difficult to detect in a system with an intact cytoskeleton. Thus, we looked for enrichment of WAVE signal in areas of positive curvature that were becoming less positive (flattening) or becoming more positive (lagging). By calculating the change in angle-binned average curvature over time, we isolated regions with positive curvature that had a positive derivative and

regions with positive curvature that had negative derivative. We then extracted and compared the fluorescence values from these regions. By artificially "rotating" the normalized WAVE fluorescence values by 1 increment (7.2 degrees) and recalculating the enrichment scores, we can estimate the significance of the enrichment of WAVE signal in flattening areas over lagging areas.

EM curvature

After identifying the plasma membrane, a perfect circle was fitted to both sides of the neck of an invagination and at the tip of a protrusion. Curvature, κ, was defined as κ = 1/r (r, radius).

Transendothelial cell macroaperture (TEM) enrichment

Transendothelial cell macroapertures were identified by segmenting the membrane channel (TEM mask). The signal mask was generated by dilating the TEM mask by 2-3 pixels and the background mask was generated by dilating the signal mask by 2-3 pixels. A doughnut-shaped signal segment was calculated by subtracting the TEM mask from the signal mask and a doughnut-shaped background segment was calculated by subtracting the signal mask from the background mask. The doughnut-shaped signal segment was background corrected (subtracting the background intensity per unit area multiplied by the signal mask area). The enrichment factor was measured as the ratio of the signal to background intensities per unit areas. The intensity per unit perimeter was calculated as the background-corrected signal intensity divided by the signal perimeter.

IRSp53 and Hem1 colocalization

Images were background subtracted (rolling ball) and Fiji's coloc2 function was applied with the segmented images and an ROI of the combined masks.

IRSp53 lamellipodia/filopodia enrichment

After background subtraction (rolling ball), two masks were generated: a lamellipodia mask was created from Hem1 signal and a filopodia mask was created from the eroded regions of a cell mask. After subtracting the cytosolic background from each segment (cytosolic intensity per unit area multiplied by the segment's area), the intensity per unit area of each segment was calculated, i.e. lamellipodia signal/lamellipodia area. The ratio of the lamellipodia to the filopodia intensities per unit areas was graphed.

IRSp53 structure/function ring enrichment

After background subtraction (rolling ball), a ring mask was generated from segmenting Hem1 signal and a background mask was generated by dilating the ring mask. IRSp53 signal was measured from both masks. After background correction (subtracting the background intensity per unit area multiplied by the ring mask area), the enrichment factor was calculated as the ratio of the ring to the background intensities per unit areas. Enrichment of all rings within a cell was averaged and treated as an individual data point.

Phalloidin intensity

After background subtraction (rolling ball), a Hem1 mask was generated from segmenting Hem1 intensity signal. The phalloidin signal within the Hem1 mask was compared to the signal within the same mask of a randomized version of the phalloidin image.

Protrusion analysis

Fluorescence images were segmented with Gaussian smoothing, intensity-based thresholding, and binary erosion. To identify protrusions, difference maps (of 1 minute intervals) were generated by subtracting the segmented masks. For protrusion widths, the width at the midpoint of the extension's length was measured. For protrusion speed, the extension's length over 1 minute was measured.

SUPPLEMENTAL MATERIAL

Fig. S1 shows Western blots of HEM1 and WAVE2 expression levels from the Hem1-eGFP HL60 cell line used throughout the study, data from endogenously split-GFP labeled WAVE2, and phalloidin staining. Fig. S2 shows the WAVE complex rings across different actin polymerization inhibitors and concentrations, multiple super-resolution microscopy techniques, tagged fluorescent protein, labeled WAVE complex subunits, and cell lines. Fig. S3 shows plots comparing WAVE complex signal and membrane velocity as well as its enrichment in flattening versus lagging membrane regions. Fig. S4 shows additional IRSp53 data: TIRF-SIM images of high-expression of IRSp53, IRSp53 ring measurements, flow plots of IRSp53 structure/function constructs, IRSp53 structure/function confocal imaging in HUVECs, and characterization of the CRISPR/Cas9 knock out of IRSp53 (Western blots and TOPO sequence). Fig. S5 shows the generation of WAVE2ΔVCA split-GFP endogenous knock-in HEK-293T cell line and its localization to the leading edge of sheet-like protrusions.

ACKNOWLDGEMENTS

REFERENCES

Abercrombie, M., J.E.M. Heaysman, and S.M. Pegrum. 1970. The locomotion of fibroblasts in culture. III. Movements of particles on the dorsal surface of the leading lamella. *Exp. Cell Res.* 62:389–398. doi:10.1016/0014-4827(70)90570-7.

Abou-Kheir, W., B. Isaac, H. Yamaguchi, and D. Cox. 2008. Membrane targeting of WAVE2 is not sufficient for WAVE2-dependent actin polymerization: A role for IRSp53 in mediating the interaction between Rac and WAVE2. *J. Cell Sci.* 121:379–390. doi:10.1242/jcs.010272.

Abraham, V.C., V. Krishnamurthi, D. Lansing Taylor, and F. Lanni. 1999. The actin-based nanomachine at the leading edge of migrating cells. *Biophys. J.* 77:1721–1732. doi:10.1016/S0006-3495(99)77018-9.

Allard, J., and A. Mogilner. 2013. Traveling waves in actin dynamics and cell motility. *Curr. Opin. Cell Biol.* 25:107–115. doi:10.1016/j.ceb.2012.08.012.

Arganda-Carreras, I., V. Kaynig, C. Rueden, K.W. Eliceiri, J. Schindelin, A. Cardona, and H.S. Seung. 2017. Trainable Weka Segmentation: A machine learning tool for microscopy pixel classification. *Bioinformatics*. 33:2424–2426. doi:10.1093/bioinformatics/btx180.

Banjade, S., and M.K. Rosen. 2014. Phase transitions of multivalent proteins can promote clustering of membrane receptors. *Elife*. 3:1–24. doi:10.7554/eLife.04123.

Bement, W.M., M. Leda, A.M. Moe, A.M. Kita, M.E. Larson, A.E. Golding, C. Pfeuti, K. Su, A.L. Miller, and B. Andrew. 2016. Activator-inhibitor coupling between Rho signaling and actin assembly make the cell cortex an excitable medium. *Nat. Cell Biol.* 17:1471–1483. doi:10.1038/ncb3251.Activator-inhibitor.

Benesch, S., S. Polo, F.P. Lai, K.I. Anderson, T.E.B. Stradal, J. Wehland, and K. Rottner. 2005. N-WASP deficiency impairs EGF internalization and actin assembly at clathrin-coated pits. *J. Cell Sci.* 118:3103–3115. doi:10.1242/jcs.02444.

Bieling, P., S.D. Hansen, O. Akin, T. Li, C.C. Hayden, D.A. Fletcher, and R.D. Mullins. 2018. WH2 and proline-rich domains of WASP-family proteins collaborate to accelerate actin filament elongation. *EMBO J.* 37:102–121. doi:10.15252/embj.201797039.

Boujemaa-Paterski, R., C. Suarez, T. Klar, J. Zhu, C. Guérin, A. Mogilner, M. Théry, and L. Blanchoin. 2017. Network heterogeneity regulates steering in actin-based motility. *Nat. Commun.* 8:1–12. doi:10.1038/s41467-017-00455-1.

Boyer, L., A. Doye, M. Rolando, G. Flatau, P. Munro, P. Gounon, R. Clément, C. Pulcini, M.R. Popoff, A. Mettouchi, L. Landraud, O. Dussurget, and E. Lemichez. 2006. Induction of transient macroapertures in endothelial cells through RhoA inhibition by Staphylococcus aureus factors. *J. Cell Biol.* 173:809–819. doi:10.1083/jcb.200509009.

Bridges, A.A., M.S. Jentzsch, P.W. Oakes, P. Occhipinti, and A.S. Gladfelter. 2016. Micron-scale plasma membrane curvature is recognized by the septin cytoskeleton. *J. Cell Biol.* 213:23–32. doi:10.1083/jcb.201512029.

Bu, W., A.M. Chou, K.B. Lim, T. Sudhaharan, and S. Ahmed. 2009. The Toca-1-N-WASP complex links filopodial formation to endocytosis. *J. Biol. Chem.* 284:11622–11636. doi:10.1074/jbc.M805940200.

Buser, C., and P. Walther. 2008. Freeze-substitution: The addition of water to polar solvents enhances the retention of structure and acts at temperatures around -60°C. *J. Microsc.* 230:268–277. doi:10.1111/j.1365-2818.2008.01984.x.

Cai, E., K. Marchuk, P. Beemiller, C. Beppler, M.G. Rubashkin, V.M. Weaver, A. Gérard, T.L. Liu, B.C. Chen, E. Betzig, F. Bartumeus, and M.F. Krummel. 2017. Visualizing dynamic microvillar search and stabilization during ligand detection by T cells. *Science (80-.).* 356. doi:10.1126/science.aal3118.

Carlier, M.F., C. Le Clainche, S. Wiesner, and D. Pantaloni. 2003. Actin-based motility: From molecules to movement. *BioEssays*. 25:336–345. doi:10.1002/bies.10257.

Carman, C. V., and T.A. Springer. 2008. Trans-cellular migration: cell-cell contacts get intimate. *Curr. Opin. Cell Biol.* 20:533–540. doi:10.1016/j.ceb.2008.05.007.

Case, L.B., X. Zhang, J.A. Ditlev, and M.K. Rosen. 2019. Stoichiometry controls activity of phase-separated clusters of actin signaling proteins. *Science (80-.).* 363:1093–1097. doi:10.1126/science.aau6313.

Chen, B., H.T. Chou, C.A. Brautigam, W. Xing, S. Yang, L. Henry, L.K. Doolittle, T. Walz, and M.K. Rosen. 2017. Rac1 GTPase activates the WAVE regulatory complex through two distinct binding sites. *Elife*. 6:1–22. doi:10.7554/eLife.29795.

Chen, B.C., W.R. Legant, K. Wang, L. Shao, D.E. Milkie, M.W. Davidson, C. Janetopoulos, X.S. Wu, J.A. Hammer, Z. Liu, B.P. English, Y. Mimori-Kiyosue, D.P. Romero, A.T. Ritter, J. Lippincott-Schwartz, L. Fritz-Laylin, R.D. Mullins, D.M. Mitchell, J.N. Bembenek, A.C. Reymann, R. Böhme, S.W. Grill, J.T. Wang, G. Seydoux, U.S. Tulu, D.P. Kiehart, and E. Betzig. 2014. Lattice light-sheet

microscopy: Imaging molecules to embryos at high spatiotemporal resolution. *Science (80-.).* 346. doi:10.1126/science.1257998.

Chen, Z., D. Borek, S.B. Padrick, T.S. Gomez, Z. Metlagel, A.M. Ismail, J. Umetani, D.D. Billadeau, Z. Otwinowski, and M.K. Rosen. 2010. Structure and control of the actin regulatory WAVE complex. *Nature*. 468:533–538. doi:10.1038/nature09623.

Chesarone, M.A., and B.L. Goode. 2009. Actin nucleation and elongation factors: mechanisms and interplay. *Curr. Opin. Cell Biol.* 21:28–37. doi:10.1016/j.ceb.2008.12.001.

Chou, A.M., K.P. Sem, W.J. Lam, S. Ahmed, and C.Y. Lim. 2017. Redundant functions of I-BAR family members, IRSp53 and IRTKS, are essential for embryonic development. *Sci. Rep.* 7:1–11. doi:10.1038/srep40485.

Clement, K., H. Rees, M.C. Canver, J.M. Gehrke, R. Farouni, J.Y. Hsu, M.A. Cole, D.R. Liu, J.K. Joung, D.E. Bauer, and L. Pinello. 2019. CRISPResso2 provides accurate and rapid genome editing sequence analysis. *Nat. Biotechnol.* 37:224–226. doi:10.1038/s41587-019-0032-3.

Davidson, A.J., C. Amato, P.A. Thomason, and R.H. Insall. 2018. WASP family proteins and formins compete in pseudopod- and bleb-based migration. *J. Cell Biol.* 217:701–714. doi:10.1083/jcb.201705160.

Disanza, A., S. Mantoani, M. Hertzog, S. Gerboth, E. Frittoli, A. Steffen, K. Berhoerster, H. Kreienkamp, F. Milanesi, P. Paolo, D. Fiore, A. Ciliberto, T.E.B. Stradal, and G. Scita. 2006. Regulation of cell shape by Cdc42 is mediated by the synergic actin-bundling activity of the Eps8 – IRSp53 complex. 8. doi:10.1038/ncb1502.

Diz-Muñoz, A., K. Thurley, S. Chintamen, S.J. Altschuler, L.F. Wu, D.A. Fletcher, and

    O.D. Weiner. 2016. Membrane Tension Acts Through PLD2 and mTORC2 to Limit

    Actin Network Assembly During Neutrophil Migration. *PLoS Biol.* 14:1–30.

    doi:10.1371/journal.pbio.1002474.

Eden, S., R. Rohatgi, A. V. Podtelejnikov, M. Mann, and M.W. Kirschner. 2002.

    Mechanism of regulation of WAVE1-induced actin nucleation by Rac1 and Nck.

    Nature. 418:790–793. doi:10.1038/nature00859.

Etienne-Manneville, S., and A. Hall. 2002. Rho GTPases in cell biology. *Nature*.

    420:629–635. doi:https://doi.org/10.1038/nature01148.

Evans, I.R., P.A. Ghai, V. Urbančič, K.L. Tan, and W. Wood. 2013. SCAR/WAVE-

    mediated processing of engulfed apoptotic corpses is essential for effective

    macrophage migration in Drosophila. *Cell Death Differ.* 20:709–720.

    doi:10.1038/cdd.2012.166.

Fonseca, J.P., A.R. Bonny, G.R. Kumar, A.H. Ng, J. Town, Q.C. Wu, E. Aslankoohi,

    S.Y. Chen, G. Dods, P. Harrigan, L.C. Osimiri, A.L. Kistler, and H. El-Samad. 2019.

    A Toolkit for Rapid Modular Construction of Biological Circuits in Mammalian Cells.

    ACS Synth. Biol. 8:2593–2606. doi:10.1021/acssynbio.9b00322.

Fritz-Laylin, L.K., S.J. Lord, and R.D. Mullins. 2017a. WASP and SCAR are

    evolutionarily conserved in actin-filled pseudopod-based motility. *J. Cell Biol.*

    216:1673–1688. doi:10.1083/jcb.201701074.

Fritz-Laylin, L.K., M. Riel-Mehan, B.-C. Chen, S.J. Lord, T.D. Goddard, T.E. Ferrin, S.M.

    Nicholson-Dykstra, H. Higgs, G.T. Johnson, E. Betzig, and R.D. Mullins. 2017b.

Actin-based protrusions of migrating neutrophils are intrinsically lamellar and facilitate direction changes. *Elife*. 6. doi:10.1300/J147v09n04_06.

Frost, A., V.M. Unger, and P. De Camilli. 2009. The BAR Domain Superfamily: Membrane-Molding Macromolecules. *Cell*. 137:191–196. doi:10.1016/j.cell.2009.04.010.

Galkina, S.I., N. V. Fedorova, M. V. Serebryakova, E.A. Arifulin, V.I. Stadnichuk, L.A. Baratova, and G.F. Sud'ina. 2018. Mold alkaloid cytochalasin d modifies the morphology and secretion of FMLP-, LPS-, or PMA-stimulated neutrophils upon adhesion to fibronectin. *Mediators Inflamm.* 2018. doi:10.1155/2018/7202698.

Genuth, M.A., C.D.C. Allen, T. Mikawa, and O.D. Weiner. 2018. Chick cranial neural crest cells use progressive polarity refinement, not contact inhibition of locomotion, to guide their migration. *Dev. Biol.* 444:S252–S261. doi:10.1016/j.ydbio.2018.02.016.

Goddard, T.D., C.C. Huang, E.C. Meng, E.F. Pettersen, G.S. Couch, J.H. Morris, and T.E. Ferrin. 2018. UCSF ChimeraX: Meeting modern challenges in visualization and analysis. *Protein Sci.* 27:14–25. doi:10.1002/pro.3235.

Goh, W.I., K.B. Lim, T. Sudhaharan, K.P. Sem, W. Bu, A.M. Chou, and S. Ahmed. 2012. mDia1 and WAVE2 proteins interact directly with IRSp53 in filopodia and are involved in filopodium formation. *J. Biol. Chem.* 287:4702–4714. doi:10.1074/jbc.M111.305102.

Graziano, B.R., J.P. Town, T.L. Nagy, M. Fošnarič, S. Penič, A. Iglič, V. Kralj-Iglič, N. Gov, A. Diz-Muñoz, and O.D. Weiner. 2019. Cell confinement reveals a branched-actin independent circuit for neutrophil polarity. e3000457 pp.

Hahne, P., A. Sechi, S. Benesch, and J.V. Small. 2001. Scar/WAVE is localised at the tips of protruding lamellipodia in living cells. *FEBS Lett.* 492:215–220. doi:10.1016/S0014-5793(01)02239-6.

Hall, A. 1998. Rho GTpases and the actin cytoskeleton. *Science (80-.).* 279:509–514. doi:10.1126/science.279.5350.509.

Ho, H.-Y., L. Ma, J.X. Li, R. Rohatgi, A. Lebensohn, J. Le Ma, S. Li, and M. Gygi. 2004. Toca-1 mediates Cdc42-dependent actin nucleation by activating the N-WASP-WIP complex. *Cell*. 118:203–216.

Huang, C.H., M. Tang, C. Shi, P.A. Iglesias, and P.N. Devreotes. 2013. An excitable signal integrator couples to an idling cytoskeletal oscillator to drive cell migration. *Nat. Cell Biol.* 15:1307–1316. doi:10.1038/ncb2859.

Ibarra, N., S.L. Blagg, F. Vazquez, and R.H. Insall. 2006. Nap1 Regulates Dictyostelium Cell Motility and Adhesion through SCAR-Dependent and -Independent Pathways. *Curr. Biol.* 16:717–722. doi:10.1016/j.cub.2006.02.068.

Innocenti, M., A. Zucconi, A. Disanza, E. Frittoli, L.B. Areces, A. Steffen, T.E.B. Stradal, P.P. Di Fiore, M.F. Carlier, and G. Scita. 2004. Abi1 is essential for the formation and activation of a WAVE2 signalling complex. *Nat. Cell Biol.* 6:319–327. doi:10.1038/ncb1105.

Insinna, C., Q. Lu, I. Teixeira, A. Harned, E.M. Semler, J. Stauffer, V. Magidson, A. Tiwari, A.K. Kenworthy, K. Narayan, and C.J. Westlake. 2019. Investigation of F-BAR domain PACSIN proteins uncovers membrane tubulation function in cilia assembly and transport. *Nat. Commun.* 10:1–17. doi:10.1038/s41467-018-08192-9.

Just, I., J. Selzer, M. Wilm, C. von Eichel-Streiber, M. Mann, and K. Aktories. 1995. Glucosylation of Rho proteins by Clostridium difficile toxin B. *Nature*. 375:500–503. doi:10.1038/246170a0.

Keren, K., Z. Pincus, G.M. Allen, E.L. Barnhart, G. Marriott, A. Mogilner, and J.A. Theriot. 2008. Mechanism of shape determination in motile cells. *Nature*. 453:475–480. doi:10.1038/nature06952.

Kheir, W.A., J.C. Gevrey, H. Yamaguchi, B. Isaac, and D. Cox. 2005. A WAVE2-Abi1 complex mediates CSF-1-induced F-actin-rich membrane protrusions and migration in macrophages. *J. Cell Sci.* 118:5369–5379. doi:10.1242/jcs.02638.

Kinoshita, M., C.M. Field, M.L. Coughlin, A.F. Straight, and T.J. Mitchison. 2002. Self- and actin-templated assembly of mammalian septins. *Dev. Cell*. 3:791–802. doi:10.1016/S1534-5807(02)00366-0.

Koronakis, V., P.J. Hume, D. Humphreys, T. Liu, O. Hørning, O.N. Jensen, and E.J. McGhie. 2011. WAVE regulatory complex activation by cooperating GTPases Arf and Rac1. *Proc. Natl. Acad. Sci. U. S. A.* 108:14449–14454. doi:10.1073/pnas.1107666108.

Kremer, J.R., D.N. Mastronarde, and J.R. McIntosh. 1996. Computer visualization of three-dimensional image data using IMOD. *J. Struct. Biol.* 116:71–76. doi:10.1006/jsbi.1996.0013.

Krugmann, S., I. Jordens, K. Gevaert, M. Driessens, J. Vandekerckhove, and A. Hall. 2001. Cdc42 induces filopodia by promoting the formation of an IRSp53:Mena complex. *Curr. Biol.* 11:1645–1655. doi:10.1016/S0960-9822(01)00506-1.

Kunda, P., G. Craig, V. Dominguez, and B. Baum. 2003. Abi, Sra1, and Kette Control the Stability and Localization of SCAR/WAVE to Regulate the Formation of Actin-Based Protrusions. *Curr. Biol.* 13:1867–1875. doi:10.1016/j.cub.2003.10.005.

Lebensohn, A.M., and M.W. Kirschner. 2009. Activation of the WAVE Complex by Coincident Signals Controls Actin Assembly. *Mol. Cell*. 36:512–524. doi:10.1016/j.molcel.2009.10.024.

Leithner, A., A. Eichner, J. Müller, A. Reversat, M. Brown, J. Schwarz, J. Merrin, D.J.J. De Gorter, F. Schur, J. Bayerl, I. De Vries, S. Wieser, R. Hauschild, F.P.L. Lai, M. Moser, D. Kerjaschki, K. Rottner, J.V. Small, T.E.B. Stradal, and M. Sixt. 2016. Diversified actin protrusions promote environmental exploration but are dispensable for locomotion of leukocytes. *Nat. Cell Biol.* 18:1253–1259. doi:10.1038/ncb3426.

Lemichez, E., M. Lecuit, X. Nassif, and S. Bourdoulous. 2010. Breaking the wall: Targeting of the endothelium by pathogenic bacteria. *Nat. Rev. Microbiol.* 8:93–104. doi:10.1038/nrmicro2269.

Leng, Y., J. Zhang, K. Badour, E. Arpaia, S. Freeman, P. Cheung, M. Siu, and K. Siminovitch. 2005. Abelson-interactor-1 promotes WAVE2 membrane translocation and Abelson-mediated tyrosine phosphory lation required for WAVE2 activation. *Proc. Natl. Acad. Sci. U. S. A.* 102:1098–1103. doi:10.1073/pnas.0409120102.

Leonetti, M.D., S. Sekine, D. Kamiyama, J.S. Weissman, and B. Huang. 2016. A scalable strategy for high-throughput GFP tagging of endogenous human proteins. *Proc. Natl. Acad. Sci. U. S. A.* 113:E3501–E3508. doi:10.1073/pnas.1606731113.

Lieber, A.D., S. Yehudai-Resheff, E.L. Barnhart, J.A. Theriot, and K. Keren. 2013. Membrane tension in rapidly moving cells is determined by cytoskeletal forces. *Curr. Biol.* 23:1409–1417. doi:10.1016/j.cub.2013.05.063.

Litschko, C., J. Linkner, S. Brühmann, T.E.B. Stradal, T. Reinl, L. Jänsch, K. Rottner, and J. Faix. 2017. Differential functions of WAVE regulatory complex subunits in the regulation of actin-driven processes. *Eur. J. Cell Biol.* 96:715–727. doi:10.1016/j.ejcb.2017.08.003.

Liu, A.P., D.L. Richmond, L. Maibaum, S. Pronk, P.L. Geissler, and D.A. Fletcher. 2008. Membrane-induced bundling of actinfilaments. *Nat. Phys.* 4:789–793. doi:10.1038/nphys1071.

Loose, M., E. Fischer-friedrich, J. Ries, K. Kruse, and P. Schwille. 2008. Spatial Regulators for Bacterial Cell. *Science*. 320:789–792. doi:10.1126/science.1154413.

Machesky, L.M., and R.H. Insall. 1998. Scar1 and the related Wiskott-Aldrich syndrome protein, WASP, regulate the actin cytoskeleton through the Arp2/3 complex. *Curr. Biol.* 8:1347–1356. doi:10.1016/S0960-9822(98)00015-3.

Machesky, L.M., R.D. Mullins, H.N. Higgs, D.A. Kaiser, L. Blanchoin, R.C. May, M.E. Hall, and T.D. Pollard. 1999. Scar, a WASp-related protein, activates nucleation of actin filaments by the Arp2/3 complex. *Proc. Natl. Acad. Sci. U. S. A.* 96:3739–3744. doi:10.1073/pnas.96.7.3739.

Maddugoda, M.P., C. Stefani, D. Gonzalez-Rodriguez, J. Saarikangas, S. Torrino, S. Janel, P. Munro, A. Doye, F. Prodon, M. Aurrand-Lions, P.L. Goossens, F. Lafont, P. Bassereau, P. Lappalainen, F. Brochard, and E. Lemichez. 2011. CAMP signaling by Anthrax edema toxin induces transendothelial cell tunnels, which Are

resealed by MIM via Arp2/3-Driven actin polymerization. *Cell Host Microbe*. 10:464–474. doi:10.1016/j.chom.2011.09.014.

Mastronarde, D.N. 1997. Dual-axis tomography: An approach with alignment methods that preserve resolution. *J. Struct. Biol.* 120:343–352. doi:10.1006/jsbi.1997.3919.

Mattila, P.K., A. Pykäläinen, J. Saarikangas, V.O. Paavilainen, H. Vihinen, E. Jokitalo, and P. Lappalainen. 2007. Missing-in-metastasis and IRSp53 deform PI(4,5)P2-rich membranes by an inverse BAR domain-like mechanism. *J. Cell Biol.* 176:953–964. doi:10.1083/jcb.200609176.

Mendoza, M.C., E.E. Er, W. Zhang, B.A. Ballif, H.L. Elliott, G. Danuser, and J. Blenis. 2011. ERK-MAPK Drives Lamellipodia Protrusion by Activating the WAVE2 Regulatory Complex. *Mol. Cell*. 41:661–671. doi:10.1016/j.molcel.2011.02.031.

Miki, H., T. Sasaki, Y. Takai, and T. Takenawa. 1998. Induction of filopodium formation by a WASP-related actin- depolymerizing protein N-WASP. *Nature*. 391:93–96. doi:10.1038/34208.

Miki, H., H. Yamaguchi, S. Suetsugu, and T. Takenawa. 2000. IRSp53 is an essential intermediate between Rac and WAVE in the regulation of membrane ruffling. *Nature*. 408:732–735. doi:10.1038/35047107.

Millius, A., N. Watanabe, and O.D. Weiner. 2012. Diffusion, capture and recycling of SCAR/WAVE and Arp2/3 complexes observed in cells by singlemolecule imaging. *J. Cell Sci.* 125:1165–1176. doi:10.1242/jcs.091157.

Moreau, H.D., M. Piel, R. Voituriez, and A.M. Lennon-Duménil. 2018. Integrating Physical and Molecular Insights on Immune Cell Migration. *Trends Immunol.* 39:632–643. doi:10.1016/j.it.2018.04.007.

Mullins, R.D., J.A. Heuser, and T.D. Pollard. 1998. The interaction of Arp2/3 complex

    with actin: Nucleation, high affinity pointed end capping, and formation of branching

    networks of filaments. *Proc. Natl. Acad. Sci. U. S. A.* 95:6181–6186.

    doi:10.1073/pnas.95.11.6181.

Nakagawa, H., H. Miki, M. Nozumi, T. Takenawa, S. Miyamoto, J. Wehland, and J.V.

    Small. 2003. IRSp53 is colocalised with WAVE2 at the tips of protruding

    lamellipodia and filopodia independently of Mena. *J. Cell Sci.* 116:2577–2583.

    doi:10.1242/jcs.00462.

Naqvi, S.N., R. Zahn, D.A. Mitchell, B.J. Stevenson, and A.L. Munn. 1998. The WASp

    homologue Las17p functions with the WIP homologue End5p / verprolin and is

    essential for endocytosis in yeast. *Curr. Biol.* 8:959–962.

Ng, W.P., K.D. Webster, C. Stefani, E.M. Schmid, E. Lemichez, P. Bassereau, and D.A.

    Fletcher. 2017. Force-induced transcellular tunnel formation in endothelial cells.

    Mol. Biol. Cell. 28:2650–2660. doi:10.1091/mbc.E17-01-0080.

Nkosi, P.J., B.S. Targosz, K. Labib, and A. Sanchez-Diaz. 2013. Hof1 and Rvs167 Have

    Redundant Roles in Actomyosin Ring Function during Cytokinesis in Budding

    Yeast. *PLoS One*. 8:1–11. doi:10.1371/journal.pone.0057846.

Oikawa, T., H. Yamaguchi, T. Itoh, M. Kato, T. Ijuin, D. Yamazaki, S. Suetsugu, and T.

    Takenawa. 2004. PtdIns(3,4,5)P 3 binding is necessary for WAVE2-induced

    formation of lamellipodia. *Nat. Cell Biol.* 6:420–426. doi:10.1038/ncb1125.

Park, H., K. Staehling-Hampton, M.W. Appleby, M.E. Brunkow, T. Habib, Y. Zhang, F.

    Ramsdell, H.D. Liggitt, B. Freie, M. Tsang, G. Carlson, S. Friend, C. Frevert, and

    B.M. Iritani. 2008. A point mutation in the murine Heml gene reveals an essential

role for Hematopoietic Protein 1 in lymphopoiesis and innate immunity. *J. Exp. Med.* 205:2899–2913. doi:10.1084/jem.20080340.

Park, J., Y. Kim, S. Lee, J.J. Park, Z.Y. Park, W. Sun, H. Kim, and S. Chang. 2010. SNX18 shares a redundant role with SNX9 and modulates endocytic trafficking at the plasma membrane. *J. Cell Sci.* 123:1742–1750. doi:10.1242/jcs.064170.

Pollard, T.D., and G.G. Borisy. 2003. Cellular Motility Driven by Assembly and Disassembly of Actin Filaments. *Cell*. 112:453–465. doi:10.1016/j.ceb.2005.12.003.

Rakeman, A.S., and K. V. Anderson. 2006. Axis specification and morphogenesis in the mouse embryo require Nap1, a regulator of WAVE-mediated actin branching. *Development*. 133:3075–3083. doi:10.1242/dev.02473.

Robens, J.M., L. Yeow-Fong, E. Ng, C. Hall, and E. Manser. 2010. Regulation of IRSp53-Dependent Filopodial Dynamics by Antagonism between 14-3-3 Binding and SH3-Mediated Localization. *Mol. Cell. Biol.* 30:829–844. doi:10.1128/mcb.01574-08.

Rohatgi, R., L. Ma, H. Miki, M. Lopez, T. Kirchhausen, T. Takenawa, and M.W. Kirschner. 1999. N-WASP activates the Arp2/3 complex and links Cdc42 and phosphoinositide signals to actin assembly. *Mol. Biol. Cell*. 10:122A.

Rotty, J.D., H.E. Brighton, S.L. Craig, S.B. Asokan, N. Cheng, J.P. Ting, and J.E. Bear. 2017. Arp2/3 Complex Is Required for Macrophage Integrin Functions but Is Dispensable for FcR Phagocytosis and In Vivo Motility. *Dev. Cell*. 42:498-513.e6. doi:10.1016/j.devcel.2017.08.003.

Rotty, J.D., C. Wu, E.M. Haynes, C. Suarez, J.D. Winkelman, H.E. Johnson, J.M. Haugh, D.R. Kovar, and J.E. Bear. 2015. Profilin-1 Serves as a gatekeeper for actin

assembly by Arp2/3-Dependent and - Independent pathways. *Dev. Cell*. 32:54–67. doi:10.1016/j.devcel.2014.10.026.

Scita, G., S. Confalonieri, P. Lappalainen, and S. Suetsugu. 2008. IRSp53: crossing the road of membrane and actin dynamics in the formation of membrane protrusions. *Trends Cell Biol.* 18:52–60. doi:10.1016/j.tcb.2007.12.002.

Singh, S.P., and R.H. Insall. 2021. Adhesion stimulates Scar/WAVE phosphorylation in mammalian cells. *Commun. Integr. Biol.* 14:1–4. doi:10.1080/19420889.2020.1855854.

Stefani, C., D. Gonzalez-Rodriguez, Y. Senju, A. Doye, N. Efimova, S. Janel, J. Lipuma, M.C. Tsai, D. Hamaoui, M.P. Maddugoda, O. Cochet-Escartin, C. Prévost, F. Lafont, T. Svitkina, P. Lappalainen, P. Bassereau, and E. Lemichez. 2017. Ezrin enhances line tension along transcellular tunnel edges via NMIIa driven actomyosin cable formation. *Nat. Commun.* 8. doi:10.1038/ncomms15839.

Steffen, A., K. Rottner, J. Ehinger, M. Innocenti, G. Scita, J. Wehland, and T.E.B. Stradal. 2004. Sra-1 and Nap1 link Rac to actin assembly driving lamellipodia formation. *EMBO J.* 23:749–759. doi:10.1038/sj.emboj.7600084.

Sudhaharan, T., S. Hariharan, J.S.Y. Lim, J.Z. Liu, Y.L. Koon, G.D. Wright, K.H. Chiam, and S. Ahmed. 2019. Superresolution microscopy reveals distinct localisation of full length IRSp53 and its I-BAR domain protein within filopodia. *Sci. Rep.* 9:1–17. doi:10.1038/s41598-019-38851-w.

Suetsugu, S., S. Kurisu, T. Oikawa, D. Yamazaki, A. Oda, and T. Takenawa. 2006. Optimization of WAVE2 complex-induced actin polymerization by membrane-bound IRSp53, PIP3, and Rac. *J. Cell Biol.* 173:571–585. doi:10.1083/jcb.200509067.

Szymanski, D.B. 2005. Breaking the WAVE complex: The point of Arabidopsis trichomes. *Curr. Opin. Plant Biol.* 8:103–112. doi:10.1016/j.pbi.2004.11.004.

T, S. 1968. A modified method for lead staining of thin sections. *J Electron Microsc.* 7:158–159.

Takenawa, T., and S. Suetsugu. 2007. The WASP-WAVE protein network: Connecting the membrane to the cytoskeleton. *Nat. Rev. Mol. Cell Biol.* 8:37–48. doi:10.1038/nrm2069.

Taylor, M.J., D. Perrais, and C.J. Merrifield. 2011. A high precision survey of the molecular dynamics of mammalian clathrin-mediated endocytosis. *PLoS Biol.* 9. doi:10.1371/journal.pbio.1000604.

Tsujita, K., A. Kondo, S. Kurisu, J. Hasegawa, T. Itoh, and T. Takenawa. 2013. Antagonistic regulation of F-BAR protein assemblies controls actin polymerization during podosome formation. *J. Cell Sci.* 126:2267–2278. doi:10.1242/jcs.122515.

Ura, S., A.Y. Pollitt, D.M. Veltman, N.A. Morrice, L.M. MacHesky, and R.H. Insall. 2012. Pseudopod growth and evolution during cell movement is controlled through SCAR/WAVE dephosphorylation. *Curr. Biol.* 22:553–561. doi:10.1016/j.cub.2012.02.020.

Urban, E., S. Jacob, M. Nemethova, G.P. Resch, and J.V. Small. 2010. Electron tomography reveals unbranched networks of actin filaments in lamellipodia. *Nat. Cell Biol.* 12:429–435. doi:10.1038/ncb2044.

Veltman, D.M., J.S. King, L.M. Machesky, and R.H. Insall. 2012. SCAR knockouts in Dictyostelium: WASP assumes SCAR's position and upstream regulators in pseudopods. *J. Cell Biol.* 198:501–508. doi:10.1083/jcb.201205058.

Walther, P., and A. Ziegler. 2002. Freeze substitution of high-pressure frozen samples: The visibility of biological membranes is improved when the substitution medium contains water. *J. Microsc.* 208:3–10. doi:10.1046/j.1365-2818.2002.01064.x.

Weaver, A.M., M.E. Young, W.L. Lee, and J.A. Cooper. 2003. Integration of signals to the Arp2/3 complex. *Curr. Opin. Cell Biol.* 15:23–30. doi:10.1016/S0955-0674(02)00015-7.

Weiner, O.D., W.A. Marganski, L.F. Wu, S.J. Altschuler, and M.W. Kirschner. 2007. An actin-based wave generator organizes cell motility. *PLoS Biol.* 5:2053–2063. doi:10.1371/journal.pbio.0050221.

Weiner, O.D., M.C. Rentel, A. Ott, G.E. Brown, M. Jedrychowski, M.B. Yaffe, S.P. Gygi, L.C. Cantley, H.R. Bourne, and M.W. Kirschner. 2006. Hem-1 complexes are essential for Rac activation, actin polymerization, and myosin regulation during neutrophil chemotaxis. *PLoS Biol.* 4:186–199. doi:10.1371/journal.pbio.0040038.

Yamaguchi, H., M. Lorenz, S. Kempiak, C. Sarmiento, S. Coniglio, M. Symons, J. Segall, R. Eddy, H. Miki, T. Takenawa, and J. Condeelis. 2005. Molecular mechanisms of invadopodium formation: The role of the N-WASP-Arp2/3 complex pathway and cofilin. *J. Cell Biol.* 168:441–452. doi:10.1083/jcb.200407076.

Yu, X., and L.M. Machesky. 2012. Cells assemble invadopodia-like structures and invade into matrigel in a matrix metalloprotease dependent manner in the circular invasion assay. *PLoS One*. 7. doi:10.1371/journal.pone.0030605.

Yu, X., T. Zech, L. McDonald, E.G. Gonzalez, A. Li, I. Macpherson, J.P. Schwarz, H. Spence, K. Futó, P. Timpson, C. Nixon, Y. Ma, I.M. Anton, B. Visegrády, R.H. Insall, K. Oien, K. Blyth, J.C. Norman, and L.M. Machesky. 2012. N-WASP

coordinates the delivery and F-actin-mediated capture of MT1-MMP at invasive

pseudopods. *J. Cell Biol.* 199:527–544. doi:10.1083/jcb.201203025.

Zallen, J.A., Y. Cohen, A.M. Hudson, L. Cooley, E. Wieschaus, and E.D. Schejter. 2002.

SCAR is a primary regulator of Arp2/3-dependent morphological events in

Drosophila. *J. Cell Biol.* 156:689–701. doi:10.1083/jcb.200109057.

Zhao, H., A. Pykäläinen, and P. Lappalainen. 2011. I-BAR domain proteins: Linking

actin and plasma membrane dynamics. *Curr. Opin. Cell Biol.* 23:14–21.

doi:10.1016/j.ceb.2010.10.005.

Zhu, Z., Y. Chai, Y. Jiang, W. Li, H. Hu, W. Li, J.W. Wu, Z.X. Wang, S. Huang, and G.

Ou. 2016. Functional Coordination of WAVE and WASP in C. elegans Neuroblast

Migration. *Dev. Cell*. 39:224–238. doi:10.1016/j.devcel.2016.09.029.

Figure 2.1
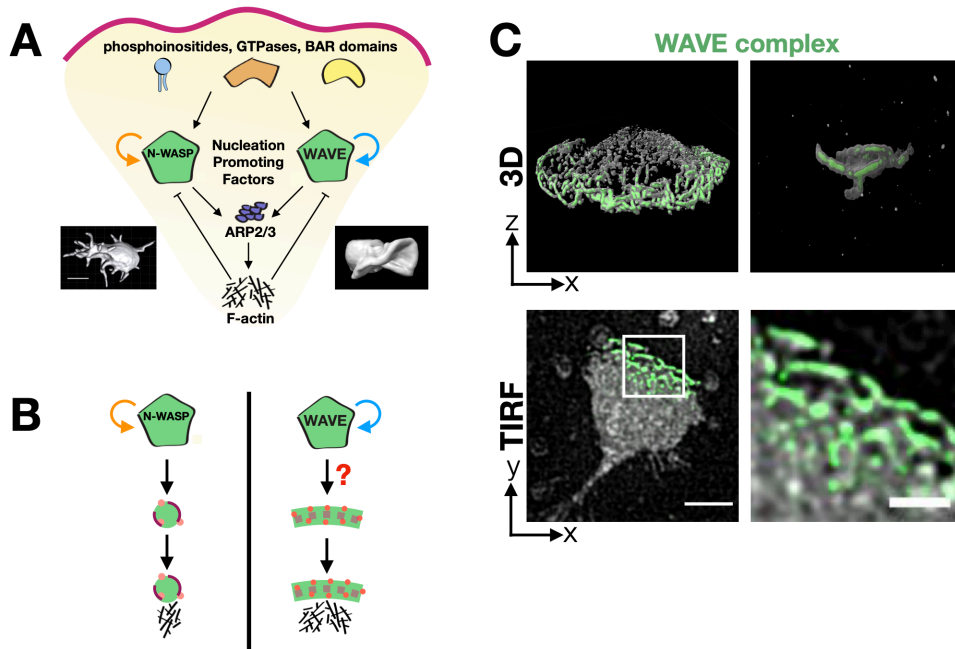
Figure 2.1 How does the WAVE complex achieve the proper spatial organization for lamellipodial generation?

(A) Homologous actin nucleation promoting factors (NPFs) organize different cell morphologies. Given that the homologous NPFs N-WASP and the WAVE complex are both activated by homologous GTPases, associated with homologous BAR domains, stimulated Arp2/3 complex activation, and stripped off the membrane as a function of this actin polymerization, how do they organize different cellular morphologies? N-WASP canonically associates with filopodia, invadopodia, and endocytosis, whereas the WAVE complex associates with sheet-like lamellipodia. Images: left, chick cranial neural crest cell with multiple filopodia from (Genuth et al., 2018) and right, head-on view of a neutrophil-like dHL60 lamellipodium (ChimeraX rendering of a confocal Z-stack).

(B) Schematic of how NPF spatial organization could instruct the resulting actin morphologies. N-WASP's positive feedback results in the focal organization expected for 1-dimensional, finger-like actin structures (Banjade and Rosen, 2014). In order to build lamellipodia, does the WAVE complex's positive feedback result in a linear organization to template 2-dimensional, sheet-like actin structures?

(C) Hem1-eGFP, a fluorescently tagged subunit of the WAVE complex, has a linear organization at tips of lamellipodia in chemoattractant-stimulated (10 nM fMLP) dHL60 cells. Top: 3D imaging of the WAVE complex at tips of extending lamellipodia; left, widefield 3D reconstruction and right, lattice light sheet reconstruction of ruffles from a

head-on view. Bottom: WAVE complex's linear organization viewed from the ventral plasma membrane; simultaneous TIRF imaging of Hem1-eGFP (green) and membrane CellMask DeepRed dye (gray). Scale bars: 5 µm (left) and 2 µm (right). See Video 1.

Figure 2.2
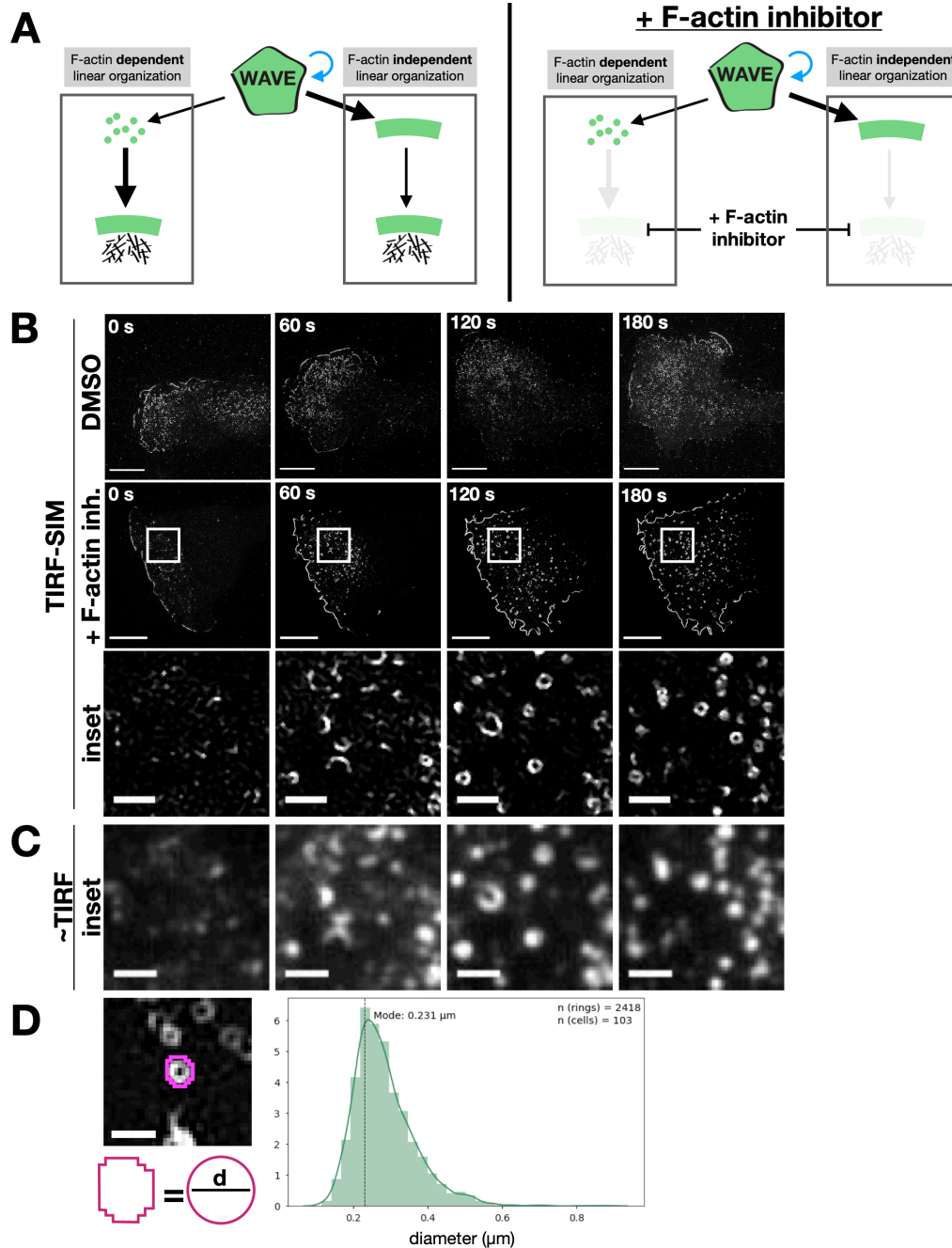
Figure 2.2 WAVE complex forms 230 nm rings in the absence of the actin cytoskeleton

(A) Models of how the WAVE complex could achieve its linear organization. Left: the WAVE complex could achieve its linear organization at the lamellipodial edge in a manner that is dependent on its interactions with the actin cytoskeleton (left) or that is established independently of the actin cytoskeleton (right). Right: addition of F-actin inhibitor can be used to distinguish these models.

(B) Super-resolution total internal reflection fluorescence structured-illumination microscopy (TIRF-SIM) imaging reveals that the WAVE complex forms rings in the absence of actin polymer. dHL60 cells expressing Hem1-eGFP were acutely stimulated with DMSO (top row) or latrunculin A (5 µM final, middle and bottom rows) at 0 seconds. Bottom row are the white boxed insets. Scale bars: 5 µm (top) and 1 µm (insets). See Video 2.

(C) Conventional TIRF resolution comparison highlights the need for super-resolution microscopy to resolve diffraction-limited WAVE complex puncta as rings. Conventional resolution TIRF images were created by sum-projecting the 9 images (3 phases * 3 angles) that construct the TIRF-SIM images of (B). Scale bar: 1 µm. See Video 2.

(D) The WAVE complex forms stereotypical 230 nanometer sized rings. Left, example measurement of fitting the ring's perimeter to a perfect circle and calculating the circle's diameter, d. Right, histogram of diameters of rings across a range of F-actin inhibiting drugs and concentrations, n = 2418 rings from 103 cells, mode = 230 nanometers, median = 270 nanometers (see Fig. S2).

Figure 2.3
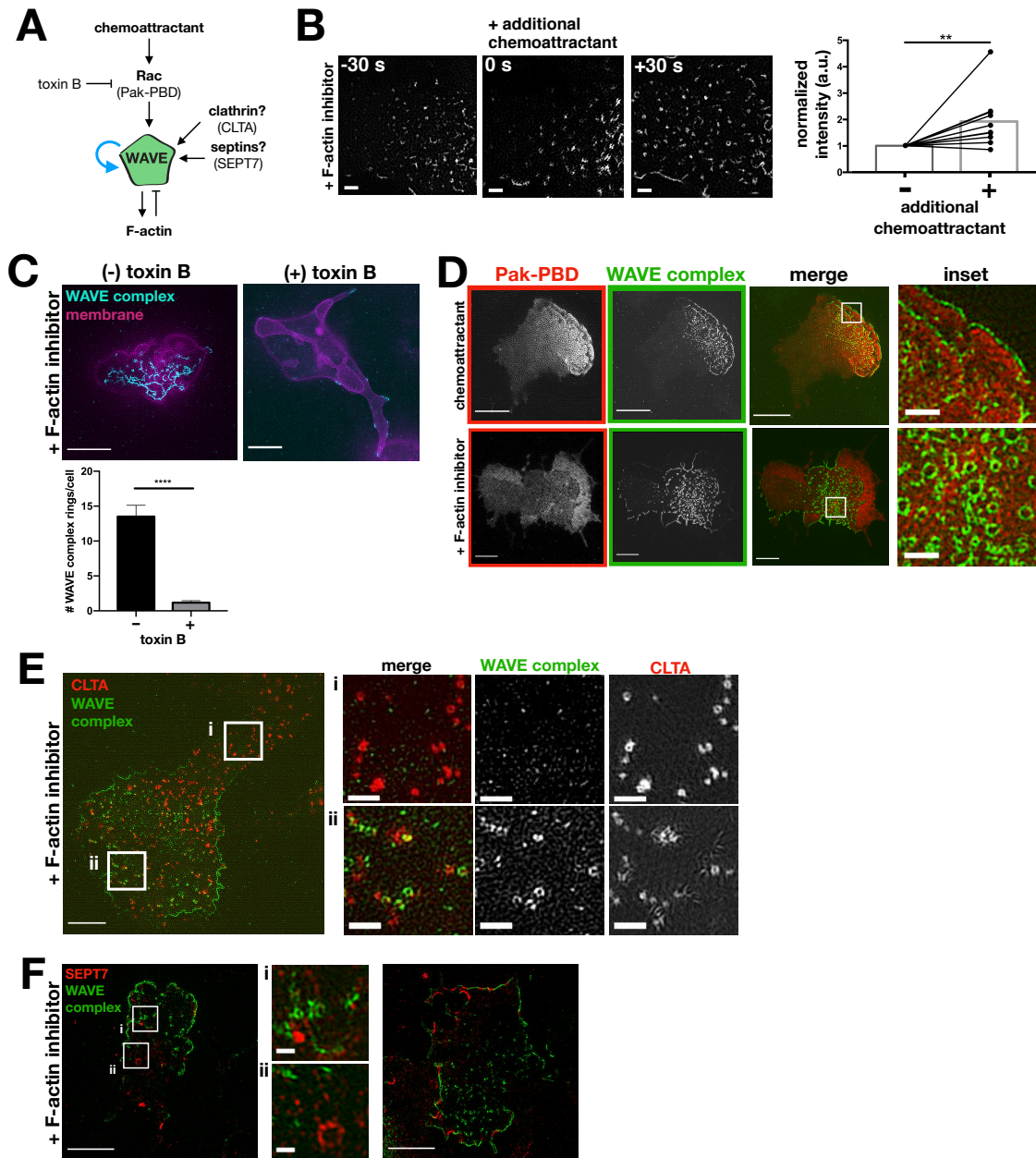
Figure 2.3 The formation of WAVE complex rings is dependent on upstream signals

(A) Potential inputs into the formation of WAVE complex rings.

(B) WAVE complex rings form upon stimulation of additional chemoattractant. Additional WAVE complex (Hem1-eGFP) is recruited to the plasma membrane upon additional chemoattractant stimulation (100 nM fMLP, timepoint 0 s) in F-actin inhibited (500 nM latrunculin B) cells. TIRF-SIM imaging; scale bar: 1 µm. Graph shows normalized integrated intensities of the WAVE complex before (-) and after (+) additional

chemoattractant stimulation of F-actin inhibited cells; n = 10 cells pooled from at least 3 independent experiments of TIRF-SIM imaging; paired t-test two-tailed ** P value = 0.0053 < 0.01.

(C) dHL60s expressing WAVE complex (Hem1-eGFP; cyan) and membrane (CAAX-tagBFP; magenta) treated with (+) or without (-) C. difficile toxin B for at least 4 hrs and acutely treated with latrunculin B (500 nM final). Scale bar: 5 µm. Graph comparing the mean +/- SEM number of the WAVE complex rings in cells treated with (+) and without (-) toxin B; (-) toxin B, n = 37 cells, (+) toxin B n = 66 cells; cells pooled from the same 3 independent experiments; unpaired t-test two-tailed, **** P value < 0.0001.

(D) Colocalization of Pak-PBD-mCherry (red) and Hem1-eGFP (green) in dHL60s treated with chemoattractant (10 nM fMLP final; top) and latrunculin B (500 nM final; bottom). Median filter applied to inset images. Scale bars: 5 µm and 1 µm (inset).

(E) Distribution of endogenously labeled split-mNeonGreen clathrin light chain A (CLTA; red) and Hem1-mCherry (green) dHL60s treated with latrunculin B (500 nM final). Insets (i and ii) shown on right. Scale bars: 5 µm and 1 µm (insets).

(F) Distribution of SEPT7 (immunofluorescence; red) in Hem1-eGFP (green) dHL60 cell line treated with latrunculin B (500 nM final). Left image shows WAVE complex rings (inset i) and septin rings (inset ii). Right image shows complementary localization of Hem1 and SEPT7 along the cell periphery. Scale bars: 5 µm and 0.5 µm (insets).
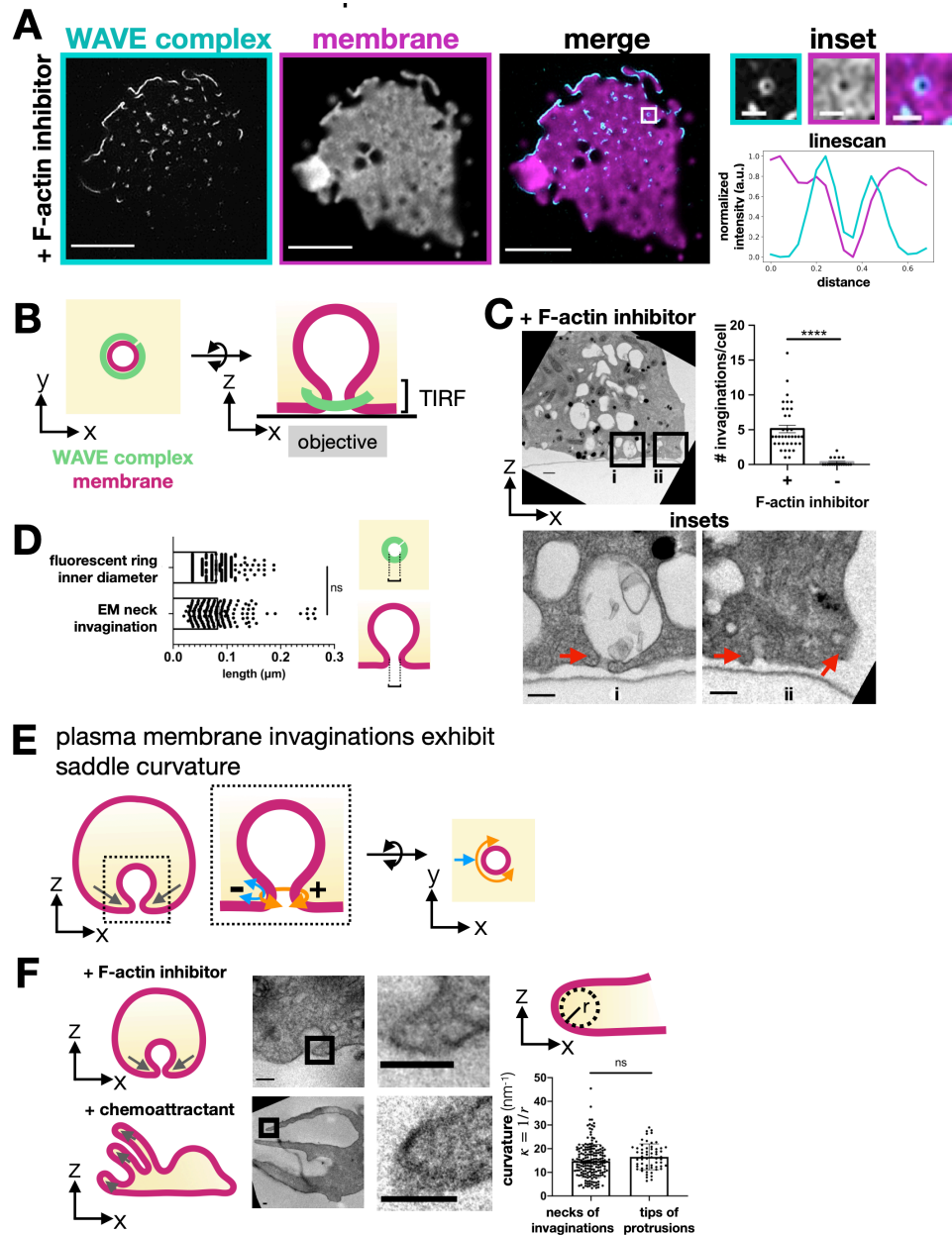
Figure 2.4

Figure 2.4 WAVE complex rings associate with plasma membrane saddle points

(A) TIRF-SIM imaging of the WAVE complex (Hem1-eGFP; cyan) reveals rings localized at the boundary where the plasma membrane (DiD-labeled; magenta) exits the TIRF-SIM plane. Right, insets and a graph of a linescan across a ring. Scale bars: 5 μm and 500 nm (insets). See Video 3.

(B) Schematic of the proposed organization of the WAVE complex ring structure (green) around the neck of a plasma membrane invagination (magenta) as seen from the top, X-Y plane (left) or the side, X-Z plane (right).

(C) Transmission electron micrographs of a cross-section of dHL60s treated with latrunculin B (500 nM). Red arrows point to membrane invaginations. Scale bars: 500 nm (top) and 200 nm (insets). Graph comparing the number of membrane invaginations per serial section of cells treated with or without F-actin inhibitor (500 nM latrunculin B). Graph shows mean +/- SEM; (+) F-actin inhibitor n = 37 cells, (-) F-actin inhibitor n = 18 cells; Mann-Whitney test with two-tailed **** P value < 0.0001.

(D) Graph comparing the length across the neck of invaginations by electron microscopy (EM) to the inner diameter of the fluorescent Hem1 rings of dHL60s treated with latrunculin B (500 nM). Schematic represents where measurements were made. Graph shows mean +/- SEM; EM of neck invaginations n = 190 from 38 cells, fluorescent ring inner diameter n = 222 from 4 cells; Mann-Whitney test with two-tailed ns, not significant P value ~0.39 > 0.05. This finding supports the possibility that the WAVE complex enriches around the necks of membrane invaginations.

(E) Schematic of a plasma membrane invagination's saddle curvature. The necks of invaginations display saddle geometry of positive curvature in one axis (orange; the curve around the invagination neck) and negative curvature in the other axis (blue; the curve perpendicular to the invagination neck).

(F) Curvature comparison of the necks of invaginations and tips of protrusions. Electron micrographs of dHL60s treated with F-actin inhibitor (top; 500 nM latrunculin B) and dHL60s treated with chemoattractant (bottom; 100 nM fMLP) show that the curvature at the necks of invaginations and the tips of protrusions are similar. Graph shows mean +/- SEM; invaginations n = 190 from 28 cells, protrusions n = 59 from 19 cells; unpaired t-test two-tailed ns, not significant P value = 0.074 > 0.05. Curvature, κ, defined as 1/r where r is the radius. Scale bar: 100nm.

Figure 2.5
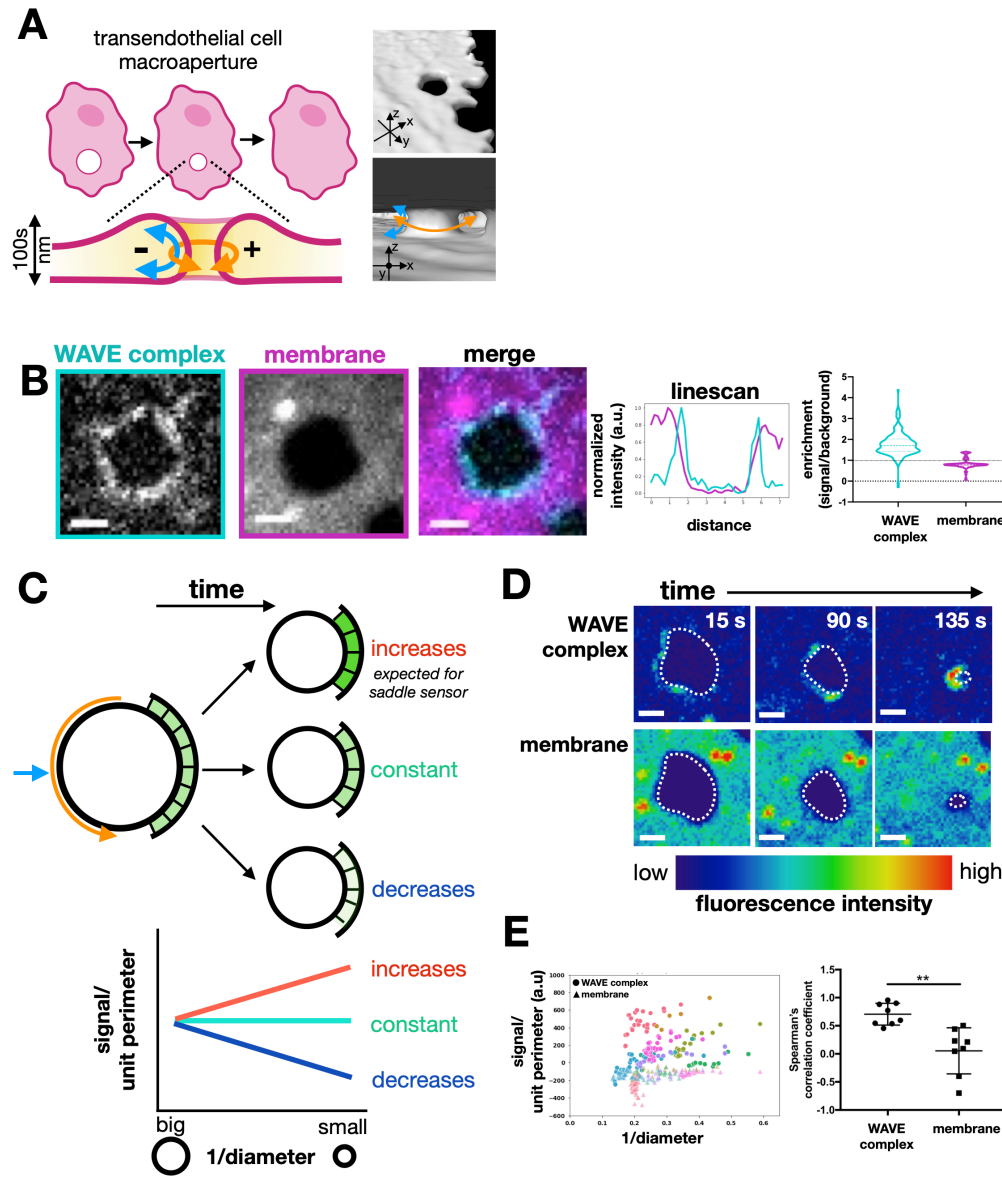
Figure 2.5 WAVE complex enriches to transendothelial cell macroaperture (TEM) tunnel saddle points

(A) Schematic of a transendothelial cell macroaperture closure and saddle geometry. Right: ChimeraX renderings of spinning disk confocal imaging of a HUVEC cell that was treated with Y27632 (50 µM) to induce transendothelial cell macroapertures, labeled with a membrane dye (CellMask DeepRed), and then fixed with paraformaldehyde. Top: tilted view. Bottom: view from inside the cell facing a transendothelial cell macroaperture and its saddle geometry.

(B) The WAVE complex localizes to transendothelial cell macroapertures. A HUVEC cell expressing eGFP-tagged Nap1, a WAVE complex subunit (cyan), and stained with membrane dye CellMask DeepRed (magenta) was treated with Y27632 (50 µM). Spinning disk confocal imaging, scale bar: 2 µm. Left graph: linescan across the transendothelial cell macroaperture; WAVE complex (cyan) and membrane dye (magenta). Right graph: violin plot of enrichment, which was measured as the ratio between the signal intensity per unit area at the transendothelial cell macroapertures compared to the background intensity per unit area. A value of 1 indicates no enrichment at the transendothelial cell macroaperture (small dotted line), and a value above 1 indicates enrichment. Each time point throughout transendothelial cell macroaperture closure was considered as a single data point; WAVE complex and membrane both had n = 164 from 8 transendothelial cell macroapertures from at least 3 independent experiments per condition.

(C) Schematic of different potential molecular behaviors during transendothelial cell macroaperture closure. As transendothelial cell macroapertures close, the local concentration (signal per unit length) could increase, remain constant, or decrease. A saddle geometry sensor would increase its local concentration until the transendothelial cell macroaperture closure reaches the sensor's preferred positive radius of curvature.

(D) Time-lapse images of the WAVE complex (top) and the membrane (bottom) as a transendothelial cell macroaperture closes. Images in each set have the same intensity scale in a LUT that eases the visualization of signal enrichment. The dotted line outlines the transendothelial cell macroaperture membrane mask. Spinning disk confocal imaging; time in seconds; scale bar: 2 µm. See Video 4.

(E) WAVE complex enriches to closing transendothelial cell macroapertures. Left: graph of the WAVE complex (circles) and membrane (triangles) signal per unit perimeter as a transendothelial cell macroaperture closes. Each color represents a single transendothelial cell macroaperture over time. The WAVE complex shows higher enrichment at smaller (more positively curved) transendothelial cell macroapertures, suggesting a preference for membrane saddles with high positive curvature. Right: graph of mean +/- SEM of the Spearman's correlation coefficient of each closing transendothelial cell macroaperture; the WAVE complex and membrane each had n = 8 transendothelial cell macroapertures from at least 3 independent experiments; unpaired t-test two-tailed ** P value = 0.0012 < 0.0021.

Figure 2.6
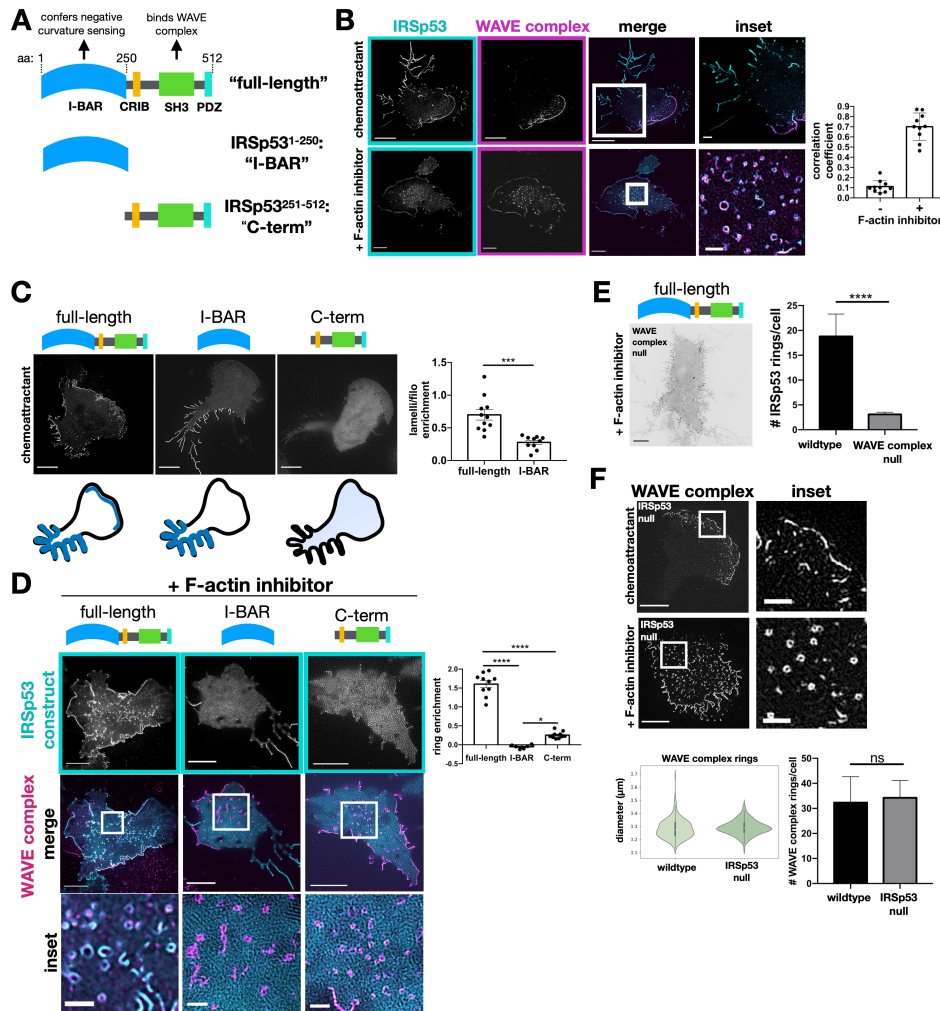
Figure 2.6 WAVE complex recruits IRSp53 to lamellipodia and regions of saddle curvature

(A) Domain structure of IRSp53 structure/function constructs. The I-BAR domain confers negative membrane curvature sensing, and the SH3 domain enables binding to the WAVE complex.

(B) IRSp53 and the WAVE complex colocalize at lamellipodia (top). Following actin depolymerization, they colocalize at rings (bottom). IRSp53 also localizes to filopodia-like structures, whereas the WAVE complex is excluded from those regions (top). dHL60 cells expressing both IRSp53-eGFP (cyan) and Hem1-mCherry (magenta) were treated with chemoattractant (10 nM fMLP, top) or F-actin inhibitor (500 nM latrunculin B, bottom). TIRF-SIM imaging; scale bars: 5 μm and 1 μm (insets). See Video 5. Graph measuring colocalization between IRSp53 and Hem1 in conditions with or without F-actin inhibition. Barplot shows mean +/- standard deviation of Manders M1 correlation coefficient (fraction of IRSp53 in compartments containing Hem1); (+) F-actin inhibition

n = 10 cells, (-) F-actin inhibition n = 10 cells; cells pooled from at least 3 independent experiments of TIRF-SIM imaging.

(C) The IRSp53 structure/function constructs have different localization patterns in chemoattractant stimulated dHL60s. Full-length IRSp53 enriches to lamellipodia and filopodia-like structures; I-BAR enriches to filopodia-like structures but not to lamellipodia; and C-term is cytosolic. Summary of the IRSp53 construct localization below. Cells with comparable expression levels were imaged (Fig. S4C). TIRF-SIM imaging; scale bar: 5 µm. Right, graph of IRSp53 enrichment ratio of signal at lamellipodia per unit area vs signal at filopodia per unit area for full-length and I-BAR IRSp53 constructs. Graph shows mean +/- SEM; full-length n = 11 cells; I-BAR n = 10 cells; cells pooled from at least 3 independent experiments per condition; unpaired t-test two-tailed *** P value = 0.0002 < 0.001.

(D) F-actin inhibited dHL60s expressing IRSp53 constructs and the WAVE complex. Middle row shows IRSp53-eGFP construct (cyan) overlay with Hem1-mCherry (magenta) rings. The I-BAR and C-term constructs fail to enrich robustly as rings. TIRF-SIM imaging; scale bars: 5 µm and 1 µm (insets). Graph comparing the signal enrichment of IRSp53 constructs' signal per unit area of rings (defined by Hem1-mCherry) over the background per unit area. Graph displays the mean +/- SEM where all rings within a cell were aggregated; full-length n = 10 cells from 3 independent experiments, I-BAR n = 6 cells from 2 independent experiments, C-term n = 10 cells from 2 independent experiments; one-way ANOVA with two-tailed P value < 0.0001 with Tukey's multiple comparisons follow-up tests, **** P values < 0.0001, * P value = 0.01 < 0.05.

(E) Full-length IRSp53 fails to enrich as rings in the absence of the WAVE complex. Inverted display of IRSp53-eGFP expressed in a WAVE complex-null dHL60 cell treated with latrunculin B (500 nM). TIRF-SIM imaging; scale bar: 5 µm. Graph comparing the mean +/- SEM number of IRSp53 rings in wildtype and WAVE complex-null cells; wildtype n = 37 cells, WAVE complex-null n = 66 cells; cells pooled from the same 3 independent experiments; unpaired t-test two-tailed **** P value < 0.0001.

(F) The WAVE complex in IRSp53-null dHL60 cells. The WAVE complex localizes to lamellipodia in chemoattractant stimulated cells (10 nM fMLP; top) and as rings in F-actin inhibited cells (500 nM latrunculin B; bottom). TIRF-SIM imaging; scale bars: 5 µm and 1 µm (inset). Left graph: violin plot of the WAVE complex rings in wildtype and IRSp53-null cells; wildtype: n = 293 rings from 13 cells, IRSp53-null: n = 470 rings from 10 cells; cells pooled from at least 3 independent experiments per condition. Diameters were measured in the same fashion shown in Fig. 2D. Right graph: graph comparing the mean +/- SEM number of the WAVE complex rings in wildtype and IRSp53-null cells; wildtype, n = 10 cells, IRSp53-null n = 16 cells; cells pooled from the same 3 independent experiments; unpaired t-test two-tailed ns, not significant P value = 0.88 > 0.05.

Figure 2.7
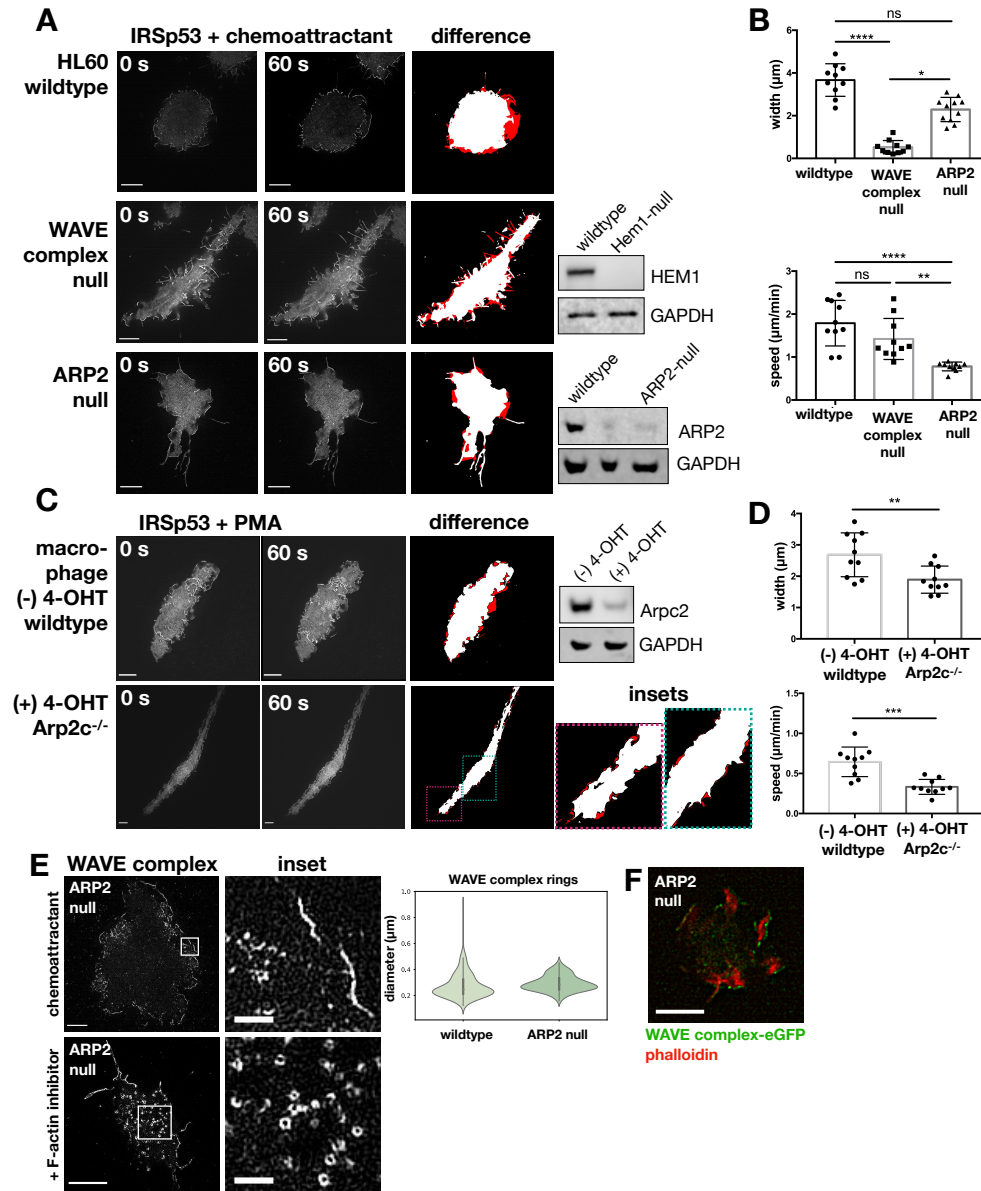
Figure 2.7 The WAVE complex, but not the ARP2/3 complex, is required for the formation of sheet-like protrusions

(A) ARP2/3 complex-disrupted dHL60 cells form sheet-like protrusions. IRSp53, a marker of both filopodial and lamellipodial protrusions, was imaged in chemoattractant stimulated wildtype (top row), WAVE complex-null (middle row), and ARP2-null (bottom row) cells. Middle column panel is 60 seconds after chemoattractant stimulation of the corresponding left column panel. Right column panel displays the difference (red) to highlight regions of protrusions. TIRF-SIM imaging; scale bar: 5 µm. See Video 7.

Western blots for HEM1 and ARP2 with GAPDH as a loading control are shown for wildtype and CRISPR/Cas9 edited cells.

(B) Graphs comparing the protrusions across cells. Top graph: mean +/- SEM of the average protrusion widths (microns) after 1 minute of chemoattractant stimulation; wildtype n = 10 cells, WAVE complex-null n = 10 cells, and ARP2-null n = 11 cells; cells pooled from at least 3 independent experiments per condition; Kruskal-Wallis test P value < 0.0001 with Dunn's multiple comparisons follow-up tests **** P value < 0.0001, * P value = 0.0141, ns, not significant P value = 0.0717 > 0.05. Bottom graph: mean +/- SEM of the average protrusion speed (micron per minute) post chemoattractant stimulation; wildtype n = 10 cells, WAVE complex-null n = 10 cells, and ARP2-null n = 11 cells; cells pooled from at least 3 independent experiments per condition; Kruskal-Wallis test P value < 0.0001 with Dunn's multiple comparisons follow-up tests **** P value < 0.0001, ** P value = 0.0029, ns, not significant P value > 0.99.

(C) Arp2c-disrupted primary mouse bone marrow macrophages form sheet-like protrusions. IRSp53-eGFP was imaged in PMA stimulated (100 nM) wildtype (- 4-OHT) and Arp2c-/- (+ 4-OHT) cells. Panels displayed similarly to (A). TIRF-SIM imaging; scale bar: 5 μm. See Video 8. Western blot for Arp2c and GAPDH as a loading control is shown.

(D) Graphs comparing the protrusions across macrophages. Top graph: mean +/- SEM of the average protrusion widths (microns) after 1 minute of PMA stimulation; wildtype (- 4-OHT) n = 10 cells and Arp2c-/- (+ 4-OHT) n = 10 cells; cells pooled from 2 experiments per condition; Mann-Whitney test ** P value = 0.0052. Bottom graph: mean +/- SEM of the average protrusion speed (micron per minute) post PMA stimulation; wildtype (- 4-OHT) n = 10 cells and Arp2c-/- (+ 4-OHT) n = 10 cells; cells pooled from 2 experiments per condition; Mann-Whitney test *** P value = 0.0002.

(E) The WAVE complex in ARP2-null dHL60 cells. The WAVE complex (Hem1-eGFP) localizes to sheet-like protrusions in chemoattractant stimulated ARP2-null cells (10 nM fMLP; top) and as rings in F-actin inhibited ARP2-null cells (500 nM latrunculin A; bottom). TIRF-SIM imaging; scale bars: 5 μm and 1 μm (insets). See Video 9. Violin plot of the WAVE complex ring diameters in wildtype and ARP2-null cells; wildtype n = 210 from 10 cells, ARP2-null n = 179 from 10 cells; cells pooled from at least 3 independent experiments per condition. Diameters measured in the same fashion shown in Fig. 2D.

(F) F-actin behind the WAVE complex in ARP2-null sheet-like protrusions. ARP2-null dHL60 cell expressing Hem1-eGFP (green) treated with chemoattractant (100 nM fMLP) and stained with phalloidin (red). TIRF imaging; scale bar: 5 μm.
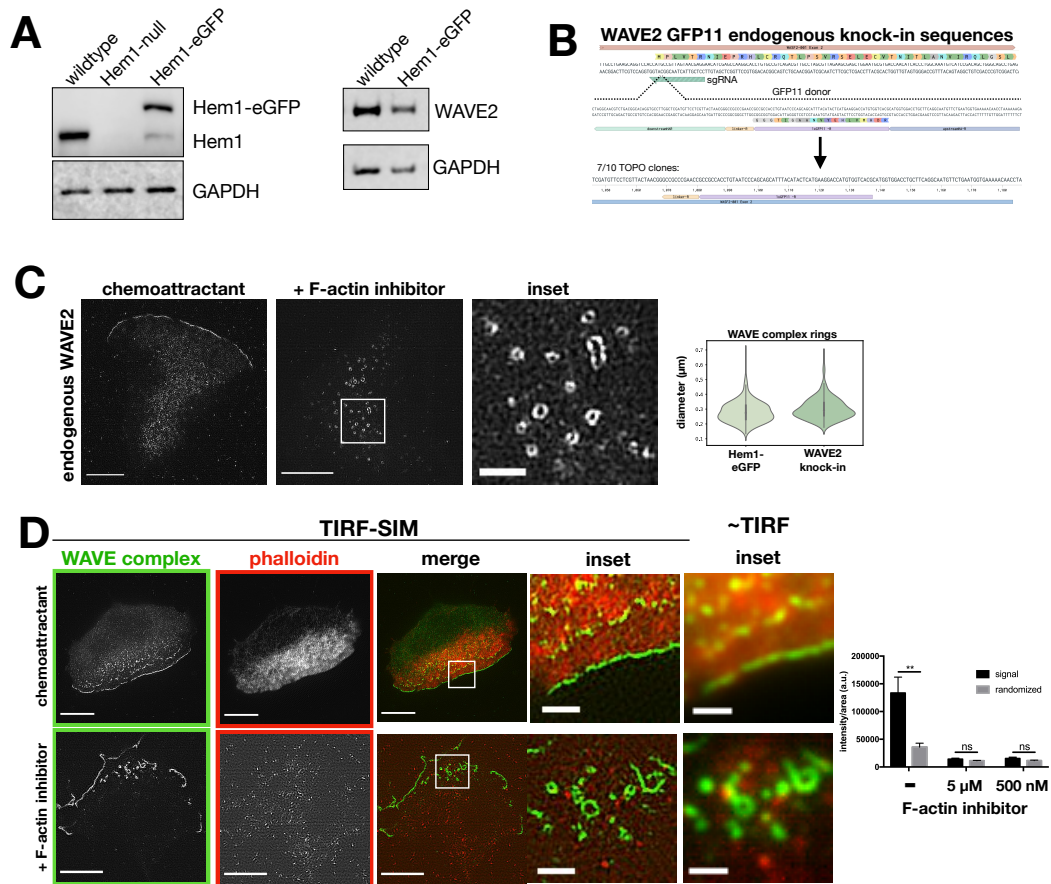
Figure S2.1

Figure S2.1 WAVE complex rings are not due to overexpression of WAVE complex subunits and are devoid of F-actin

(A) HEM1 and WAVE2 expression levels in the Hem1-eGFP HL60 cell line used throughout the study. Left: Western blot of HEM1 and GAPDH in wildtype, HEM1-null, and Hem1-eGFP HL60 cell lines. Right: Western blot of WAVE2 and GAPDH in wildtype and Hem1-eGFP HL60 cell lines.

(B) WAVE2 split-GFP endogenous knock-in sequences. In a GFP1-10 expressing cell line, CRISPR/Cas9 cuts the N-terminus of WAVE2's exon 2 and the cell repairs with a GFP11 donor flanked with WAVE2 homology arms.

(C) Endogenous localization of WAVE2 in split-GFP knock-in dHL60 cells. Cells treated with chemoattractant (10 nM fMLP) or F-actin inhibitor (500 nM latrunculin B). TIRF-SIM imaging; scale bars: 5 μm and 1 μm (inset). Violin plot of the WAVE complex ring diameters in Hem1-eGFP and WAVE2 knock-in cells treated with F-actin inhibitor (500 nM latrunculin B); Hem1-eGFP n = 293 rings from 13 cells, WAVE2 knock-in n = 305 from 10 cells; cells pooled from at least 2 independent experiments per condition. Diameters measured in the same fashion shown in Fig. 2D.

(D) Images of dHL60 cells expressing Hem1-eGFP (green) treated with chemoattractant (100 nM fMLP; top) or F-actin inhibitor (5 µM latrunculin B; bottom) that were then fixed and stained with phalloidin (red). TIRF-SIM imaging; scale bars: 5 µm and 1 µm (insets). ~TIRF inset images are the sum projection of SIM angles. Graph shows mean +/- SEM of phalloidin intensity/area; (-) F-actin inhibitor n = 14 cells, 5 µM F-actin inhibitor n = 10 cells, 500 nM F-actin inhibitor n = 10 cells; cells pooled from at least 3 independent experiments; multiple t-tests, ** P value = 0.003 < 0.01, ns, not significant 5 µM lat P value = 0.14 > 0.05, and 500 nM lat P value = 0.17 > 0.05.

Figure S2.2
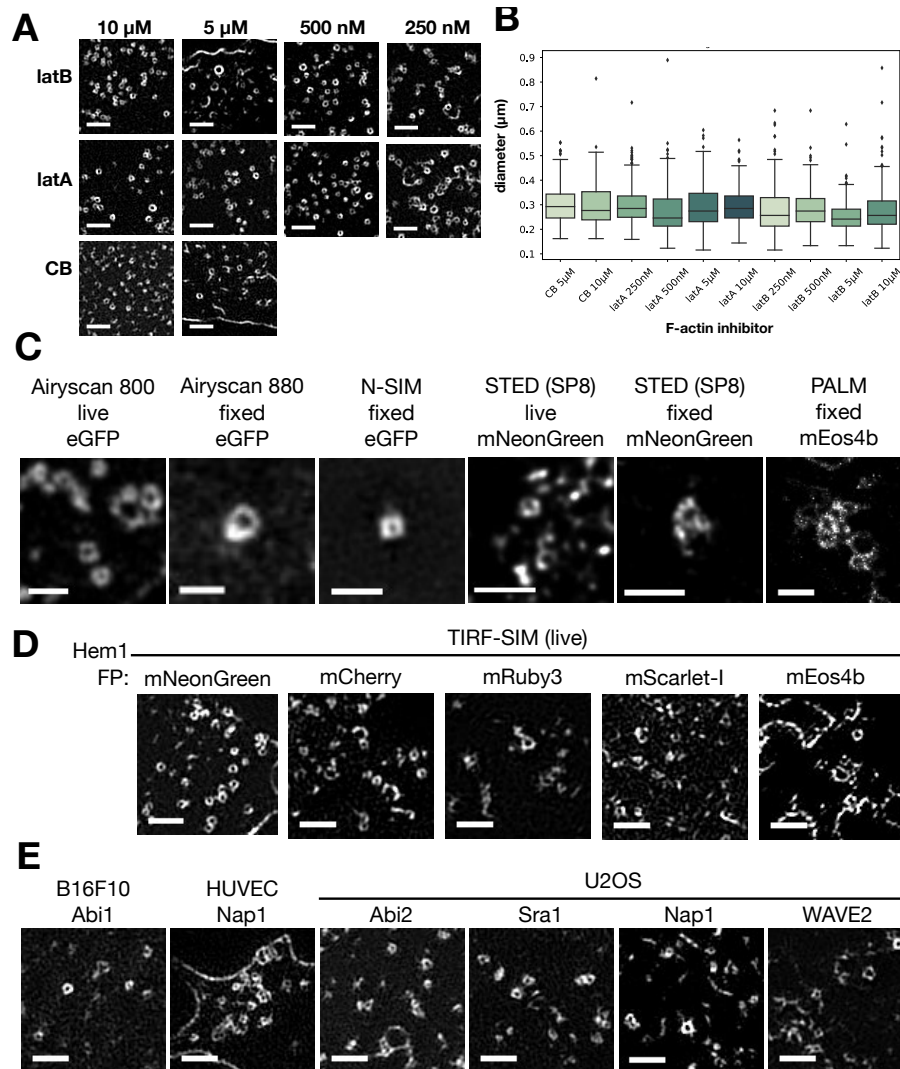
Figure S2.2 WAVE complex rings observed for multiple cell lines, labeled subunits, microscopy techniques, and actin inhibitors

(A) Zoomed-in TIRF-SIM images of Hem1-eGFP rings across different drug conditions: 250 nM, 500 nM, 5 µM, 10 µM (final) of latrunculin B (latB), latrunculin A (latA), and cytochalasin B (CB). Scale bar: 1 µm.

(B) Boxplots (interquartile range) of ring diameters across drug conditions as measured in Fig. 2D. Each condition has at least 10 cells from at least 3 independent experiments per condition; ensemble histogram in Fig. 2D.

(C) Multiple super-resolution techniques in live or fixed cell conditions of Hem1 tagged with different fluorescent proteins all show ring structures. Microscopes and techniques used: Airyscan 800 (Zeiss), Airyscan 880 (Zeiss), N-SIM (Nikon), SP8 STimulated

Emission Depletion (STED, Leica), and photoactivated localization microscopy (PALM) on B Huang lab (UCSF) microscope. All cells treated with latrunculin B (500 nM). Scale bar: 1 µm.

(D) Hem1 tagged with different fluorescent proteins (FP) show ring structures. All imaged with TIRF-SIM and treated with latrunculin B (500 nM). Scale bar: 1 µm.

(E) Different eGFP tagged WAVE complex subunits in B16F10 (Mus musculus skin melanoma cells), HUVECs (human umbilical vein endothelial cells), and U2OS (Homo sapiens bone osteosarcoma) cell lines show ring structures. All cells treated with latrunculin B (500 nM). TIRF-SIM imaging; scale bar: 1 µm.
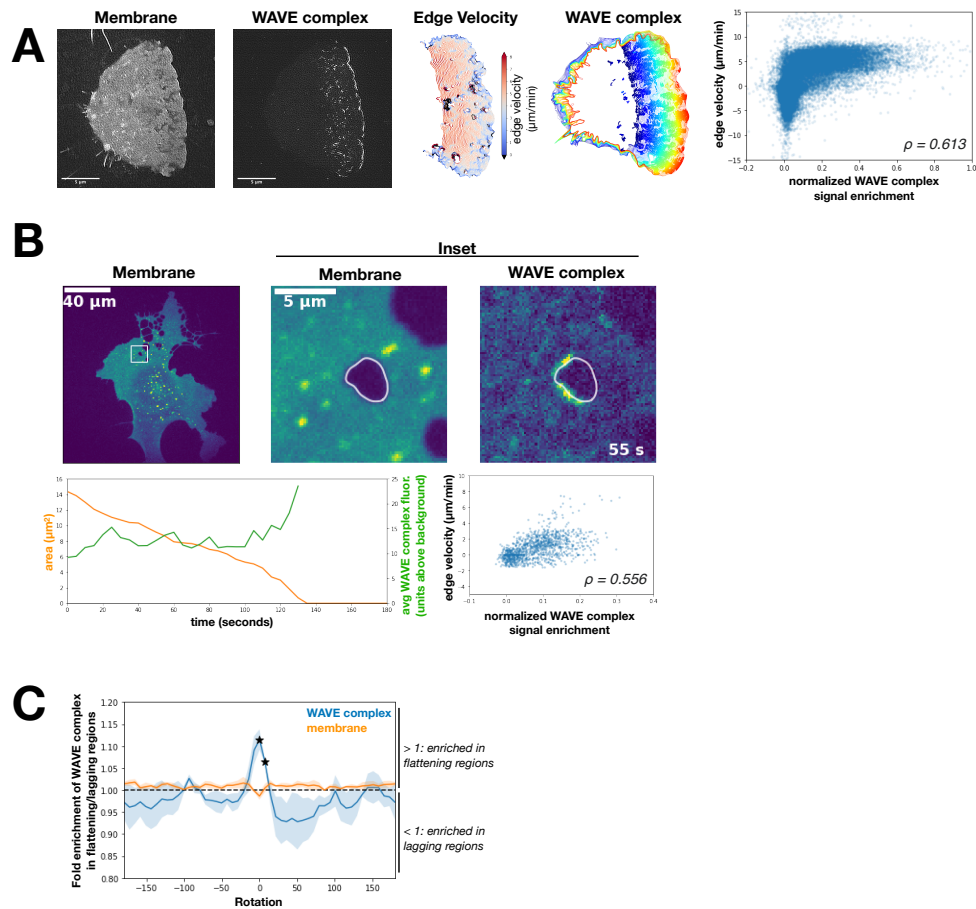
Figure S2.3

Figure S2.3 The WAVE complex enriches at flattening membrane regions

(A) WAVE complex signal enrichment versus membrane edge velocity in a migrating dHL60 cell. From left to right: image of the membrane (CellMask DeepRed) at a single time point, image of the WAVE complex (Hem1-eGFP) at a single time point, successive cell outlines of the leading edge over time, WAVE complex localization (solid colors) over time, and graph of normalized WAVE complex signal enrichment versus membrane edge velocity (Spearman's correlation ρ = 0.613). TIRF-SIM images; scale bar: 5 µm.

(B) WAVE complex signal enrichment versus membrane edge velocity in a closing transendothelial cell macroaperture. Images (top row): HUVEC cell expressing WAVE complex-eGFP (Nap1-eGFP) treated with ROCK inhibitor Y27632 (50 µM) to generate transendothelial cell macroapertures. Left: membrane (CellMask DeepRed), middle: inset of membrane channel, right: inset of WAVE complex signal. Spinning disk confocal imaging; scale bars: 40 µm and 5 µm (insets). Left graph: area of transendothelial cell macroaperture (orange) and the average WAVE complex fluorescence signal (units above background; green) over time (seconds). Right graph: normalized WAVE

complex signal enrichment versus macroaperture membrane edge velocity throughout closure (Spearman's correlation ρ = 0.556).

(C) The WAVE complex fold enrichment at flattening over lagging regions at different image rotations. "Flattening" defined as the membrane becoming less positively curved (toward flat or negatively curved), "lagging" defined as the membrane becoming more positively curved, and "rotation" refers to the degree to which the WAVE complex signal is rotated around the transendothelial cell macroaperture. At each point, the fold enrichment of WAVE complex signal in flattening over lagging regions is calculated. The peak at zero rotation indicates that the highest enrichment was due to the colocalization of the curvature and fluorescent features of interest in the unrotated configuration, indicating a true correlation. N = 3 transendothelial cell macroapertures from 2 independent experiments were averaged. Rotations that are statistically significantly different from 1 (P value <= 0.05) are indicated with a star.

Figure S2.4

A High expression of IRSp53 forms rings in the presence of F-actin

chemoattractant

B WAVE complex rings

C IRSp53 structure/function — full-length IRSp53 expression

D full-length — I-BAR

E
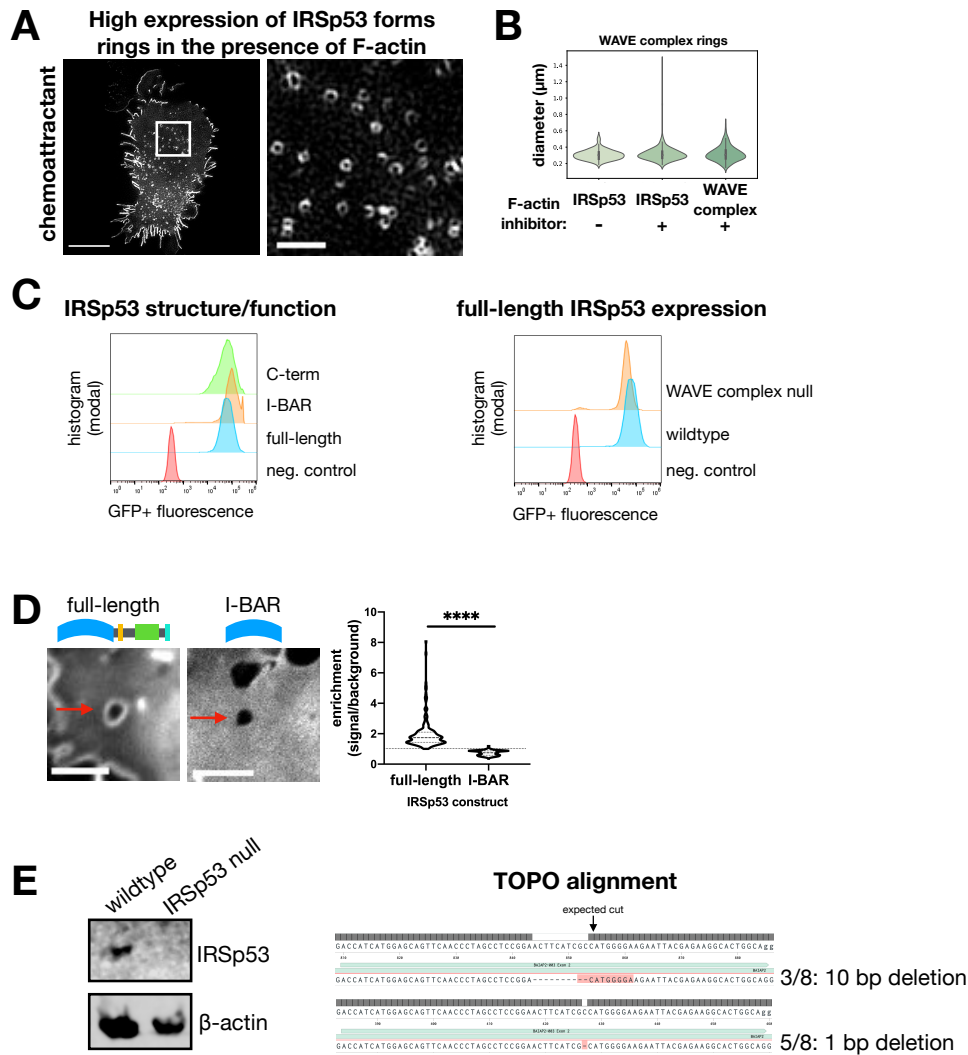
Figure S2.4 Supplemental IRSp53 data

(A) dHL60 cell with high expression of IRSp53-eGFP stimulated with chemoattractant (10 nM fMLP) shows that high levels of IRSp53 induce ring structures even in the presence of an intact actin cytoskeleton. TIRF-SIM imaging, scale bars: 5 μm (left) and 1 μm (inset). See Video 6.

(B) Graph comparing the diameters of the WAVE complex rings with F-actin inhibition to IRSp53 rings with (+) or without (-) F-actin inhibition (500 nM latrunculin B). Diameters measured in the same fashion shown in Fig. 2D. Violin plot of rings; IRSp53 without (-) F-actin inhibition n = 157 from 10 cells, IRSp53 with (+) F-actin inhibition n = 483 from 10 cells, the WAVE complex (+) F-actin inhibition n = 202 from 13 cells; cells pooled from at least 3 independent experiments per condition; Kruskal-Wallis test, nonsignificant P value = 0.56 > 0.05.

(C) IRSp53-eGFP structure/function expression levels are comparable across cell lines. Left: IRSp53 structure/function constructs in wildtype cells. Right: full-length IRSp53 in wildtype and WAVE complex-null HL60s. Flow cytometry data graphed with FlowJo.

(D) Images of HUVECs expressing full-length IRSp53 (left) or I-BAR only domain (right) at Y27632-induced transendothelial cell macroapertures. Spinning disk confocal imaging; red arrows point to a transendothelial cell macroaperture; scale bar: 5 μm. See Video 4. Graph: violin plot of the enrichment of full-length IRSp53 and I-BAR domain at transendothelial cell macroapertures; measurements made in the same fashion as Fig. 5B. Each time point across transendothelial cell macroaperture closure was considered as a single data point: full-length n = 186 and I-BAR n = 291, both from 4 transendothelial cell macroapertures from at least 3 independent experiments per condition; Mann-Whitney test of significance two-tailed **** P value < 0.0001.

(E) Characterization of CRISPR/Cas9 mediated IRSp53 knock out in HL60s. Left: immunoblot of wildtype and IRSp53-null clonal HL60 line. β-actin was used as a loading control. Right: TOPO alignment of the gene-edited region of exon 2 reveals indels of the IRSp53-null clonal HL60 line.

Figure S2.5
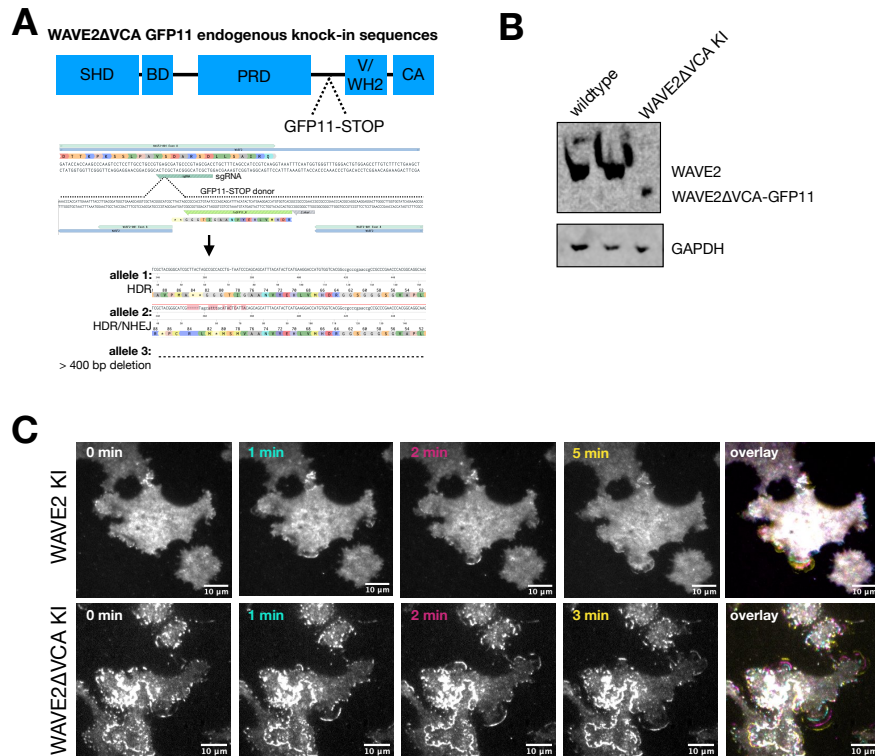
Figure S2.5 WAVE2ΔVCA localizes to the leading edge of sheet-like protrusions

(A) Generation of WAVE2ΔVCA cells with the split-GFP endogenous CRISPR/Cas9 editing system. Schematic of WAVE2 domains and editing (SHD: Scar homology domain, BD: basic domain, PRD: proline-rich domain, V/WH2: WASP-homology 2 domain, CA: central acidic domain). In a GFP1-10 expressing cell line, CRISPR/Cas9 with a guide targeting WAVE2's VCA region cuts and the cell repairs with a HDR donor containing GFP11 and two stop codons. After generating clonal cell lines, the edited region was PCR amplified and analyzed with MiSeq and CRISPresso2. The edited alleles are: one HDR allele, one mixed HDR/NHEJ allele (that resulted in a stop codon), and one allele with a deletion larger than 400 base pairs.

(B) Western blot of WAVE2 and GAPDH in wildtype and WAVE2ΔVCA GFP11 knock-in HEK-293T lines.

(C) WAVE2ΔVCA localizes to the leading edge of sheet-like protrusions. Timelapse of endogenously split-GFP edited full-length WAVE2 ("FL KI," top row) and WAVE2ΔVCA ("ΔVCA KI," bottom row) HEK-293T cells stimulated with 300 nM PMA. TIRF imaging; scale bars: 10 µm. See Video 10.

93

CHAPTER THREE

WASP INTEGRATES SUBSTRATE TOPOLOGY AND CELL POLARITY TO GUIDE NEUTROPHIL MIGRATION

SUMMARY

To control their shape and movement, cells leverage nucleation promoting factors (NPFs) to regulate when and where they polymerize actin. Here we investigate the role of the immune-specific NPF WASP during neutrophil migration. Endogenously-tagged WASP localizes to substrate-induced plasma membrane deformations. Super-resolution imaging of live cells reveals that WASP preferentially enriches to the necks of these substrate-induced membrane invaginations, a distribution that could support substrate pinching. Unlike other curvature-sensitive proteins, WASP only enriches to membrane deformations at the cell front, where it controls Arp2/3 complex recruitment and actin polymerization. Despite relatively normal migration on flat substrates, WASP depletion causes defects in topology sensing and directed migration on textured substrates. WASP therefore both responds to and reinforces cell polarity during migration. Surprisingly, front-biased WASP puncta continue to form in the absence of Cdc42. We propose that WASP integrates substrate topology with cell polarity for 3D guidance by selectively polymerizing actin around substrate-induced membrane deformations at the leading edge. A misregulation of WASP-mediated contact guidance could provide insight into the immune disorder Wiskott-Aldrich syndrome.

INTRODUCTION

Motile cells must coordinate many types of actin networks to achieve directed migration (Blanchoin et al., 2014). Nucleation promoting factors (NPFs) control when and where branched actin is assembled, with different NPFs giving rise to different types of actin networks (Pollitt and Insall, 2009; Rottner et al., 2017). For example, WAVE forms broad, propagating waves at the leading edge that pattern the sheet-like actin networks that generate lamellipodia (Weiner et al., 2007; Veltman et al., 2012; Leithner et al., 2016). In contrast, N-WASP has a punctate distribution and forms finger-like actin networks that comprise podosomes (Isaac et al., 2010; Nusblat et al., 2011; Mizutani et al., 2002), invadopodia (Yamaguchi et al., 2005; Yu et al., 2012; Yu and Machesky, 2012), and sites of endocytosis (Kessels and Qualmann, 2002; Merrifield et al., 2004; Benesch et al., 2005). While the function of WAVE and N-WASP is well understood, other NPFs remain poorly characterized. This includes WASP, an N-WASP homologue specific to the hematopoietic lineage. WASP was initially identified through its role in Wiskott-Aldrich syndrome (Derry et al., 1994), an immune disorder characterized by abnormal platelets, eczema, and recurrent infection (Wiskott, 1937; Aldrich et al., 1954). However, despite the homing defects of immune cells in WASP-deficient patients and animal models (Ochs et al., 1980; Snapper et al., 2005; De Noronha et al., 2005; Westerberg et al., 2005; Jones et al., 2013), how WASP contributes to actin organization and cell migration remains poorly understood.

The function of WASP in vertebrates has been inferred from the function of its homologue N-WASP. However, important functional divergences have been reported

between these proteins (Isaac et al., 2010; Nusblat et al., 2011). In particular, N-WASP

cannot compensate for the loss of WASP in T cell chemotaxis (Jain and Thanabalu,

2015). The basis of WASP's role in immune cell guidance remains unknown. Do

functions ascribed to N-WASP such as endocytosis and podosome/invadopodia

formation also underlie WASP-deficient immune cell migration defects? Or does WASP

participate in additional aspects of physiology during immune cell migration? The

functional roles of actin nucleators and NPFs have successfully been elucidated through

analysis of spatiotemporal dynamics and loss-of-function phenotypes (Bear et al., 1998;

Rogers et al., 2003; Kunda et al., 2003; Weiner et al., 2007; Miki et al., 1998; Nakagawa

et al., 2001; Taunton et al., 2000; Benesch et al., 2002; Duleh and Welch, 2010;

Zuchero et al., 2009; Sagot et al., 2002; Yang et al., 2007; Manor et al., 2015). Here we

use this approach to probe WASP's contribution to neutrophil migration.

By fluorescently labeling endogenous WASP, we find its primary localization to be focal

puncta on the ventral surface of cells. These structures are not sites of clathrin-

mediated endocytosis but are instead triggered by interaction with the substrate.

Specifically, sites where the substrate induces inward plasma membrane curvature lead

to local WASP enrichment. Super-resolution imaging reveals that WASP concentrates

at the necks of substrate-induced invaginations, a distribution that supports engagement

with substrate features. Typically, curvature-responsive proteins show the same degree

of curvature sensitivity in different parts of the same cell (Zhao et al., 2017; Lou et al.,

2019). In contrast, WASP integrates cell polarity with membrane curvature sensing and

enriches at sites of inward curvature only in the front half of the cell. This spatial

restriction could enable the cell to disengage with the substrate at the trailing edge while prioritizing engagement in the direction of advance. Through analyzing knockouts, we find that WASP is essential for Arp2/3 complex recruitment and actin polymerization at sites of membrane deformation at the cell front, linking the substrate's topology with the migration machinery. Consistent with this idea, WASP-null cells exhibit migration defects on patterned substrates, while their motility on flat substrates is relatively unaffected. Our data establishes a role for WASP in connecting substrate topology and cell polarity with migration in neutrophils.

RESULTS

WASP enriches to puncta that associate with the substrate

Because of its key role in the immunological disorder Wiskott-Aldrich Syndrome, WASP

has traditionally been studied through its loss-of-function phenotypes in immune cells

from patients and animal models of the disease (Ochs et al., 1980; Snapper et al., 2005;

De Noronha et al., 2005; Westerberg et al., 2005; Jones et al., 2013). Less attention

has been paid to its localization and dynamics in cells. Therefore, we turned to the

easily manipulated human neutrophil-like cell line HL-60 to better understand the

spatiotemporal dynamics of WASP and how these attributes might inform its function. In

a previous report, exogenously expressed WASP was shown to enrich to the tip of the

leading edge and to membrane-associated puncta in HL-60s (Fritz-Laylin et al., 2017).

However, protein overexpression can lead to ectopic localization (Doyon et al., 2011).

To better profile WASP's functional properties, we generated a fluorescently tagged

protein at the endogenous locus in HL-60 cells using CRISPR-Cas9 and homology-

directed repair (**Fig. S1A-C**).

WASP knock-in HL-60 cells were confined in 2D to flatten the ventral surface of the cell

against the coverslip and facilitate imaging by TIRF microscopy. Endogenous WASP

localized to membrane-associated puncta and the periphery of the leading edge, a

distribution which was broadly consistent with exogenous WASP (Fritz-Laylin et al.,

2017). However, enrichment of WASP to puncta in the front half of the cell, separate

from the cell periphery, was more strongly pronounced than previously appreciated and

proved to be the dominant pattern of WASP localization (**Fig. 1A and 1C; Video 1**).

Additionally, WASP puncta were remarkably stationary, often persisting at the same position relative to the coverslip on the minute time scale despite bulk cell displacement (**Fig. 1B**). Because N-WASP has been implicated in clathrin-mediated endocytosis (CME) (Kessels and Qualmann, 2002; Merrifield et al., 2004; Benesch et al., 2005), we investigated whether WASP puncta represent sites of CME. Endogenous WASP and endogenous clathrin light chain A failed to co-localize at the cell front (**Fig. 1D-E; Fig. S1D-E; Video 2**). In addition, both clathrin-dependent and independent endocytic pathways have been shown to occur at the rear of polarized HL-60 cells (Davis et al., 1982; Subramanian et al., 2018). Therefore, front-biased WASP puncta (**Fig. 1E**) do not appear to mark sites of endocytosis.

Other documented roles for WASP/N-WASP include the formation of invasive structures (Yu et al., 2012; Yu and Machesky, 2012; Isaac et al., 2010; Nusblat et al., 2011; Mizutani et al., 2002; Yamaguchi et al., 2005) and facilitation of cell adhesion (Misra et al., 2007; Zhang et al., 2006) and spreading (Misra et al., 2007; Liu et al., 2013). Neutrophils have a limited capacity for generating invadopodia or podosomes, failing to invade soft substrates like matrigel or to form their characteristic actin-vinculin rosettes (Cougoule et al., 2012). We therefore investigated whether WASP puncta are linked to cell adhesion. While neutrophils do not generate the long-lived focal adhesions found in many adherent cell lines (Yuruker and Niggli,

1992; Lämmermann and Sixt, 2009), we hypothesized that the fixed location of WASP puncta relate to adhesion with the underlying substrate. To test this, we confined cells between two glass coverslips and treated them with EDTA, a calcium and magnesium chelator that blocks integrin-ligand binding and therefore prevents adhesion (Zhang and Chen, 2012). Under inelastic confinement, neutrophils can migrate in an adhesion-independent manner (Malawista et al., 2000), using friction to chimney between the glass surfaces like a climber squeezing between two rock faces. In the absence of integrin-based adhesion, we found that WASP puncta continued to form on the cell surface but were no longer stationary relative to the substrate and instead began undergoing retrograde flow (**Fig. 1F; Video 3**). Additionally, WASP puncta are less stable for cells lacking integrin adhesions, extinguishing significantly closer to their point of nucleation at the cell front (**Fig. 1G**). The induced motility of WASP puncta when cell-substrate adhesions are removed suggests that stationary WASP puncta normally depend on engagement with the substrate. This finding is supported by previous observations that WASP-null neutrophils have an impaired ability to adhere to and cross cell monolayers under shear flow (Zhang et al., 2006) while neutrophils expressing only constitutively active WASP demonstrate increased adhesion and migration in flow chambers (Keszei et al., 2018).

Based on these data, we hypothesized that WASP puncta couple the lamellipodial actin network to the cell substrate to aid in motility. We next asked which substrate features are involved in WASP recruitment.

WASP is curvature-sensitive and sorts to sites of saddle curvature

Positive (inward) membrane curvature can organize N-WASP both in reconstituted systems (Takano et al., 2008) and in live cells plated on nanopatterns (Lou et al., 2019). We sought to test whether inward curvature similarly templates WASP organization. However, neutrophils only loosely adhere to their substrate (Lämmermann and Sixt, 2009), limiting the ability of nanopatterns to precisely deform the cell membrane. We therefore forced cells into closer apposition to the substrate by overlaying them with agarose and incubating samples until cells were flattened (**Fig. 2A**). Because WASP/N-WASP natively associates with spherical membrane invaginations like endocytic pits, we used polystyrene beads as our membrane-deforming agents. The use of spherical beads enabled us to explore 2D curvatures that are inaccessible with most fabricated nanopatterns. Specifically, beads allowed us to probe (1) two dimensions of positive (inward) isotropic curvature at the body of the bead-induced invagination and (2) saddle curvature at the invagination neck. Because curvature sensitive proteins can discriminate between 1D and 2D curvatures (Iversen et al., 2015; Larsen et al., 2020), it is important to have tools that can probe 2D curvature in cells. Additionally, this approach has the benefit of being highly tunable through the availability of beads of different diameters (and therefore radii of curvature). Finally, use of commercially available, inert beads removed the cost and throughput limitations of nanofabrication techniques like electron beam lithography (Li et al., 2019).

As HL-60s migrated over beads, WASP was recruited within seconds to all beads and persisted while they were under the lamellipod (**Fig. 2B-C; Video 4**). To determine

whether this enrichment is curvature sensitive, we compared WASP recruitment in cells

migrating over 100 and 200 nm beads (**Fig. 2D**). *In vitro*, enrichment of curvature-

sensitive proteins to different sized liposomes is normalized per unit area (Bhatia et al.,

2009). Applying this normalization scheme to our data, we found a three-fold

enrichment of WASP to the smaller bead size (higher radius of curvature) (**Fig. 2E**).

This finding is consistent with measurements for curvature-sensitive proteins, including

BAR domain-containing proteins (Bhatia et al., 2009) and components of CME (Zhao et

al., 2017), suggesting that WASP recruitment is sensitive to curvature. To probe

whether membrane deformation could similarly be an organizing cue for physiological

substrates, we plated cells on coverslips coated with a thin layer of fluorescent collagen

fibers (Elkhatib et al., 2017). Even without agarose confinement, cells were deformed by

collagen fibers, and endogenous WASP was recruited to cell-fiber interfaces (**Fig. S2**).

WASP was strikingly consistent in its recruitment across multiple beads under the same

lamellipod. In adherent cells plated on nanopatterns, curvature-sensitive proteins are

normally heterogeneous in their degree of recruitment to adjacent nanobars (Lou et al.,

2019; Zhao et al., 2017). This led us to compare the strength of WASP recruitment with

that of other known curvature sensors through measuring enrichment to sites of bead-

induced membrane deformation (**Fig. 2F-G**). First, we investigated the WASP/N-WASP-

interacting, BAR domain-containing protein FBP17. FBP17 activates N-WASP *in vitro*

(Takano et al., 2008) and has been posited as an organizer of N-WASP-dependent

actin nucleation in endocytosis (Tsujita et al., 2006) and at the leading edge of polarized

cells (Tsujita et al., 2015). In COS-1 cells FBP17 also exists as membrane-associated

puncta that are reminiscent of our WASP puncta (Tsujita et al., 2015). Despite co-localization of endogenous FBP17 and WASP at puncta biased toward the cell front (**Fig. S3A-B)**, FBP17 was neither required for WASP puncta formation nor WASP recruitment to bead-induced membrane deformations since these behaviors persisted in FBP17 knockout cells (**Fig. S3F-G**). Furthermore, the degree of FBP17 enrichment to beads was significantly poorer than that of WASP (**Fig. 2G**). Similarly, endogenous clathrin light chain A (LCa), which enriches to bead-induced membrane invaginations in MDA-MB-231 cells (Elkhatib et al., 2017), exhibited less robust recruitment to beads than WASP in neutrophils (**Fig. 2G**). Finally, since WAVE complex exhibits a preference for saddle curvatures (Pipathsouk et al., 2019), we measured its enrichment to bead-induced invaginations. While WAVE complex transiently enriched to some beads, it failed to persistently enrich (**Fig. 2G**). WASP appears to be unusual among other curvature-sensitive proteins in its consistent marking of 500 nm-scale membrane invaginations in neutrophils.

While we found that curvature informs WASP recruitment, it remained unclear what type of membrane geometry was driving this process since bead-induced invaginations have both positive (inward) isotropic curvature (along the bead body) and saddle curvature (at the invagination neck). To elucidate WASP's preferred curvature, we turned to live-cell 2D and 3D super-resolution stimulated emission depletion (STED) microscopy of the membrane at bead-induced invaginations. Using 3D STED, we achieved a lateral (x-y) resolution of 160 ± 6 nm and an axial (x-z) resolution of 160 ± 16 nm (**Fig. S4A-E**). We began with cells confined onto fluorescent 500 nm beads to clearly separate the

isotropically positive invagination body from the saddle-shaped neck. We observed two

different classes of membrane organization around 500 nm beads, each of which

correlated to distinct patterns of WASP enrichment (**Fig. 3A**). In one set of cases, the

membrane wrapped around a bead but failed to cinch around the bead bottom, forming

an inverted "U" shape (∩). In this case, WASP lined the entirety of the bead-induced

membrane invagination (**Fig. 3A**, top panel). In a second set of cases, the membrane

formed a cinched neck under the bead, making an "omega" shape (Ω) (**Fig. 3A**, bottom

panels). When this morphology was observed, WASP no longer surrounded the entire

structure but was instead concentrated onto the sides of the invagination neck. At

smaller, 200 nm bead-induced invaginations, we could not resolve any membrane

necks, and WASP organization at these sites appeared to match that of "U" shaped

invaginations (**Fig. 3B**). In contrast, others have reported saddle-enrichment of N-

WASP (Kaplan et al., 2020) and the yeast orthologue Las17 (Mund et al., 2018) on this

size scale using STORM to image CME in fixed cells. Finally, we compared WASP

intensities at uniformly coated 200 and 500 nm bead-induced invaginations measured

with 3D STED and again found an increased enrichment to beads with higher radii of

curvature (**Fig. S4F**).

We next investigated the temporal relation between the "U" and "omega" invagination

states, and, using time-lapse 3D STED, were able to record "U"-shaped membranes

closing around beads into "omega" shapes (**Fig. 3C; Video 5**). We found that not only

does WASP reorganize during neck closing, but also additional WASP is recruited from

the environment, highlighting a preference for the geometry found at the neck of 500 nm

bead-induced invaginations (**Fig. 3D**). Finally, when analyzing the ventral surface of cells with 2D STED, we see a higher proportion of "U"-shaped invaginations with uniform WASP closer to the cell front and omega-shaped invaginations with punctate WASP further back (**Fig. 3E**), supporting our observations that over time the membrane reconfigures from open-necked to closed-neck and that WASP reorganizes as more favorable neck geometries arise (**Fig. 3F**).

Dual inputs of membrane curvature and cell polarity inform WASP recruitment
WASP is consistently recruited to sites of inward membrane deformation. However, if WASP enriched everywhere the membrane was invaginated by the substrate, cells might engage with the coverslip across their entire surface and be unable to productively migrate. We next investigated whether there was spatial information restricting where WASP can respond to curvature.

Established curvature-sensitive proteins typically enrich to a given plasma membrane morphology irrespective of location in the cell (Zhao et al., 2017; Lou et al., 2019). Strikingly, WASP only enriched to beads in the front half of the cell (**Fig. 4A**). When a cell ran into a bead, WASP was recruited within seconds (**Fig. 2B**). Then, as the cell migrated over the bead and it progressed to the cell rear, WASP signal was lost (**Fig. 4B-C; Fig. S5A**). The disappearance of WASP correlated more strongly with puncta position than duration, as puncta that nucleated further from the cell front exhibited shorter lifetimes (**Fig. S5B**). To ensure that WASP disappearance was not a consequence of poor membrane deformation at the cell rear, we imaged the membrane

106

and confirmed that 500 nm bead-induced membrane deformations persisted at the cell rear but lost WASP signal (**Fig. 4D**). Additionally, using 3D STED we observed that bead-induced invaginations lost WASP over time, as they moved toward the cell rear (**Fig. S5C**). Invaginations at the cell front were consistently WASP-positive, while invaginations at the rear of the same cells did not have WASP despite displaying similar membrane geometries (**Fig. S5D**). To our knowledge, this is the first report of a curvature-sensitive protein that integrates both membrane curvature and cell polarity.

To investigate how WASP combines cell polarity inputs with its curvature-sensitive membrane enrichment, we sought to better understand the inputs that specify the region permissive for WASP recruitment. WASP/N-WASP is known to link Cdc42 to Arp2/3 complex activation (Rohatgi et al., 1999; Higgs and Pollard, 2000), and Cdc42 activity is polarized towards the leading edge of migrating neutrophils (Yang et al., 2016). However, WASP puncta continued to form in a polarized fashion in Cdc42 knockout cells (**Fig. 4E-F**). Therefore, despite the strong link between Cdc42 and WASP, Cdc42 is not necessary for WASP foci formation or polarization in neutrophils. As an orthogonal approach to remove potential polarity input from both Cdc42GTP and RacGTP binding, we rescued WASP-null cells with a WASP mutant lacking the Cdc42- and Rac-interactive binding (CRIB) domain and observed similarly polarized puncta (**Fig. S5E**).

Our data show that WASP puncta formation and curvature sensitivity occur only in a permissive, front-polarized region. WASP identifies membrane invaginations as they

form at the cell front and then leaves around the time they cross the cell midline (**Fig. 4G**). We next investigated how this polarization impacts the cytoskeleton.

WASP links membrane topology with the actin cytoskeleton

To determine whether actin polymerization occurs at WASP puncta, we transduced WASP knock-in cells with a TagRFP-T-tagged Arp3 subunit of the Arp2/3 complex. Arp3 co-localizes with endogenous WASP puncta at the cell front (**Fig. 5A-B**). Unlike in CME where N-WASP signal peaks roughly ten seconds before that of Arp3 (Taylor et al., 2011) , we were unable to resolve a temporal offset between recruitment of WASP and Arp3 at puncta. Additionally, in comparing the spatial distributions of WASP and Arp3 across the cell length, we find significant overlap between the signals (**Fig. 5C**). Given these observations, we conclude that Arp3 behavior closely mirrors that of WASP at puncta. Enrichment of an actin nucleator to these sites suggests polymerization is occurring and that native WASP puncta are filamentous actin (F-actin) rich structures.

Next, we sought to determine whether actin polymerization occurs at bead-induced invaginations, and, if so, whether this process depends on WASP. Confining our Arp3-tagged cells onto beads, we found that the Arp2/3 complex, like WASP, enriches to nearly all bead-induced invaginations at the cell front (**Fig. 5D**). However, repeating these measurements in WASP-null HL-60s led to a roughly 50% reduction in the number of beads that induced Arp2/3 puncta formation and a significant decrease in the integrated Arp3 intensity at beads despite similar expression levels in both backgrounds (**Fig. 5D-F**). Additionally, while there persisted a band of Arp3 signal immediately behind

the leading edge, Arp3 signal across the rest of the cell was quite uniform, and puncta outside of those formed at beads were rare (**Fig. 5D**). Therefore, the Arp2/3 complex is normally recruited to sites of inward membrane deformation through its association with WASP.

Finally, we used the live-cell actin probe SiR-actin to assay for F-actin at bead induced invaginations and found co-localization of SiR-actin with WASP at beads under the cell front (**Fig. 5G-H**). Our finding that WASP plays an important role in linking membrane deformation to the actin cytoskeleton led us to next investigate how WASP-dependent actin structures affect neutrophil migration.

Integration of topographical features during neutrophil migration depends on WASP
Given the clear *in vivo* phenotype of WASP-null neutrophils (Snapper et al., 2005; De Noronha et al., 2005; Westerberg et al., 2005; Jones et al., 2013) and our observation that WASP recruitment is regulated by inward membrane curvature, we hypothesized that WASP-dependent migration may be particularly acute for cells challenged by a complex, membrane-deforming environment. To asses this, we probed the role of WASP during migration on nanoridged substrates designed to mimic the aligned collagen fibers cells encounter *in vivo* (Ray et al., 2017).

First, we tested whether WASP puncta form at sites of inward curvature generated by nanoridges, as they did at beads (**Fig. 2)** and on collagen fibers (**Fig. S2**)**.** Indeed, WASP puncta accumulate on nanoridges where the pattern pushes into the cell (**Fig.**

6A-B). Unlike focal adhesions that form on both the ridges and grooves of these patterns (Ray et al., 2017), WASP localized specifically to the positive (inward) curvature-inducing ridges. Additionally, despite long stretches of contact between cells and the patterns, WASP enrichment remained punctate and failed to continuously localize across ridges under the cell. The fact that curvature alone does not explain WASP patterning on nanoridges suggests that there may be other inputs determining the spatial scale of WASP self-organization (Li et al., 2012; Banjade and Rosen, 2014; Case et al., 2019).

To determine whether WASP enrichment on nanoridges reflected a role in migration, we next compared the effect of flat versus textured substrates on the migration of wild type and WASP-null HL-60s (**Fig. S1**). There was a modest difference between the total distance travelled by wild type and WASP-null cells on flat substrates (15%-19% decrease) (**Fig. 6C; Video 6**). In contrast, WASP-null cells plated on nanoridges exhibited a greater reduction in total distance travelled compared to wild type cells (27-30% decrease) (**Fig. 6D, Video 7**). When we decomposed cell movement into axes that aligned with or were perpendicular to the nanopatterns, the observed migration defect was explained by a decrease in the ability of WASP-null cells to orient their migration along patterns. In fact, WASP-null cells moved ~60% less than wild type cells in the direction of the patterns while moving ~30% <u>more</u> than wild type cells in the direction perpendicular to the patterns. This is further reflected by a large difference in the ratio of aligned to perpendicular migration between wild type and WASP-null cells (**Fig. 6E**). The observed increase in perpendicular migration as opposed to a decrease in

110

migration along both axes highlights a defect in the ability of WASP-null cells to sense and respond to the nanopatterned features of their substrate. Indeed, wild type HL-60 cells largely aligned with the ridges, while WASP-null cells did so with much lower frequency (**Fig. 6F, Video 7**). Wild type cells also moved more persistently along ridges and sometimes followed them across the entire field of view (>665 µm) (**Fig. 6G, bottom left**). In contrast, persistent migration along nanoridges occurred less frequently in WASP KO cells (**Fig. 6G, bottom right**).

To better understand how wild type and WASP-null cells differentially explore space on flat versus patterned substrates, we calculated the mean squared displacement (MSD) for each cell type in these different environments. In the absence of patterns, the MSDs of wild type and WASP KO cells were largely indistinguishable (**Fig. 6H, top**). However, on nanoridges the MSD was significantly larger for wild type cells than WASP KO cells across increasing time offsets (**Fig. 6H, bottom**). Due to an apparent difference in persistence between wild type and WASP KO cells on nanoridges (**Fig. 6G, bottom; Video 7**), we also calculated a persistence ratio, defined here as the ratio between displacement from the starting position and total distance travelled. In the absence of patterns the persistence ratio steadily falls off over increasing time windows for both wild type and WASP-null cells since there is no input biasing the direction of movement (**Fig. 6I, top**). Conversely, in the presence of nanoridges wild type cells are significantly more persistent than WASP-null cells on both short and long time scales (**Fig. 6I, bottom**).

Taken together, these observations reveal an essential role for WASP in substrate topology sensing and contact guidance in neutrophils (**Fig. 6J**).

DISCUSSION

Neutrophils need to navigate complex three-dimensional paths through dense extracellular matrices *in vivo* (Lämmermann et al., 2013). To move in this environment, a cell must be able to sense its physical surroundings and coordinate its movement with the features of its substrate. Our work suggests that WASP plays a role in mediating this process. First, WASP helps detect the topology of the substrate by enriching to sites of inward, substrate-induced membrane deformation (**Fig. 2 and Fig. 3**). WASP then facilitates recruitment of the Arp2/3 complex for local actin assembly, thereby coupling substrate features with the cytoskeleton (**Fig. 5**). WASP functions as a dual integrator of cell polarity and membrane curvature, enriching to membrane invaginations only at the cell front (**Fig. 4**). To our knowledge, this is the first report of curvature sensitivity that is informed by physical location within a cell. Through these characteristics, WASP is able to (1) identify substrate features on which to anchor the cell, (2) pattern actin polymerization to leverage substrate contact sites for locomotion, and (3) constrain substrate engagement to regions that yield productive migration. As a consequence of these features, WASP-null neutrophils are particularly defective at coordinating substrate topology with cell guidance (**Fig. 6**).

While the importance of WASP has long been appreciated due to its role in Wiskott-Aldrich syndrome, its contribution to neutrophil migration has been unclear. In animal models of this disease, neutrophils are defective at homing to sterile wounds (Jones et al., 2013) and sites of infection (Snapper et al., 2005; Kumar et al., 2012). However, *in vitro* WASP-null neutrophils have shown mixed phenotypes. Some studies have

113

reported defective migration (Ochs et al., 1980; Fritz-Laylin et al., 2017) while others found no defect (Zicha et al., 1998; Zhang et al., 2006). One possible reason for this discrepancy is our finding that WASP is primarily used during migration in complex environments where substrate topology sensing and engagement play a critical role.

Much of what we know about WASP function has been inferred from that of its ubiquitously expressed homologue N-WASP, which plays a key role in clathrin-mediated endocytosis (Merrifield et al., 2004; Benesch et al., 2005; Kessels and Qualmann, 2002), among other functions (Isaac et al., 2010; Nusblat et al., 2011; Mizutani et al., 2002; Yamaguchi et al., 2005; Yu et al., 2012; Yu and Machesky, 2012; Zhang et al., 2006; Misra et al., 2007; Liu et al., 2013). Whether WASP plays a similar role in immune cells was not known. Our work reveals that a critical function of WASP in neutrophils is divergent from the canonical functions of N-WASP. However, we find some parallels between WASP and N-WASP; both proteins use membrane invagination to locally polymerize actin via Arp2/3 complex recruitment. This process culminates in clathrin-mediated endocytosis for N-WASP, but not WASP, where the function appears to be in coupling the actin cytoskeleton to substrate-induced membrane deformations that guide cell movement. This is not the first example of cells repurposing the curvature sensitivity of the endocytic machinery to help engage with their substrate. In particular, collagen fibers induce persistent non-endocytic clathrin-coated structures that aid in 3D migration in other cellular contexts (Elkhatib et al., 2017). We propose WASP is performing a similar function in highly motile neutrophils.

WASP and N-WASP have also been implicated in building podosomes and invadopodia (Isaac et al., 2010; Nusblat et al., 2011; Mizutani et al., 2002; Yamaguchi et al., 2005; Yu et al., 2012; Yu and Machesky, 2012), which are membrane exvaginations that participate in extracellular matrix degradation and mechanosensation (Albiges-Rizo et al., 2009; Murphy and Courtneidge, 2011). The WASP puncta we observe are triggered by membrane invagination, rather than exvagination, and wrap around the substrate, instead of poking into it. Therefore, WASP structures in neutrophils are distinct from invadopodia and podosomes and may represent a variation on how cells interact with their substrate. Also, rather than degrading ECM, neutrophils squeeze through pores in collagen matrices, which may rely on an alternate mode of substrate engagement (Lämmermann et al., 2013; Steadman et al., 1997; Allport et al., 2002; Lämmermann et al., 2008).

WASP is unusual in that it is able to integrate both cell polarity and membrane curvature for its recruitment; only membrane deformations in the cell front result in WASP enrichment (**Fig. 4A-D, Fig. S5C-D**). How does WASP sense cell polarity? An obvious candidate is Cdc42; it is one of the primary inputs to WASP-mediated actin assembly (Rohatgi et al., 1999; Higgs and Pollard, 2000), and Cdc42 activity is polarized towards the leading edge of migrating neutrophils (Yang et al., 2016). However, we find Cdc42 to be dispensable for WASP polarity (**Fig. 4E-F**). WASP can also bind Rac with a lower affinity (Kolluri et al., 1996), but structure-function analysis of WASP reveals that the Cdc42- and Rac-interactive binding domain of WASP is also dispensable for its polarity (**Fig. S5E**). Importantly, there are other inputs that activate WASP family proteins; N-

WASP-mediated actin polymerization can be elicited in the absence of Cdc42 both *in vitro* (Takano et al., 2008) and by pathogens (Moreau et al., 2000). Therefore, future studies will be needed to elucidate the additional inputs to WASP's polarity sensing. Similarly, the molecular basis of WASP's curvature sensitivity remains unknown. Previous studies have suggested that the BAR domain-containing protein FBP17 plays a role in the curvature sensitivity of N-WASP (Lou et al., 2019; Tsujita et al., 2015), but we find that WASP can sense curvature in the absence of FBP17 in neutrophils (**Fig. S3**). Whether this is due to a difference between WASP and N-WASP or whether the use of dominant-negative FBP17 in initial studies inhibited other N-WASP-associating curvature-sensitive proteins, which can normally co-oligomerize and compensate for one another (Chan Wah Hak et al., 2018; Tsujita et al., 2013), is unknown.

Overall, our work establishes WASP as a link between cell movement and substrate topology. Previous reports have found that different cell types, including HL-60s, can sense nanopatterned topologies and respond to them through reorientation and aligned migration (Driscoll et al., 2014; Sun et al., 2015). In the case of adherent cells, this is thought to be through imposing spatial constraints on focal adhesion formation and maturation (Ray et al., 2017). However, for loosely adherent cells like neutrophils and *Dictyostelium discoideum* that do not rely on long-lived adhesive structures (Lämmermann and Sixt, 2009; Driscoll et al., 2014), the molecular mechanism unpinning physical environment sensing and alignment to substrate topologies has remained unclear. Some proposed mechanisms for cytoskeletal remodeling in response to membrane deformation include membrane geometry sensing (Itoh et al., 2005; Zhao

et al., 2017; Lou et al., 2019; Takenawa and Suetsugu, 2007), membrane tension sensing (Houk et al., 2012; Tsujita et al., 2015; Diz-Muñoz et al., 2016), force adaptation (Bieling et al., 2016; Mueller et al., 2017), and even actin filament bending (Risca et al., 2012). The fact that WASP is both curvature-sensitive and essential for HL-60 alignment to nanoridges supports WASP-mediated actin polymerization as a mechanism by which loosely adherent cells can sense and align with their substrate's topology.

Membrane curvature has emerged as a key regulator for WASP family proteins; other NPFs from this family such as N-WASP and WAVE also preferentially enrich to sites of membrane curvature (Lou et al., 2019; Pipathsouk et al., 2019). Unique curvature preferences among WASP family NPFs could help differentiate their organization and inform the morphology of the actin networks they generate. For N-WASP, enrichment to membrane invaginations could facilitate scission of endocytic vesicles from the plasma membrane (Kaksonen et al., 2005; Akamatsu et al., 2020). For WAVE, saddle preference could help organize a coherently advancing flat lamellipod (Pipathsouk et al., 2019). And for WASP, enrichment to stable inward curvature (in particular the saddle-shaped necks of invaginations) could help the cell integrate substrate topologies with motility. Interestingly, these proteins also appear to have different rules for reading curvature—for instance WASP is much better than WAVE at persistently enriching to saddles at bead-induced membrane invaginations (**Fig. 2F-G**). Whether these individualized responses arise from subtle differences in saddle-curvature preference, WAVE complex's extinction at non-motile barriers (Weiner et al., 2007), or WASP's

broader permissive zone (**Fig. 1A**) will be an interesting avenue for future investigation. Notably, in some contexts WASP can even substitute for WAVE (Veltman et al., 2012; Zhu et al., 2016; Tang et al., 2013), suggesting overlap in the membrane geometries they can read. Future studies systematically investigating the curvature preferences among WASP family NPFs will expand our understanding of how variation in membrane geometry can feed into the diversification of actin network patterning.

MATERIALS AND METHODS

Cell Culture

HL-60 cells are from the lab of Henry Bourne. PLB-985 cells were originally obtained

from Onyx Pharmaceuticals. RNA-seq was recently performed on both of these

backgrounds (Rincón et al., 2018), confirming cell line identity and supporting a

previous report that PLB-985 cells are actually a sub-line of HL-60 cells (Drexler et al.,

2003). Both lines were grown in RPMI 1640 media supplemented with L-glutamine and

25 mM HEPES (Corning, MT10041CV) and containing 10% (v/v) heat-inactivated fetal

bovine serum (Gibco, 16140071) and 1X penicillin-streptomycin (Gibco, 15140148)

(called HL-60 media). Cultures were split to 0.17-0.2 million cells/mL every two to three

days and grown at 37°C/5% CO_2. Cells were differentiated for experiments by diluting

cells to 0.2 million/mL, adding 1.5% (v/v) DMSO (Santa Cruz Biotechnology, 358801),

and incubating for 4-5 days. HEK293T cells (used to generate lentivirus for transduction

of HL-60s) were grown in DMEM (Gibco, 11995065) containing 10% (v/v) heat-

inactivated fetal bovine serum (Gibco, 16140071) and 1X penicillin-streptomycin (Gibco,

15140148) and maintained at 37°C/5% CO_2. Cells were routinely checked for

mycoplasma contamination.

Plasmids

A vector for mammalian expression of TagRFP-T-Arp3 was generated by PCR

amplification of the Arp3 coding sequence and Gibson assembly into a lentiviral pHR

backbone containing a N-terminal TagRFP-T sequence. The sequence for

mNeonGreen2$_{1-10}$ (Feng et al., 2017) was similarly transferred to a pHR backbone.

Hem1-eGFP, used for measuring WAVE complex recruitment, was previously described (Diz-Muñoz et al., 2016; Pipathsouk et al., 2019) and similarly generated by transferring the protein coding sequence to a pHR backbone.

For generating knockout lines, guide RNAs with homology to exon 1 of *WAS* (5′ CCAATGGGAGGAAGGCCCGG 3′ and 5' GCTGAACCGCTGGTGCTCCT 3') and exon 4 of *FNBP1* (5′ ACGAAATGAATGATTACGCA 3′) were selected using the CRISPR design tool in Benchling (www.benchling.com) and cloned into the previously described LentiGuide-Puro vector (Addgene plasmid #52963) (Sanjana et al., 2014). The vector used to express human-codon–optimized *Streptococcus pyrogenes* Cas9-BFP was also previously described (Graziano et al., 2017).

For endogenous tagging of WASP with plasmid donor, 500 base pairs of the 5' untranslated region and the start codon (5' homology arm), TagRFP-T flanked by unique seven amino acid long linkers, and the 500 base pairs following the start codon (3' homology arm) were Gibson assembled into a minimal backbone (pUC19). A similar approach was used for endogenous tagging of clathrin light chain A (*CLTA*).

Transduction of HL-60 cells

HEK293T cells (ATCC) were seeded into 6-well plates and grown until approximately 70% confluent. For each well, 1.5 µg pHR vector (containing the appropriate transgene), 0.167 µg vesicular stomatitis virus-G vector, and 1.2 µg cytomegalovirus 8.91 vector were mixed and prepared for transfection using TransIT-293 Transfection Reagent

(Mirus Bio, MIR 2705). Following transfection, cells were incubated for 3 days, after which virus-containing supernatants were harvested and concentrated approximately 40-fold using Lenti-X Concentrator (Takara Bio, 631232) per the manufacturer's instructions. Concentrated viruses were frozen and stored at −80°C until needed or used immediately. For all transductions, virus was mixed with 0.36 million cells in growth media supplemented with 8 µg/mL Polybrene (Sigma-Aldrich, H9268) and incubated overnight. Fluorescence-activated cell sorting (FACS) (BD Biosciences, FACSAria2 or FACSAria3) was used to isolated cells with the desired expression level of the transgene.

Generation of CRISPR knockout HL-60 cell lines

WASP and FBP17 HL-60 knockout cell lines were generated as described in (Graziano et al., 2019). Briefly, HL-60s were transduced with a puromycin-selectable vector containing an sgRNA sequence for the gene of interest. Following puromycin selection, cells were transduced with a *S. pyrogenes* Cas9 sequence fused to tagBFP. Cells expressing high levels of Cas9-tagBFP were isolated with FACS. Cells were then diluted into 96-well plates at a density of approximately one cell per well in 50% (v/v) filtered conditioned media from a healthy culture, 40% (v/v) fresh HL-60 media, and 10% (v/v) additional heat-inactivated fetal bovine serum. Clonal cell lines were expanded and validated using amplicon sequencing and immunoblot. Two clonal lines were generated for WASP from separate CRISPR assemblies (guide 1: 5' CCAATGGGAGGAAGGCCCGG 3' and guide 2: 5' GCTGAACCGCTGGTGCTCCT 3') and one clonal line was generated for FBP17 (5' ACGAAATGAATGATTACGCA 3').

The Cdc42 PLB-895 knockout line was generated as described in (Bell et al., 2021). Briefly, PLB-895 cells were electroporated with a CRISPR-Cas9 ribonucleoprotein (RNP) complex. Tandem guides targeting exon 4 of Cdc42 were purchased from Synthego (5' TTTCTTTTTTCTAGGGCAAG 3' and 5' ATTTGAAAACGTGAAAGAAA 3'). Guides were complexed with Cas9 protein and electroporated into cells using a custom suspended-drop electroporation device (Guignet and Meyer, 2008).

Immunoblot assays

Protein content from one million cells was extracted using TCA precipitation. Samples were separated via SDS-PAGE and transferred to a nitrocellulose membrane. Membranes were blocked for approximately one hour in either a 1:1 solution of TBS (20 mM Tris, 500 mM NaCl [pH 7.4]) and Odyssey Blocking Buffer (LI-COR, 927-70001) or PBS with 1% BSA. For detection of WASP, the membrane was incubated overnight at 4°C in primary antibody (Cell Signaling Technology, 4860) diluted 1:1,000 in a 1:1 solution of TBST (TBS + 0.2% w/v Tween 20) and Odyssey Blocking Buffer. For detection of FBP17, the membrane was incubated for one hour at room temperature in primary antibody (a gift from P. De Camilli, Yale University) diluted 1:5,000 in PBST with 1% BSA. Membranes were washed three times with either TBST or PBST and then incubated for 45 minutes at room temperature with LI-COR secondary antibodies diluted 1:20,000 in either Odyssey Blocking Buffer or PBS with 1% BSA. Membranes were then washed three times with TBST or PBST, washed a final time with TBS or PBS, and imaged using an Odyssey Fc (LI-COR).

GAPDH (Invitrogen, MA5-15738) was used as a loading control for each blot and subjected to the same conditions as the antibody detecting the protein of interest.

Generation of CRISPR knock-in HL-60 cell lines

Wild type HL-60 cells were transduced with a plasmid containing the non-fluorescent 1-10 segment of mNeonGreen2 ($mNG2_{1-10}$) (Feng et al., 2017). Cells expressing the transgene were identified through electroporation (Lonza, 4D-Nucleofector) with a mCherry-conjugated $mNeonGreen2_{11}$ ($mNG2_{11}$) mRNA. Positive cells (those that were fluorescent in both 488 and 561) were identified using FACS (Sony, SH800) and a subset of cells that appeared to have a single insertion of $mNG2_{1-10}$ was isolated. After a few days the mRNA was degraded and the cells lost fluorescence. This created the base $mNG2_{1-10}$ HL-60 cell line used with $mNG2_{11}$ knock-in.

sgRNAs of the target gene were obtained by *in vitro* transcription as described in (Leonetti et al., 2016) with modifications only to the PCR polymerase used (Phusion; New England Biolabs, M0530S). A 100 µL reaction of $mNG2_{1-10}$ HL-60 cells were electroporated (Invitrogen, Neon) with a Cas9-sgRNA complex and a single-stranded DNA ultramer (ssDNA) (Integrated DNA Technologies) donor containing $mNG2_{11}$, a linker, and ~55 base pairs of homology to each side of the cut site. Cas9-sgRNA complex formation and electroporation protocols were adapted from (Brunetti et al., 2018; Garner et al., 2020). Briefly, 90 pmol of Cas9 containing a nuclear localization signal (QB3 MacroLab) and 270 pmol of sgRNA were mixed on ice and then incubated

at room temperature for 30 minutes. Meanwhile, 2 million cells were spun down at 300xg for 5 minutes and washed with phosphate buffered saline to remove extracellular proteins. When the Cas9 complex was ready, cells were again spun down and this time resuspended in 100 µL room temperature R Buffer (Invitrogen, MPK10096). 100 pmol of ssDNA donor was added to the Cas9-sgRNA complex and the whole mixture was added to the resuspended cells. Samples were then electroporated at 1350V for 35 ms and recovered in 5 mL warmed media. Cells were monitored and allowed to recover. Using 100 µL tips led to recovery within only a few days. Cells were then expanded for selection with FACS. The percent of fluorescent cells ranged from 0.1-1%. For WAS, which has only one allele, the polyclonal line resulting from FACS sorting was sequence-verified and used for experiments. For other knock-ins, cells underwent clonal dilution as outlined above and surviving clones were screened using a PCR-based gel shift assay. Samples showing biallelic insertion were gel extracted and Sanger sequenced.

In the case of full-length fluorophore knock-in, plasmid donor was used in place of ssDNA donor. The above protocol was executed with only slight changes. First, 10 µL tips were used in place of 100 µL tips to remove the need for large amounts of donor. RNP components and the number of cells electroporated were therefore scaled down by a factor of ten as originally done in (Brunetti et al., 2018; Garner et al., 2020). Next, 800 ng of plasmid donor was provided in place of the ssDNA donor. Finally, post electroporation cells were rescued in 500 µL pre-warmed media in a 24 well plate and allowed to recover for ten to fourteen days. Despite lowered viability and longer

recovery times post electroporation compared to 100 µL tips, similar tagging efficiencies were observed with this strategy.

N-terminal tagging was performed for WASP (*WAS*), clathrin LCa (*CLTA*), and FBP17 (*FNBP1*). We used the following guide sequences to target near the start codon: *WAS* – 5' GGCAGAAAGCACCATGAGTG 3', *CLTA* – 5' GAACGGATCCAGCTCAGCCA 3', 5' *FNBP1* – CGTCCCCTGCACCATGAGCT 3'.

Compression of HL-60s for imaging

For all experiments excepting the STED, collagen, nanopatterns, and EDTA treatment, HL-60s were confined based on the method described in (Bell et al., 2018). For this work, a solution of 2% low-melt agarose (Gold Biotechnology, A-204) was made in L-15 media (Gibco, 21083-027) and microwaved in a loosely capped conical placed in a water reservoir. Heating was done in short increments to promote melting while preventing the solution from boiling over. Once completely melted, the gel was kept at 37°C to allow cooling while preventing solidification. Meanwhile, 500 µL of differentiated HL-60 cells were spun down at 200 x g for 5 minutes and then concentrated three-fold in HL-60 media. 5 µL of the concentrated cells were placed in the center of a circular well (Greiner Bio-One, 655891) and allowed to settle. When circular-welled plates could not be used, a 5 mm circular mold was inserted into the well. After the agarose had cooled to 37°C, 195 µL of agarose was slowly pipetted into the bottom edge of the well, allowing the agarose to spread over the droplet of cells. The pipette was then slowly raised up the side of the well to continue depositing agarose without sweeping away the

covered cells. The plate was then allowed to dry uncovered for 20-45 minutes in an oven set to 37°C without humidity to promote high compression of the cells as in (Garner et al., 2020). Adequate flattening of the lamellipod was determined by observation of the complete cell footprint in TIRF.

Compression was also used in STED experiments, but modifications were used to accommodate imaging chambers (Ibidi, 80827). Briefly, a 1% solution of liquid agarose (Thermo Scientific, 17850) was made and poured into 8X8X5 mm square molds. After solidification, agarose pads were stored in L-15 media (Gibco, 21083-027) at 4°C. Cells were compressed by gently placing a room temperature agarose pad atop the well with tweezers and putting the chamber lid on top of the pad. Flattening was confirmed by cellular morphology in the confocal imaging mode.

The EDTA experiments required inelastic confinement to maintain the polarity and migration of cells. To achieve this, we confined cells between two glass surfaces as descried in (Malawista et al., 2000; Graziano et al., 2017). Briefly, glass slides and coverslips were thoroughly cleaned with Sparkleen laboratory detergent (Fisherbrand, 04-320-4) and then sonicated for 10 minutes first in acetone, then twice in ethanol, and finally three times in MilliQ water. The glass was immediately dried using N_2 gas and stored in a clean, dry place. For experiments, differentiated HL-60s were concentrated to 20 million cells/mL in HL-60 media and a final concentration of 10 mM EDTA (Teknova, E0306) was added to "+EDTA" samples. 2 µL of cells were then placed onto a clean slide and a clean 18x18 mm coverslip was dropped on top. We confirmed that

the cell solution was wicked across the majority of the coverslip surface, ensuring adequate confinement. Chambers were then sealed with VALAP (a mixture of equal parts Vaseline, paraffin wax, and lanolin) (Cold Spring Harbor Laboratory, 2015) and imaged.

Cell compression onto beads

Agarose-based compression was done as described above with the addition of red (580/605) fluorescent carboxylate-modified microspheres (Invitrogen, F8887) to concentrated cells prior to plating. For quantitation of WASP and Arp2/3 recruitment to beads, a low density of beads was used (1:10,000 to 1:100,000). For bead carpets, as shown in Fig. 4A, beads were diluted only 1:1000. Since bead density is proportional to the bead volume a less stringent dilution was used for 500 nm beads (1:100).

STED microscopy of cells on beads

All STED microscopy experiments were performed in plain glass 8-well chambers (Ibidi, 80827). Wells were coated with 100 µL of 20 µg/mL porcine fibronectin (prepared from whole blood) diluted in PBS at 37°C for 30 min and washed 3x using L-15 media (Gibco, 21083-027). Next, any residual imaging media was removed and 100 µL of beads diluted in L-15 were added to the well. We used either red-fluorescent (580/605) carboxylate modified beads of 200 or 500 nm diameter (Invitrogen, F8887) or non-fluorescent carboxylate modified beads of 500 nm diameter (Invitrogen, C37481). Bead density and adhesion were checked on the microscope prior to the addition of cells. Next, 800 µL of differentiated HL-60 cells were spun down at 200 x g for 5 minutes and

resuspended in 100 μL of 5x concentrated CellMask Deep Red (Invitrogen, C10046) in L-15. Immediately after resuspension in the labeling solution, cells were spun down again at 200 x g for 5 minutes. After complete removal of supernatant, cells were resuspended in 100 μL of L-15 media and added to the well containing beads. To promote cell adhesion, the sample was placed in a 37°C incubator for 15 min. Finally, an agarose pad was placed atop cells for confinement and samples were imaged at room temperature.

Cell migration on nanopatterned substrates

Nanopatterned and flat control substrates were purchased in 96-well plate format from Curi Bio (ANFS-0096). Wells were coated with 50 μL of 10 μg/mL porcine fibronectin (prepared from whole blood) dissolved in PBS for one hour at room temperature. The fibronectin solution was then removed and replaced with differentiated HL-60s (wild type or WASP KO) diluted by a factor of five into fresh HL-60 media containing one drop of the nuclear dye NucBlue (R37605, Thermo Fisher) per 500 μL. The plate was then transferred to a 37°C/5% CO_2 incubator for 15 minutes to allow cells to adhere. The media was then gently pipetted over cells a few times to remove unattached cells and the media was exchanged for 100 μL fresh HL-60 media without NucBlue. The plate was then transferred to the microscope, which had been pre-heated to 37°C and an environmental chamber supplying 5% CO_2 was turned on. The plate was allowed to equilibrate for one hour prior to imaging, giving cells time to align on nanopatterns. Wild type and WASP KO cells were always plated in adjacent wells, so that three positions

could be taken per well over the time interval between frames (45s). Acquisition lasted one hour, and both bright field and 405 (nuclei) were collected.

Cell migration in fluorescent collagen matrices

30 µL of pH-adjusted FITC-conjugated bovine skin collagen at 1 mg/mL (Sigma-Aldrich, C4361) was polymerized in a round, glass-bottomed well (Greiner Bio-One, 655891) for 3 minutes at room temperature and then gently washed with PBS (Elkhatib et al., 2017). 100 µL of differentiated HL-60s in HL-60 media were immediately added and allowed to migrate into the network up to one hour before imaging. WASP co-localization with fibers was assessed using a cell line that had WASP endogenously tagged with TagRFP-T.

Microscopy

Total internal reflection fluorescence (TIRF) imaging experiments in Fig. 1 (excepting F), Fig. 2, and Fig. 4 (excepting E) were performed at room temperature using the ring TIRF light path of a DeltaVision OMX SR microscope (GE Healthcare) with a 60x/1.42 numerical aperture (NA) oil Plan Apo objective (Olympus) and 1.518 refractive index oil (Cargille). The system is equipped with 405, 445, 488, 514, 568, and 642 nm laser lines. mNeonGreen2 and eGFP-tagged proteins were imaged with the 488 nm laser line and Tag-RFP-T-tagged proteins were measured with the 568 nm laser line. The system was controlled with OMX AquireSR software (GE) and alignment of two channel images was performed with SoftWoRx (GE).

TIRF and confocal imaging experiments in Fig. 1F, Fig. 4E, Fig. 5 (excepting G), and Fig. 6 were performed at 37°C on a Nikon Eclipse Ti inverted microscope equipped with a motorized laser TIRF illumination unit, a Borealis beam conditioning unit (Andor), a CSU-W1 Yokugawa spinning disk (Andor), a 60X PlanApo TIRF 1.49 numerical aperture (NA) objective (Nikon), an iXon Ultra EMCCD camera (Andor), and a laser module (Vortran Laser Technology) equipped with 405, 488, 561, and 642 nm laser lines. NucBlue was measured with the 405 nm line, mNeonGreen2-tagged proteins were measured with the 488 nm line, and TagRFP-T-tagged proteins were measured with the 561 nm line. The system was controlled with μManager software (version 2.0-beta) (Edelstein et al., 2010).

Confocal microscopy and stimulated emission-depletion (STED) microscopy for Fig. 3 and panel 5G were performed at room temperature using an Abberior Expert Line system (Abberior Instruments GmbH) with an inverted Olympus IX83 microscope, QUADScan Beam Scanner (Abberior Instruments GmbH) and an Olympus UPlanSApo x100/1.41 oil immersion objective lens. The system was controlled with ImSpector (Abberior). Confocal measurements of mNeonGreen2 were made using a 488 nm line. All STED measurements were made using a 640 nm line and a 775 nm STED depletion laser. Sequential imaging was used to avoid cross-excitation. 2D STED imaging of the CellMask Deep Red and SiR-actin were performed using a 30 nm pixel size for X and Y. 3D STED imaging of CellMask Deep Red was performed in XZY mode using a z piezo stage (P-736 Pinano, Physik Instrumente), the Abberior adaptive illumination module RESCue, and a 30 nm voxel size for X, Y and Z (Staudt et al., 2011). The STED and confocal channels were aligned using measurements of 100 nm fluorescent beads on

the Abberior auto-alignment sample. Spatial resolution of 3D STED was determined by imaging 40 nm far-red fluorescent beads purchased from Abberior.

Image Analysis

Images were displayed in FIJI and WASP puncta and nuclei tracking were performed using the plug-in TrackMate (Tinevez et al., 2017). Tracks were filtered for desired property (duration, quality, etc.) within TrackMate and coordinates were exported as csv files and analyzed with custom Python code that made heavy use of the scikit-image package (van der Walt et al., 2014). All analysis code and a csv of all data are available at https://github.com/rachel-bot/WASP. Kymographs were created using the plug-in KymographBuilder (Mary et al., 2016).

Quantification of WASP distribution

A single image from the indicated number of cells over three experiments was rotated using an interactive rigid transformation in FIJI so that cells were consistently oriented from left to right. Otsu thresholding was used to create a binary cell mask. The cell was then split into four regions: the leading edge, cell front, cell rear, and uropod. The leading edge was defined as the area removed by erosion of the front 40% of the cell mask with a 20x20 structuring element, which was determined to robustly isolate signal at the leading edge. The cell front was defined as the front 50% of the cell excluding the leading edge. The cell rear was defined as the region behind the front 50% of the cell and before the rear 20% of the cell, which was defined as the uropod. WASP signal in each region was determined by applying an Otsu threshold to a Difference of Gaussians

131

(DoG) image (σ_{high} = 2, σ_{low} = 1), which highlights puncta. The signal in each region was measured by summing the binary of the thresholded DoG image. These values were then normalized to the total number of pixels in the cell mask for each region. Conversely, calculating the normalized integrated intensity in each region, after applying an Otsu threshold to remove background signal, yielded similar results.

Spatial histogram analysis

Using cells oriented from left to right as explained above, a cell mask and its contour were created. The left, right, top and bottom bounds of the cell outline were extracted. The width of the cell in x was divided into the specified number of bins, here ten. Next, a DoG image of WASP or clathrin or Arp3 was generated and an Otsu threshold was applied. The user confirmed that this scheme of puncta identification was sufficiently robust. The resulting binary image was indexed and puncta centroids were recorded. The x-coordinate of each puncta was then used to assign it to one of the bins made from the cell mask's x coordinate range. Similar analysis was repeated over all cells. Puncta counts per bin (each with different x-coordinates but representing the same portion of the cell, i.e. the front $1/10^{th}$) from all cells were then combined and normalized to the total puncta counts to get a density. For display purposes, this 1D array was extended in y to be 2D and multiplied by a binary mask of a well-polarized cell. All values outside of the cell body were converted to NaN to give a white background, and the cell contour was plotted on top to denote this boundary.

Similar analysis was employed to investigate the disappearance of WASP puncta in +/- EDTA conditions and the appearance of WASP puncta in wild type and Cdc42 knockout cells. To do this, puncta tracks were determined in FIJI using TrackMate (Tinevez et al., 2017), discarding traces that did not disappear during the course of the movie, for the EDTA experiments, or traces that were present at the start of the movie, for the Cdc42 experiment. All tracks were manually checked to ensure they accurately captured the last or first frame of the puncta, respectively. Centroids at these times points were then passed to the analysis described above and their position relative to the cell length was determined by manual specification of the cell front and cell back in each frame using the matplotlib (Hunter, 2007) command "ginput" to select these landmarks.

Quantification of WASP and Arp3 signal at beads

Single frames from movies of cells migrating over beads were selected based on the presence of beads under the lamellipod. The matplotlib (Hunter, 2007) command "ginput" was used to manually select beads that were completely under the lamellipod. The immediate region around the bead was isolated and a 2D Gaussian was fit to the diffraction-limited WASP or Arp3 signal. Intensity of the signal at the bead was calculated using the formula for volume under a Gaussian: $2\pi A\sigma_x\sigma_y$, where the amplitude (A) and the standard deviation in each direction (σ_x, σ_y) come from the fit. This quantity is independent of background signal. For comparing WASP intensity across bead sizes, Gaussian volumes were normalized to bead surface area in accordance with our observation from STED microscopy that WASP signal is distributed across the entire invagination surface at sufficiently high curvatures ($\leq$ 1/200 nm). For

133

assessing Arp3 recruitment to beads in wild type and WASP KO cells, Gaussian volumes were not directly compared since many beads failed to induce Arp3 puncta in the absence of WASP and therefore could not be fit. Instead, we reported the fraction of beads able to form Arp3 puncta for each cell background. To avoid losing the intensity data entirely, we took an orthogonal approach and calculated a background subtracted integrated intensity for Arp3 signal at beads. To do this, Arp3 signal was tracked over time, and the frame with the brightest Arp3 signal in the region of the bead of interest was isolated. Arp3 signal was then masked with the bead signal to separate out the foreground and background. The mean background signal was calculated and subtracted from each pixel in the masked image. The resulting values were then summed to get the background subtracted Arp3 integrated intensity.

Measuring WASP signal as a function of distance from the leading edge

Movies where a cell moved the majority of its length over a bead without dislodging it from the TIRF plane were analyzed. At each time point, the cell rear and cell front were manually selected with the matplotlib (Hunter, 2007) command "ginput" to find the cell's major axis. Beads that passed under the cell were selected and, at each time point, their (stationary) position was projected onto the major axis. This value was normalized to the major axis length in each frame to get a relative distance from the cell front (value of 0 to 1). For each time point, WASP intensity was estimated by summing the signal in a small box around the bead. The exactness of this measurement is not imperative since all traces are normalized to their maximum WASP signal to build a profile of relative signal as a function of distance from the cell front.

To get a population level profile, relative distances were discretized to the nearest 0.1 and traces from many beads were averaged to create a line plot. To better represent the data underlying this line, WASP data points in each positional bin were overlaid onto the plot and colored by the kernel density estimate of the value compared to all WASP values in the same positional bin.

Co-localization by correlation analysis

Co-localization of curvature sensors with beads and WASP with clathrin/Arp3/FBP17 were determined by calculating the Pearson correlation coefficient between the flattened vectors of each channel. For statistical comparison of enrichment between curvature sensors, distributions of correlation coefficients were compared using an unpaired two-tailed t-test. For statistical comparison of co-localization between markers in the same cell, a negative control was generated by rotating one channel 90 degrees to remove co-localization while maintaining any punctate organization in the image (Dunn et al., 2011). The Pearson correlation coefficient was again calculated. The values of non-transformed and transformed correlation coefficients were combined across cells and experiments to create distributions. The means from each technical replicate were then compared between these two conditions using a paired t-test.

Cell tracking and measurement of migration properties

Cell nuclei were tracked in FIJI using TrackMate (Tinevez et al., 2017) and resulting csv files were exported for analysis in Python.

To prevent double counting of cells, only traces that lasted at least half of the movie were kept. Then, to make sure all cells were compared over the same time window, only cells present for the first half of the movie were analyzed. Total distance traveled by each cell was calculated by applying the distance formula to each time point and summing the resulting displacements. This was performed for either both x and y or x or y independently, depending on the kind of distance being reported.

Mean squared displacement (MSD) was calculated using

$$\frac{1}{N}\sum_{i=1}^{N}\left|x^{(i)}(t)-x^{(i)}(0)\right|^2$$

where $x^{(i)}(t)$ is the position of i-th cell at time t and $x^{(i)}(0)$ is its initial position. N denotes the total number of cells.

The persistence ratio for each cell was calculated using

$$\frac{|x(T)-x(0)|}{\sum_{t=0}^{T}|x(t)-x(0)|}$$

where T denotes the time point being compared with t = 0 (Gorelik and Gautreau, 2014). . The persistence ratio traces were then averaged across cells.

Statistics and reproducibility

All experiments were repeated a minimum of three times unless otherwise specified. For comparisons between datasets in Fig. 2E, Fig. 4, Fig. 5, and Fig. 6 the mean of each technical replicate is plotted as a large, colored marker over the single cell

distribution. When there were many observations per cell, statistics were done on single cell means. Otherwise, statistics were done on replicate means. Alternatively, in the case of small n, such as Fig. 2G and Fig. 3D, statistics were applied to all measurements. We used a paired t-test when datasets were related (i.e. localization of clathrin and WASP in the same cells (Fig. 1E) or WASP signal at single beads before and after membrane closing (Fig. 3F)) or if there was obvious technical variability (Fig. 4F). We also used paired t-tests to compare migration properties as suggested in (Lord et al., 2020) to reduce influence from day-to-day variability. For measurements that do not exhibit major experimental variation (such as the position of WASP puncta appearance (Fig. 4F)), we used an unpaired t-test. Paired and unpaired two-tailed t-tests are standard for comparing means between parametric datasets.

Data and code availability

All analysis code and a csv of all data are available at https://github.com/rachel-bot/WASP.

SUPPLEMENTAL MATERIAL

Fig. S1 schematizes the knock-in strategy used and reports the propensity of HL-60 cells to undergo non-homologous end joining and homology directed repair. It also includes sequencing validation of the endogenously tagged WASP and clathrin light chain A cell lines as well as Western blot and sequencing validation of WASP KO cell lines. Fig. S2 shows that endogenous WASP enriches to the interface between HL-60 cells and collagen fibers. Fig. S3 examines the relationship between WASP and FBP17. Fig. S4 demonstrates the resolution increase provided by 3D STED and offers an orthogonal measure of WASP enrichment as a function of bead diameter. Fig. S5 further investigates how polarity informs WASP recruitment. Video 1 shows the dynamics of endogenous WASP in a persistently migrating HL-60 cell. Video 2 shows the spatial separation of endogenous WASP and endogenous clathrin light chain A in an HL-60 cell. Video 3 shows the effect of blocking integrin-based adhesion on WASP puncta dynamics. Video 4 shows the dynamics of WASP recruitment to sites of bead-induced plasma membrane deformation. Video 5 shows plasma membrane and WASP rearrangement as an HL-60 cell migrates over beads. Video 6 shows similar migration between wild type and WASP-null HL-60 cells on flat substrates while Video 7 shows severe defects in WASP-null HL-60 cells plated on nanoridged substrates.

ACKNOWLEDGEMENTS

REFERENCES

Akamatsu, M., R. Vasan, D. Serwas, M.A. Ferrin, P. Rangamani, and D.G. Drubin. 2020. Principles of self-organization and load adaptation by the actin cytoskeleton during clathrin-mediated endocytosis. *Elife*. 9:e49840. doi:10.7554/eLife.49840.

Albiges-Rizo, C., O. Destaing, B. Fourcade, E. Planus, and M.R. Block. 2009. Actin machinery and mechanosensitivity in invadopodia, podosomes and focal adhesions. *J. Cell Sci.* 122:3037–3049. doi:10.1242/jcs.052704.

Aldrich, R.A., A.G. Steinberg, and D.D. Campbell. 1954. Pedigree demonstrating a sex-linked recessive condition characterized by draining ears, eczematoid dermatitis and bloody diarrhea. *Pediatrics*. 13:133–139.

Allport, J.R., Y.C. Lim, J. Michael Shipley, R.M. Senior, S.D. Shapiro, N. Matsuyoshi, D. Vestweber, and F.W. Luscinskas. 2002. Neutrophils from MMP-9- or neutrophil elastase-deficient mice show no defect in transendothelial migration under flow in vitro. *J. Leukoc. Biol.* 71:821–828. doi:10.1189/jlb.71.5.821.

Banjade, S., and M.K. Rosen. 2014. Phase transitions of multivalent proteins can promote clustering of membrane receptors. *Elife*. 3:e04123. doi:10.7554/eLife.04123.

Bear, J.E., J.F. Rawls, and C.L. Saxe. 1998. SCAR, a WASP-related protein, isolated as a suppressor of receptor defects in late Dictyostelium development. *J. Cell Biol.* 142:1325–1335. doi:10.1083/jcb.142.5.1325.

Bell, G.R.R., D.E. Natwick, and S.R. Collins. 2018. Parallel High-Resolution Imaging of Leukocyte Chemotaxis Under Agarose with Rho-Family GTPase Biosensors. *In*

Rho GTPases. Methods in Molecular Biology, vol 1821. F. Rivero, editor. Humana Press, New York. 71–85.

Bell, G.R.R., E. Rincón, E. Akdoğan, and S.R. Collins. 2021. Optogenetic control of receptors reveals distinct roles for actin- and Cdc42-dependent negative signals in chemotactic signal processing. *bioRxiv*. doi:10.1101/2021.04.03.438340 (Preprint posted April 4, 2021).

Benesch, S., S. Lommel, A. Steffen, T.E.B. Stradal, N. Scaplehorn, M. Way, J. Wehland, and K. Rottner. 2002. Phosphatidylinositol 4,5-biphosphate (PIP2)-induced vesicle movement depends on N-WASP and involves Nck, WIP, and Grb2. *J. Biol. Chem.* 277:37771–37776. doi:10.1074/jbc.M204145200.

Benesch, S., S. Polo, F.P. Lai, K.I. Anderson, T.E.B. Stradal, J. Wehland, and K. Rottner. 2005. N-WASP deficiency impairs EGF internalization and actin assembly at clathrin-coated pits. *J. Cell Sci.* 118:3103–3115. doi:10.1242/jcs.02444.

Bhatia, V.K., K.L. Madsen, P.Y. Bolinger, A. Kunding, P. Hedegard, U. Gether, and D. Stamou. 2009. Amphipathic motifs in BAR domains are essential for membrane curvature sensing. *EMBO J.* 28:3303–3314. doi:10.1038/emboj.2009.261.

Bieling, P., T. De Li, J. Weichsel, R. McGorty, P. Jreij, B. Huang, D.A. Fletcher, and R.D. Mullins. 2016. Force feedback controls motor activity and mechanical properties of self-assembling branched actin networks. *Cell*. 164:115–127. doi:10.1016/j.cell.2015.11.057.

Blanchoin, L., R. Boujemaa-Paterski, C. Sykes, and J. Plastino. 2014. Actin dynamics, architecture, and mechanics in cell motility. *Physiol. Rev.* 94:235–263. doi:10.1152/physrev.00018.2013.

Brunetti, L., M.C. Gundry, A. Kitano, D. Nakada, and M.A. Goodell. 2018. Highly

    Efficient Gene Disruption of Murine and Human Hematopoietic Progenitor Cells by

    CRISPR/Cas9. *J. Vis. Exp.* e57278. doi:10.3791/57278.

Case, L.B., X. Zhang, J.A. Ditlev, and M.K. Rosen. 2019. Stoichiometry controls activity

    of phase-separated clusters of actin signaling proteins. *Science*. 363:1093–1097.

    doi:10.1126/science.aau6313.

Chan Wah Hak, L., S. Khan, I. Di Meglio, A. Law, S. Lucken-Ardjomande Häsler, L.M.

    Quintaneiro, A.P.A. Ferreira, M. Krause, H.T. McMahon, and E. Boucrot. 2018.

    FBP17 and CIP4 recruit SHIP2 and lamellipodin to prime the plasma membrane for

    fast endophilin-mediated endocytosis. *Nat. Cell Biol.* 20:1023–1031.

    doi:10.1038/s41556-018-0146-8.

Clement, K., H. Rees, M.C. Canver, J.M. Gehrke, R. Farouni, J.Y. Hsu, M.A. Cole, D.R.

    Liu, J.K. Joung, D.E. Bauer, and L. Pinello. 2019. CRISPResso2 provides accurate

    and rapid genome editing sequence analysis. *Nat. Biotechnol.* 37:224–226.

    doi:10.1038/s41587-019-0032-3.

Cold Spring Harbor Laboratory. 2015. Recipe: Valap sealant. *Cold Spring Harb. Protoc.*

    pdb.rec082917. doi:10.1101/pdb.rec082917.

Cougoule, C., E. Van Goethem, V. Le Cabec, F. Lafouresse, L. Dupré, V. Mehraj, J.L.

    Mège, C. Lastrucci, and I. Maridonneau-Parini. 2012. Blood leukocytes and

    macrophages of various phenotypes have distinct abilities to form podosomes and

    to migrate in 3D environments. *Eur. J. Cell Biol.* 91:938–949.

    doi:10.1016/j.ejcb.2012.07.002.

Davis, B.H., R.J. Walter, C.B. Pearson, E.L. Becker, and J.M. Oliver. 1982. Membrane activity and topography of F-Met-Leu-Phe-treated polymorphonuclear leukocytes. Acute and sustained responses to chemotactic peptide. *Am. J. Pathol.* 108:206–216.

Derry, J.M.J., H.D. Ochs, and U. Francke. 1994. Isolation of a novel gene mutated in Wiskott-Aldrich syndrome. *Cell*. 78:635–644. doi:10.1016/0092-8674(94)90528-2.

Diz-Muñoz, A., K. Thurley, S. Chintamen, S.J. Altschuler, L.F. Wu, D.A. Fletcher, and O.D. Weiner. 2016. Membrane Tension Acts Through PLD2 and mTORC2 to Limit Actin Network Assembly During Neutrophil Migration. *PLOS Biol.* 14:e1002474. doi:10.1371/journal.pbio.1002474.

Doyon, J.B., B. Zeitler, J. Cheng, A.T. Cheng, J.M. Cherone, Y. Santiago, A.H. Lee, T.D. Vo, Y. Doyon, J.C. Miller, D.E. Paschon, L. Zhang, E.J. Rebar, P.D. Gregory, F.D. Urnov, and D.G. Drubin. 2011. Rapid and efficient clathrin-mediated endocytosis revealed in genome-edited mammalian cells. *Nat. Cell Biol.* 13:331–337. doi:10.1038/ncb2175.

Drexler, H.G., W.G. Dirks, Y. Matsuo, and R.A.F. MacLeod. 2003. False leukemia-lymphoma cell lines: An update on over 500 cell lines. *Leukemia*. 17:416–426. doi:10.1038/sj.leu.2402799.

Driscoll, M.K., X. Sun, C. Guven, J.T. Fourkas, and W. Losert. 2014. Cellular contact guidance through dynamic sensing of nanotopography. *ACS Nano*. 8:3546–3555. doi:10.1021/nn406637c.

Duleh, S.N., and M.D. Welch. 2010. WASH and the Arp2/3 complex regulate endosome shape and trafficking. *Cytoskeleton*. 67:193–206. doi:10.1002/cm.20437.

Dunn, K.W., M.M. Kamocka, and J.H. McDonald. 2011. A practical guide to evaluating colocalization in biological microscopy. *Am. J. Physiol. Physiol.* 300:C723–C742. doi:10.1152/ajpcell.00462.2010.

Edelstein, A., N. Amodaj, K. Hoover, R. Vale, and N. Stuurman. 2010. Computer control of microscopes using μManager. *Curr. Protoc. Mol. Biol.* 1–17. doi:10.1002/0471142727.mb1420s92.

Elkhatib, N., E. Bresteau, F. Baschieri, A.L. Rioja, G. van Niel, S. Vassilopoulos, and G. Montagnac. 2017. Tubular clathrin/AP-2 lattices pinch collagen fibers to support 3D cell migration. *Science*. 356:eaal4713. doi:10.1126/science.aal4713.

Feng, S., S. Sekine, V. Pessino, H. Li, M.D. Leonetti, and B. Huang. 2017. Improved split fluorescent proteins for endogenous protein labeling. *Nat. Commun.* 8:370. doi:10.1038/s41467-017-00494-8.

Fritz-Laylin, L.K., S.J. Lord, and R.D. Mullins. 2017. WASP and SCAR are evolutionarily conserved in actin-filled pseudopod-based motility. *J. Cell Biol.* 216:1673–1688. doi:10.1083/jcb.201701074.

Garner, R.M., G. Skariah, A. Hadjitheodorou, N.M. Belliveau, A. Savinov, M.J. Footer, and J.A. Theriot. 2020. Neutrophil-like HL-60 cells expressing only GFP-tagged β-actin exhibit nearly normal motility. *Cytoskeleton*. 77:181–196. doi:10.1002/cm.21603.

Gorelik, R., and A. Gautreau. 2014. Quantitative and unbiased analysis of directional persistence in cell migration. *Nat. Protoc.* 9:1931–1943. doi:10.1038/nprot.2014.131.

Graziano, B.R., D. Gong, K.E. Anderson, A. Pipathsouk, A.R. Goldberg, and O.D. Weiner. 2017. A module for Rac temporal signal integration revealed with optogenetics. *J. Cell Biol.* 216:2515–2531. doi:10.1083/jcb.201604113.

Graziano, B.R., J.P. Town, E. Sitarska, T.L. Nagy, M. Fošnarič, S. Penič, A. Iglič, V. Kralj-Iglič, N.S. Gov, A. Diz-Muñoz, and O.D. Weiner. 2019. Cell confinement reveals a branched-actin independent circuit for neutrophil polarity. *PLOS Biol.* 17:e3000457. doi:10.1371/journal.pbio.3000457.

Guignet, E.G., and T. Meyer. 2008. Suspended-drop electroporation for high-throughput delivery of biomolecules into cells. *Nat. Methods*. 5:393–395. doi:10.1038/nmeth.1201.

Higgs, H.N., and T.D. Pollard. 2000. Activation by Cdc42 and PIP2 of Wiskott-Aldrich Syndrome protein (WASp) stimulates actin nucleation by Arp2/3 complex. *J. Cell Biol.* 150:1311–1320. doi:10.1083/jcb.150.6.1311.

Houk, A.R., A. Jilkine, C.O. Mejean, R. Boltyanskiy, E.R. Dufresne, S.B. Angenent, S.J. Altschuler, L.F. Wu, and O.D. Weiner. 2012. Membrane tension maintains cell polarity by confining signals to the leading edge during neutrophil migration. *Cell*. 148:175–188. doi:10.1016/j.cell.2011.10.050.

Hunter, J.D. 2007. Matplotlib: A 2D Graphics Environment. *Comput. Sci. Eng.* 9:90–95. doi:10.1109/MCSE.2007.55.

Isaac, B.M., D. Ishihara, L.M. Nusblat, J.C. Gevrey, A. Dovas, J. Condeelis, and D. Cox. 2010. N-WASP has the ability to compensate for the loss of WASP in macrophage podosome formation and chemotaxis. *Exp. Cell Res.* 316:3406–3416. doi:10.1016/j.yexcr.2010.06.011.

Itoh, T., K.S. Erdmann, A. Roux, B. Habermann, H. Werner, and P. De Camilli. 2005. Dynamin and the actin cytoskeleton cooperatively regulate plasma membrane invagination by BAR and F-BAR proteins. *Dev. Cell*. 9:791–804. doi:10.1016/j.devcel.2005.11.005.

Iversen, L., S. Mathiasen, J.B. Larsen, and D. Stamou. 2015. Membrane curvature bends the laws of physics and chemistry. *Nat. Chem. Biol.* 11:822–825. doi:10.1038/nchembio.1941.

Jain, N., and T. Thanabalu. 2015. Molecular difference between WASP and N-WASP critical for chemotaxis of T-cells towards SDF-1α. *Sci. Rep.* 5:15031. doi:10.1038/srep15031.

Jones, R.A., Y. Feng, A.J. Worth, A.J. Thrasher, S.O. Burns, and P. Martin. 2013. Modelling of human Wiskott-Aldrich syndrome protein mutants in zebrafish larvae using in vivo live imaging. *J. Cell Sci.* 126:4077–4084. doi:10.1242/jcs.128728.

Kaksonen, M., C.P. Toret, and D.G. Drubin. 2005. A modular design for the clathrin- and actin-mediated endocytosis machinery. *Cell*. 123:305–320. doi:10.1016/j.cell.2005.09.024.

Kaplan, C., S.J. Kenny, S. Chen, E. Sitarska, K. Xu, and D.G. Drubin. 2020. Adaptive actin organization counteracts elevated membrane tension to ensure robust endocytosis. *bioRxiv*. doi:10.1101/2020.04.05.026559 (Preprint posted April 6, 2020).

Kessels, M.M., and B. Qualmann. 2002. Syndapins integrate N-WASP in receptor-mediated endocytosis. *EMBO J.* 21:6083–94. doi:10.1093/emboj/cdf604.

Keszei, M., J. Record, J.S. Kritikou, H. Wurzer, C. Geyer, M. Thiemann, P. Drescher, H. Brauner, L. Köcher, J. James, M. He, M.A.P. Baptista, C.I.M. Dahlberg, A. Biswas, S. Lain, D.P. Lane, W. Song, K. Pütsep, P. Vandenberghe, S.B. Snapper, and L.S. Westerberg. 2018. Constitutive activation of WASp in X-linked neutropenia renders neutrophils hyperactive. *J. Clin. Invest.* 128:4115–4131. doi:10.1172/JCI64772.

Kolluri, R., K.F. Tolias, C.L. Carpenter, F.S. Rosen, and T. Kirchhausen. 1996. Direct interaction of the Wiskott-Aldrich syndrome protein with GTPase Cdc42. *Proc. Natl. Acad. Sci. U. S. A.* 93:5615–5618. doi:10.1073/pnas.93.11.5615.

Kumar, S., J. Xu, C. Perkins, F. Guo, S. Snapper, F.D. Finkelman, Y. Zheng, and M.D. Filippi. 2012. Cdc42 regulates neutrophil migration via crosstalk between WASp, CD11b, and microtubules. *Blood*. 120:3563–3574. doi:10.1182/blood-2012-04-426981.

Kunda, P., G. Craig, V. Dominguez, and B. Baum. 2003. Abi, Sra1, and Kette control the stability and localization of SCAR/WAVE to regulate the formation of actin-based protrusions. *Curr. Biol.* 13:1867–1875. doi:10.1016/j.cub.2003.10.005.

Lämmermann, T., P. V. Afonso, B.R. Angermann, J.M. Wang, W. Kastenmüller, C.A. Parent, and R.N. Germain. 2013. Neutrophil swarms require LTB4 and integrins at sites of cell death in vivo. *Nature*. 498:371–375. doi:10.1038/nature12175.

Lämmermann, T., B.L. Bader, S.J. Monkley, T. Worbs, R. Wedlich-Söldner, K. Hirsch, M. Keller, R. Förster, D.R. Critchley, R. Fässler, and M. Sixt. 2008. Rapid leukocyte migration by integrin-independent flowing and squeezing. *Nature*. 453:51–55. doi:10.1038/nature06887.

Lämmermann, T., and M. Sixt. 2009. Mechanical modes of "amoeboid" cell migration. *Curr. Opin. Cell Biol.* 21:636–644. doi:10.1016/j.ceb.2009.05.003.

Larsen, J.B., K.R. Rosholm, C. Kennard, S.L. Pedersen, H.K. Munch, V. Tkach, J.J. Sakon, T. Bjørnholm, K.R. Weninger, P.M. Bendix, K.J. Jensen, N.S. Hatzakis, M.J. Uline, and D. Stamou. 2020. How membrane geometry regulates protein sorting independently of mean curvature. *ACS Cent. Sci.* 6:1159–1168. doi:10.1021/acscentsci.0c00419.

Leithner, A., A. Eichner, J. Müller, A. Reversat, M. Brown, J. Schwarz, J. Merrin, D.J.J. de Gorter, F. Schur, J. Bayerl, I. de Vries, S. Wieser, R. Hauschild, F.P.L. Lai, M. Moser, D. Kerjaschki, K. Rottner, J.V. Small, T.E.B. Stradal, and M. Sixt. 2016. Diversified actin protrusions promote environmental exploration but are dispensable for locomotion of leukocytes. *Nat. Cell Biol.* 18:1253–1259. doi:10.1038/ncb3426.

Leonetti, M.D., S. Sekine, D. Kamiyama, J.S. Weissman, and B. Huang. 2016. A scalable strategy for high-throughput GFP tagging of endogenous human proteins. *Proc. Natl. Acad. Sci. U. S. A.* 113:E3501–E3508. doi:10.1073/pnas.1606731113.

Li, P., S. Banjade, H.-C. Cheng, S. Kim, B. Chen, L. Guo, M. Llaguno, J. V. Hollingsworth, D.S. King, S.F. Banani, P.S. Russo, Q.-X. Jiang, B.T. Nixon, and M.K. Rosen. 2012. Phase transitions in the assembly of multivalent signalling proteins. *Nature*. 483:336–340. doi:10.1038/nature10879.

Li, X., L. Matino, W. Zhang, L. Klausen, A.F. McGuire, C. Lubrano, W. Zhao, F. Santoro, and B. Cui. 2019. A nanostructure platform for live-cell manipulation of membrane curvature. *Nat. Protoc.* 14:1772–1802. doi:10.1038/s41596-019-0161-7.

Liu, C., X. Bai, J. Wu, S. Sharma, A. Upadhyaya, C.I.M. Dahlberg, L.S. Westerberg, S.B. Snapper, X. Zhao, and W. Song. 2013. N-WASP Is essential for the negative regulation of B cell receptor signaling. *PLoS Biol.* 11:e1001704. doi:10.1371/journal.pbio.1001704.

Lord, S.J., K.B. Velle, R.D. Mullins, and L.K. Fritz-Laylin. 2020. SuperPlots: Communicating reproducibility and variability in cell biology. *J. Cell Biol.* 219:e202001064. doi:10.1083/jcb.202001064.

Lou, H., W. Zhao, X. Li, L. Duan, A. Powers, M. Akamatsu, F. Santoro, A.F. McGuire, Y. Cui, D.G. Drubin, and B. Cui. 2019. Membrane curvature underlies actin reorganization in response to nanoscale surface topography. *Proc. Natl. Acad. Sci.* 116:23143–23151. doi:10.1073/pnas.1910166116.

Malawista, S.E., A. de Boisfleury Chevance, and L.A. Boxer. 2000. Random locomotion and chemotaxis of human blood polymorphonuclear leukocytes from a patient with Leukocyte Adhesion Deficiency-1: Normal displacement in close quarters via chimneying. *Cell Motil. Cytoskeleton*. 46:183–189. doi:10.1002/1097-0169(200007)46:3<183::AID-CM3>3.0.CO;2-2.

Manor, U., S. Bartholomew, G. Golani, E. Christenson, M. Kozlov, H. Higgs, J. Spudich, and J. Lippincott-Schwartz. 2015. A mitochondria-anchored isoform of the actin-nucleating spire protein regulates mitochondrial division. *Elife*. 4:e08828. doi:10.7554/eLife.08828.

Mary, H., C. Rueden, and T. Ferreira. 2016. KymographBuilder: Release 1.2.4. doi:10.5281/zenodo.56702.

Merrifield, C.J., B. Qualmann, M.M. Kessels, and W. Almers. 2004. Neural Wiskott

    Aldrich Syndrome Protein (N-WASP) and the Arp 2/3 complex are recruited to sites

    of clathrin-mediated endocytosis in cultured fibroblasts. *Eur. J. Cell Biol.* 83:13–18.

    doi:10.1078/0171-9335-00356.

Miki, H., T. Sasaki, Y. Takai, and T. Takenawa. 1998. Induction of filopodium formation

    by a WASP-related actin-depolymerizing protein N-WASP. *Nature*. 391:93–96.

    doi:10.1038/34208.

Misra, A., R.P.Z. Lim, Z. Wu, and T. Thanabalu. 2007. N-WASP plays a critical role in

    fibroblast adhesion and spreading. *Biochem. Biophys. Res. Commun.* 364:908–

    912. doi:10.1016/j.bbrc.2007.10.086.

Mizutani, K., H. Miki, T. Takenawa, H. Maruta, T. Takenawa, H. He, and H. Maruta.

    2002. Essential role of neural Wiskott-Aldrich syndrome protein in podosome

    formation and degradation of extracellular matrix in src-transformed fibroblasts.

    Cancer Res. 62:669–674.

Moreau, V., F. Frischknecht, I. Reckmann, R. Vincentelli, G. Rabut, D. Stewart, and M.

    Way. 2000. A complex of N-WASP and WIP integrates signalling cascades that

    lead to actin polymerization. *Nat. Cell Biol.* 2:441–448. doi:10.1038/35017080.

Mueller, J., G. Szep, M. Nemethova, I. de Vries, A.D. Lieber, C. Winkler, K. Kruse, J.V.

    Small, C. Schmeiser, K. Keren, R. Hauschild, and M. Sixt. 2017. Load adaptation of

    lamellipodial actin networks. *Cell*. 171:188–200.e16. doi:10.1016/j.cell.2017.07.051.

Mund, M., J.A. van der Beek, J. Deschamps, S. Dmitrieff, P. Hoess, J.L. Monster, A.

    Picco, F. Nédélec, M. Kaksonen, and J. Ries. 2018. Systematic nanoscale analysis

of endocytosis links efficient vesicle formation to patterned actin nucleation. *Cell*. 174:884–896.e17. doi:10.1016/j.cell.2018.06.032.

Murphy, D.A., and S.A. Courtneidge. 2011. The "ins" and "outs" of podosomes and invadopodia: Characteristics, formation and function. *Nat. Rev. Mol. Cell Biol.* 12:413–426. doi:10.1038/nrm3141.

Nakagawa, H., H. Miki, M. Ito, K. Ohashi, T. Takenawa, and S. Miyamoto. 2001. N-WASP, WAVE and Mena play different roles in the organization of actin cytoskeleton in lamellipodia. *J. Cell Sci.* 114:1555–1565.

De Noronha, S., S. Hardy, J. Sinclair, M.P. Blundell, J. Strid, O. Schulz, J. Zwirner, G.E. Jones, D.R. Katz, C. Kinnon, and A.J. Thrasher. 2005. Impaired dendritic-cell homing in vivo in the absence of Wiskott-Aldrich syndrome protein. *Blood*. 105:1590–1597. doi:10.1182/blood-2004-06-2332.

Nusblat, L.M., A. Dovas, and D. Cox. 2011. The non-redundant role of N-WASP in podosome-mediated matrix degradation in macrophages. *Eur. J. Cell Biol.* 90:205–212. doi:10.1016/j.ejcb.2010.07.012.

Ochs, H.D., S.J. Slichter, L.A. Harker, W.E. Von Behrens, R.A. Clark, and R.J. Wedgwood. 1980. The Wiskott-Aldrich syndrome: Studies of lymphocytes, granulocytes, and platelets. *Blood*. 55:243–252. doi:10.1182/blood.v55.2.243.243.

Pipathsouk, A., R.M. Brunetti, J.P. Town, A. Breuer, P.A. Pellett, K. Marchuk, N.T. Tran, M.F. Krummel, and D. Stamou. 2019. WAVE complex self-organization templates lamellipodial formation. *bioRxiv*. doi:10.1101/836585 (Preprint posted November 9, 2019).

Pollitt, A.Y., and R.H. Insall. 2009. WASP and SCAR/WAVE proteins: the drivers of

    actin assembly. *J. Cell Sci.* 122:2575–2578. doi:10.1242/jcs.023879.

Ray, A., O. Lee, Z. Win, R.M. Edwards, P.W. Alford, D.-H. Kim, and P.P. Provenzano.

    2017. Anisotropic forces from spatially constrained focal adhesions mediate contact

    guidance directed cell migration. *Nat. Commun.* 8:14923.

    doi:10.1038/ncomms14923.

Rincón, E., B.L. Rocha-Gregg, and S.R. Collins. 2018. A map of gene expression in

    neutrophil-like cell lines. *BMC Genomics*. 19:573. doi:10.1186/s12864-018-4957-6.

Risca, V.I., E.B. Wang, O. Chaudhuri, J.J. Chia, P.L. Geissler, and D.A. Fletcher. 2012.

    Actin filament curvature biases branching direction. *Proc. Natl. Acad. Sci. U. S. A.*

    109:2913–2918. doi:10.1073/pnas.1114292109.

Rogers, S.L., U. Wiedemann, N. Stuurman, and R.D. Vale. 2003. Molecular

    requirements for actin-based lamella formation in Drosophila S2 cells. *J. Cell Biol.*

    162:1079–1088. doi:10.1083/jcb.200303023.

Rohatgi, R., L. Ma, H. Miki, M. Lopez, T. Kirchhausen, T. Takenawa, and M.W.

    Kirschner. 1999. The Interaction between N-WASP and the Arp2/3 Complex Links

    Cdc42-Dependent Signals to Actin Assembly. *Cell*. 97:221–231.

    doi:10.1016/S0092-8674(00)80732-1.

Rottner, K., J. Faix, S. Bogdan, S. Linder, and E. Kerkhoff. 2017. Actin assembly

    mechanisms at a glance. *J. Cell Sci.* 130:3427–3435. doi:10.1242/jcs.206433.

Sagot, I., S.K. Klee, and D. Pellman. 2002. Yeast formins regulate cell polarity by

    controlling the assembly of actin cables. *Nat. Cell Biol.* 4:42–50.

    doi:10.1038/ncb719.

Sanjana, N.E., O. Shalem, and F. Zhang. 2014. Improved vectors and genome-wide libraries for CRISPR screening. *Nat. Methods*. 11:783–784. doi:10.1038/nmeth.3047.

Snapper, S.B., P. Meelu, D. Nguyen, B.M. Stockton, P. Bozza, F.W. Alt, F.S. Rosen, U.H. von Andrian, and C. Klein. 2005. WASP deficiency leads to global defects of directed leukocyte migration in vitro and in vivo. *J. Leukoc. Biol.* 77:993–998. doi:10.1189/jlb.0804444.

Staudt, T., A. Engler, E. Rittweger, B. Harke, J. Engelhardt, and S.W. Hell. 2011. Far-field optical nanoscopy with reduced number of state transition cycles. *Opt. Express*. 19:5644–5657. doi:10.1364/OE.19.005644.

Steadman, R., P.L.S. John, R.A. Evans, G.J. Thomas, M. Davies, L.W. Heck, and D.R. Abrahamson. 1997. Human neutrophils do not degrade major basement membrane components during chemotactic migration. *Int. J. Biochem. Cell Biol.* 29:993–1004. doi:10.1016/S1357-2725(97)00038-1.

Subramanian, B.C., K. Moissoglu, and C.A. Parent. 2018. The LTB4-BLT1 axis regulates the polarized trafficking of chemoattractant GPCRs during neutrophil chemotaxis. *J. Cell Sci.* jcs.217422. doi:10.1242/jcs.217422.

Sun, X., M.K. Driscoll, C. Guven, S. Das, C.A. Parent, J.T. Fourkas, and W. Losert. 2015. Asymmetric nanotopography biases cytoskeletal dynamics and promotes unidirectional cell guidance. *Proc. Natl. Acad. Sci.* 112:12557–12562. doi:10.1073/pnas.1502970112.

Takano, K., K. Takano, K. Toyooka, and S. Suetsugu. 2008. EFC/F-BAR proteins and

    the N-WASP-WIP complex induce membrane curvature-dependent actin

    polymerization. *EMBO J.* 27:2817–28. doi:10.1038/emboj.2008.216.

Takenawa, T., and S. Suetsugu. 2007. The WASP–WAVE protein network: connecting

    the membrane to the cytoskeleton. *Nat. Rev. Mol. Cell Biol.* 8:37–48.

    doi:10.1038/nrm2069.

Tang, H., A. Li, J. Bi, D.M. Veltman, T. Zech, H.J. Spence, X. Yu, P. Timpson, R.H.

    Insall, M.C. Frame, and L.M. MacHesky. 2013. Loss of scar/WAVE complex

    promotes N-WASP- and FAK-dependent invasion. *Curr. Biol.* 23:107–117.

    doi:10.1016/j.cub.2012.11.059.

Taunton, J., B.A. Rowning, M.L. Coughlin, M. Wu, R.T. Moon, T.J. Mitchison, and C.A.

    Larabell. 2000. Actin-dependent propulsion of endosomes and lysosomes by

    recruitment of N-WASP. *J. Cell Biol.* 148:519–530. doi:10.1083/jcb.148.3.519.

Taylor, M.J., D. Perrais, and C.J. Merrifield. 2011. A high precision survey of the

    molecular dynamics of mammalian clathrin-mediated endocytosis. *PLoS Biol.*

    9:e1000604. doi:10.1371/journal.pbio.1000604.

Tinevez, J.Y., N. Perry, J. Schindelin, G.M. Hoopes, G.D. Reynolds, E. Laplantine, S.Y.

    Bednarek, S.L. Shorte, and K.W. Eliceiri. 2017. TrackMate: An open and extensible

    platform for single-particle tracking. *Methods*. 115:80–90.

    doi:10.1016/j.ymeth.2016.09.016.

Tsujita, K., A. Kondo, S. Kurisu, J. Hasegawa, T. Itoh, and T. Takenawa. 2013.

    Antagonistic regulation of F-BAR protein assemblies controls actin polymerization

    during podosome formation. *J. Cell Sci.* 126:2267–78. doi:10.1242/jcs.122515.

Tsujita, K., S. Suetsugu, N. Sasaki, M. Furutani, T. Oikawa, and T. Takenawa. 2006. Coordination between the actin cytoskeleton and membrane deformation by a novel membrane tubulation domain of PCH proteins is involved in endocytosis. *J. Cell Biol.* 172:269–279. doi:10.1083/jcb.200508091.

Tsujita, K., T. Takenawa, and T. Itoh. 2015. Feedback regulation between plasma membrane tension and membrane-bending proteins organizes cell polarity during leading edge formation. *Nat. Cell Biol.* 17:749–758. doi:10.1038/ncb3162.

Veltman, D.M., J.S. King, L.M. Machesky, and R.H. Insall. 2012. SCAR knockouts in Dictyostelium: WASP assumes SCAR's position and upstream regulators in pseudopods. *J. Cell Biol.* 198:501–508. doi:10.1083/jcb.201205058.

van der Walt, S., J.L. Schönberger, J. Nunez-Iglesias, F. Boulogne, J.D. Warner, N. Yager, E. Gouillart, and T. Yu. 2014. scikit-image: image processing in Python. *PeerJ*. 2:e453. doi:10.7717/peerj.453.

Weiner, O.D., W.A. Marganski, L.F. Wu, S.J. Altschuler, and M.W. Kirschner. 2007. An actin-based wave generator organizes cell motility. *PLoS Biol.* 5:e221. doi:10.1371/journal.pbio.0050221.

Westerberg, L., M. Larsson, S.J. Hardy, C. Fernández, A.J. Thrasher, and E. Severinson. 2005. Wiskott-Aldrich syndrome protein deficiency leads to reduced B-cell adhesion, migration, and homing, and a delayed humoral immune response. *Blood*. 105:1144–1152. doi:10.1182/blood-2004-03-1003.

Wiskott, A. 1937. Familiarer, angeborener morbus werlhofli? (Familial congenital Werlhof's disease?). *Monatsschr Kinderheikd.* 68:212–216.

Yamaguchi, H., M. Lorenz, S. Kempiak, C. Sarmiento, S. Coniglio, M. Symons, J. Segall, R. Eddy, H. Miki, T. Takenawa, and J. Condeelis. 2005. Molecular mechanisms of invadopodium formation: The role of the N-WASP-Arp2/3 complex pathway and cofilin. *J. Cell Biol.* 168:441–452. doi:10.1083/jcb.200407076.

Yang, C., L. Czech, S. Gerboth, S. Kojima, G. Scita, and T. Svitkina. 2007. Novel Roles of Formin mDia2 in Lamellipodia and Filopodia Formation in Motile Cells. *PLoS Biol.* 5:e317. doi:10.1371/journal.pbio.0050317.

Yang, H.W., S.R. Collins, and T. Meyer. 2016. Locally excitable Cdc42 signals steer cells during chemotaxis. *Nat. Cell Biol.* 18:191–201. doi:10.1038/ncb3292.

Yu, X., and L.M. Machesky. 2012. Cells assemble invadopodia-like structures and invade into matrigel in a matrix metalloprotease dependent manner in the circular invasion assay. *PLoS One*. 7:e30605. doi:10.1371/journal.pone.0030605.

Yu, X., T. Zech, L. McDonald, E.G. Gonzalez, A. Li, I. Macpherson, J.P. Schwarz, H. Spence, K. Futó, P. Timpson, C. Nixon, Y. Ma, I.M. Anton, B. Visegrády, R.H. Insall, K. Oien, K. Blyth, J.C. Norman, and L.M. Machesky. 2012. N-WASP coordinates the delivery and F-actin-mediated capture of MT1-MMP at invasive pseudopods. *J. Cell Biol.* 199:527–544. doi:10.1083/jcb.201203025.

Yuruker, B., and V. Niggli. 1992. α-Actinin and vinculin in human neutrophils: Reorganization during adhesion and relation to the actin network. *J. Cell Sci.* 101:403–414.

Zhang, H., U.Y. Schaff, C.E. Green, H. Chen, M.R. Sarantos, Y. Hu, D. Wara, S.I. Simon, and C.A. Lowell. 2006. Impaired integrin-dependent function in Wiskott-

Aldrich syndrome protein-deficient murine and human neutrophils. *Immunity*. 25:285–295. doi:10.1016/j.immuni.2006.06.014.

Zhang, K., and J.F. Chen. 2012. The regulation of integrin function by divalent cations. *Cell Adhes. Migr.* 6:20–29. doi:10.4161/cam.18702.

Zhao, W., L. Hanson, H.-Y. Lou, M. Akamatsu, P.D. Chowdary, F. Santoro, J.R. Marks, A. Grassart, D.G. Drubin, Y. Cui, and B. Cui. 2017. Nanoscale manipulation of membrane curvature for probing endocytosis in live cells. *Nat. Nanotechnol.* 12:750–756. doi:10.1038/nnano.2017.98.

Zhu, Z., Y. Chai, Y. Jiang, W. Li, H. Hu, W. Li, J.W. Wu, Z.X. Wang, S. Huang, and G. Ou. 2016. Functional coordination of WAVE and WASP in C. elegans neuroblast migration. *Dev. Cell*. 39:224–238. doi:10.1016/j.devcel.2016.09.029.

Zicha, D., W.E. Allen, P.M. Brickell, C. Kinnon, G.A. Dunn, G.E. Jones, and A.J. Thrasher. 1998. Chemotaxis of macrophages is abolished in the Wiskott-Aldrich syndrome. *Br. J. Haematol.* 101:659–665. doi:10.1046/j.1365-2141.1998.00767.x.

Zuchero, J.B., A.S. Coutts, M.E. Quinlan, N.B. La Thangue, and R.D. Mullins. 2009. p53-cofactor JMY is a multifunctional actin nucleation factor. *Nat. Cell Biol.* 11:451–459. doi:10.1038/ncb1852.
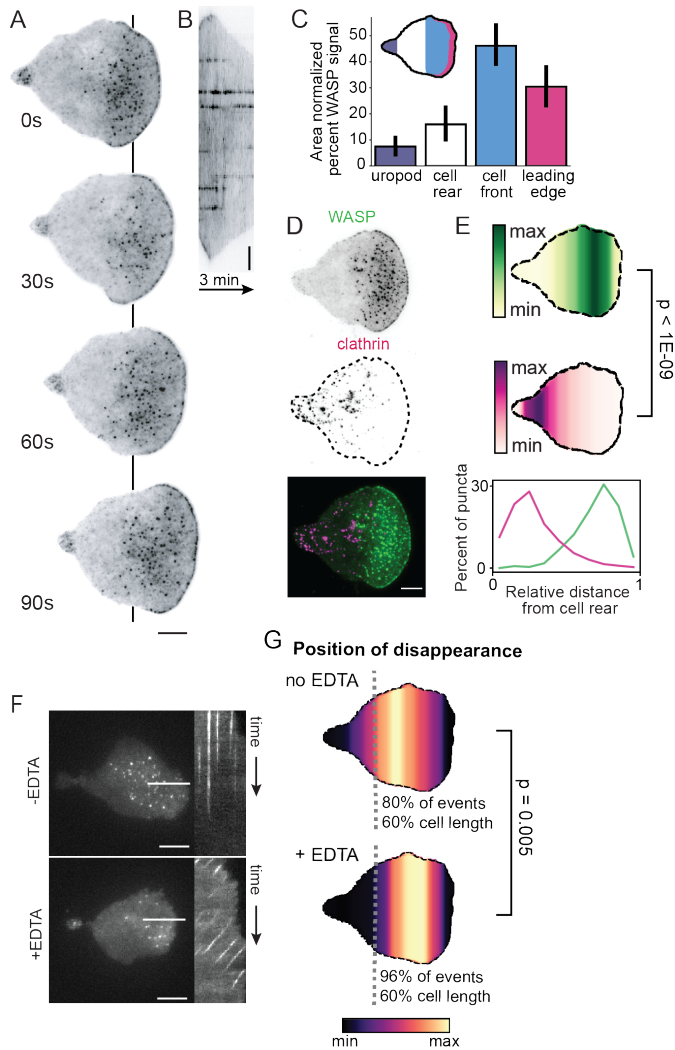
Figure 3.1

Figure 3.1 Endogenous WASP forms puncta stabilized by cell-substrate interactions.

(A) TIRF microscopy of endogenous WASP reveals localization to the tip of the lamellipod and to ventral puncta throughout the front half of the cell and to a lesser extent the uropod. Color map is inverted. Each frame is 30s. See also Video 1.

(B) Kymograph along the line in (A) highlights the stationary nature of WASP puncta relative to the substrate. Scale bar is 2 μm.

(C) WASP shows primary localization to punctate structures biased toward the cell front. n = 22 cells collected across three experiments. Leading edge: 30.5 ± 4.4%, cell front: 46.1 ± 4.4%, cell rear: 16.0 ± 3.6%, uropod: 7.5 ± 2.2% of total WASP signal. Values are area normalized.

(D) Endogenous WASP and endogenous clathrin light chain A fail to co-localize. Color map is inverted for single channel images. See also Video 2.

(E) Spatial distribution of WASP (green) and clathrin (magenta) puncta and their corresponding line scans confirm consistent spatial separation of these proteins in co-expressing cells. n = 11 cells collected across three experiments with more than 1000 puncta measured for each marker. Mean relative position of WASP is 0.71 ± 0.01 and mean relative position of clathrin is 0.29 ± 0.02 on the single cell level. p= 8.82E-10 by a paired two- tailed t-test on the mean puncta position of each marker in each cell.

(F) Treatment of cells with EDTA, a calcium and magnesium chelator that blocks integrin-based adhesion, causes normally stationary WASP puncta to experience retrograde flow relative to the substrate. Left depicts a single frame of endogenous WASP with a line used to construct the kymograph to the right. See also Video 3.

(G) Spatial distribution of the position of disappearance of WASP puncta reveals earlier extinction in the presence of EDTA. n = 12 cells per condition collected across three experiments with approximately 300 puncta measured for each condition. Mean relative position of puncta disappearance is 0.55 ± 0.03 in the absence of EDTA and 0.66 ± 0.02 in the presence of EDTA on the single cell level. p = 0.005 by an unpaired two-tailed t-test on the mean position of puncta disappearance for each cell. For relative positions, the cell rear is defined as 0 and the cell front is defined as 1. Scale bars are 5 µm unless otherwise specified.
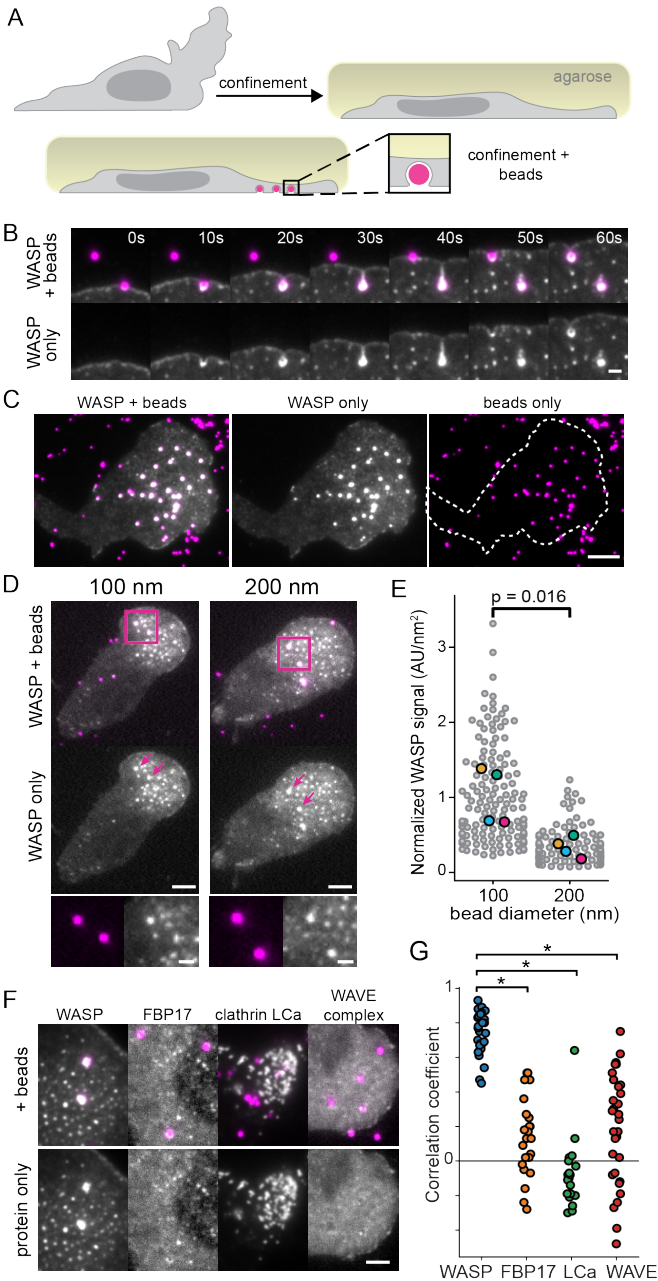
Figure 3.2

Figure 3.2 WASP is recruited to membrane invaginations in a curvature-dependent manner

(A) Experimental strategy of confining cells onto beads to induce sites of substrate-controlled plasma membrane curvature.

160

(B) Time lapse imaging reveals rapid recruitment of endogenous WASP to 500 nm bead-induced invaginations. Scale bar is 1 μm.

(C) WASP consistently localizes to 200 nm bead-induced invaginations across the cell front. Scale bar is 5 μm. See also Video 4.

(D) WASP knock-in cells were confined onto beads of varying diameter to assess the curvature sensitivity of WASP recruitment. Images are scaled to the same intensity for WASP. Below is a zoomed inset of the boxed regions. Scale bars are 5 μm and 1 μm for the inset.

(E) Quantification of WASP signal at 100 and 200 nm beads reveals significantly more WASP at smaller invaginations (sites of higher curvature) when normalized to bead surface area. Mean WASP signal per unit area is 1.01 ± 0.19 AU/nm^2 for 100 nm beads and 0.34 ± 0.07 AU/nm^2 for 200 nm beads on the replicate level. Large markers denote the mean of each replicate, which were compared using an unpaired two-tailed t-test: p = 0.016. Measurements are from 142 100 nm beads and 120 200 nm beads collected across four experiments.

(F) WASP enrichment to 500 nm beads is much stronger than that of other known curvature-sensitive proteins: FBP17, clathrin light chain A (LCa), and WAVE complex. Scale bar is 2 μm.

(G) Pearson correlation coefficients for 1.5X1.5 μm ROIs of a bead and the protein of interest. WASP has a significantly higher correlation with bead signal ($r = 0.75 \pm 0.02$) compared to FBP17 (0.14 ± 0.05), clathrin LCa (-0.09 ± 0.04), and WAVE complex (0.19 ± 0.06). The correlation of each protein with beads was compared to the correlation of WASP with beads using an unpaired two-tailed t-test. Asterisks mark significance. $p_{WASP/FBP17} = 6.56E\text{-}18$, $p_{WASP/clathrin} = 4.60E\text{-}24$, and $p_{WASP/WAVE} = 5.58E\text{-}13$. $n_{WASP} = 31$, $n_{FBP17} = 24$, $n_{clathrin} = 21$, and $n_{WAVE} = 31$ beads each from one experiment.
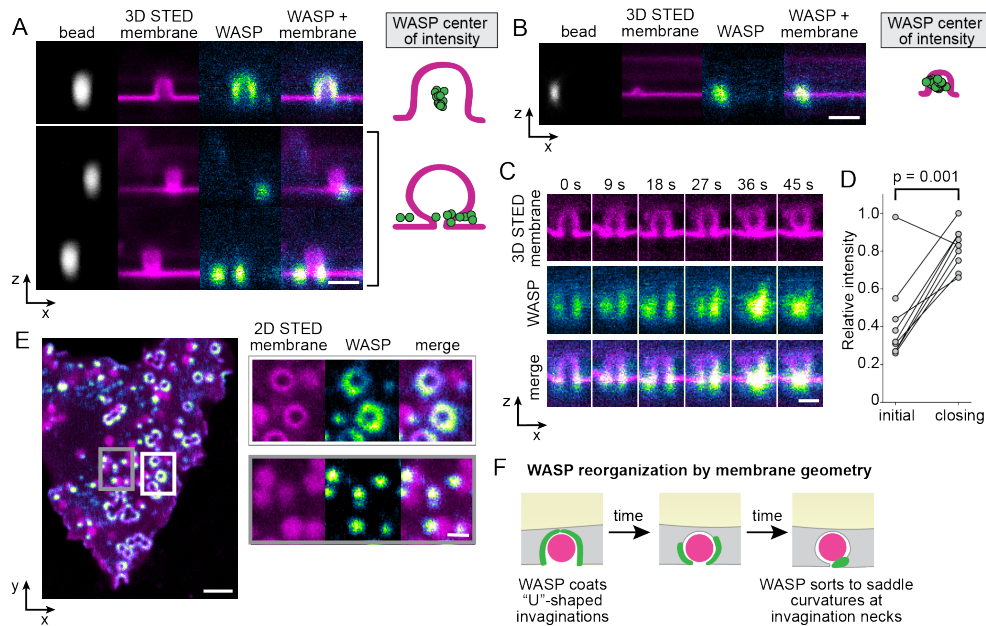
Figure 3.3

Figure 3.3 Super-resolution imaging reveals nanoscale reorganization of WASP by membrane geometry.

(A) Live cell 3D STED microscopy of the membrane coupled with confocal imaging of WASP on 500 nm beads show that WASP enriches to the site of highest inward curvature, either across the whole bud (top) or at a neck when present (bottom). Right hand side depicts the center of intensity of WASP for these two cases, with $n_{500nm, no\ neck}$ = 17 and $n_{500nm,\ neck}$ = 11 invaginations collected across 8 and 4 cells, respectively, from the same experiment. Scale bar is 1 μm.

(B) WASP enriches to the entire bead at smaller, 200 nm invaginations, as reflected in the center of intensity of WASP to the right. n_{200nm} = 29 invaginations collected across 9 cells from one experiment. Scale bar is 1 μm.

(C) Time lapse 3D STED imaging of the membrane reveals evolution from an open to closed-neck structure at sites of bead-induced invagination. As this occurs, WASP redistributes and moves from the bead surface to the invagination neck. Scale bar is 500 nm.

(D) As the membrane closes down around a bead, total WASP levels significantly increase. Mean normalized WASP intensity is 0.42 ± 0.08 AU at the first frame of the movie compared to 0.82 ± 0.04 AU at the time of neck closing on the single invagination level. A paired two-tailed t-test was used to compare the normalized intensity of WASP at these time points from nine invaginations collected across three experiments: p = 0.001.

162

(E) 2D STED imaging of the cell membrane reveals both open and closed invaginations. At open invaginations WASP coats the base (white box). As invaginations close down, WASP is reorganized into a focal accumulation at the neck (gray box). Scale bars are 2 µm and 500 nm in the inset. See Video 5 for the dynamics of this process.

(F) Model for WASP evolution as the membrane of a confined cell constricts around a bead.
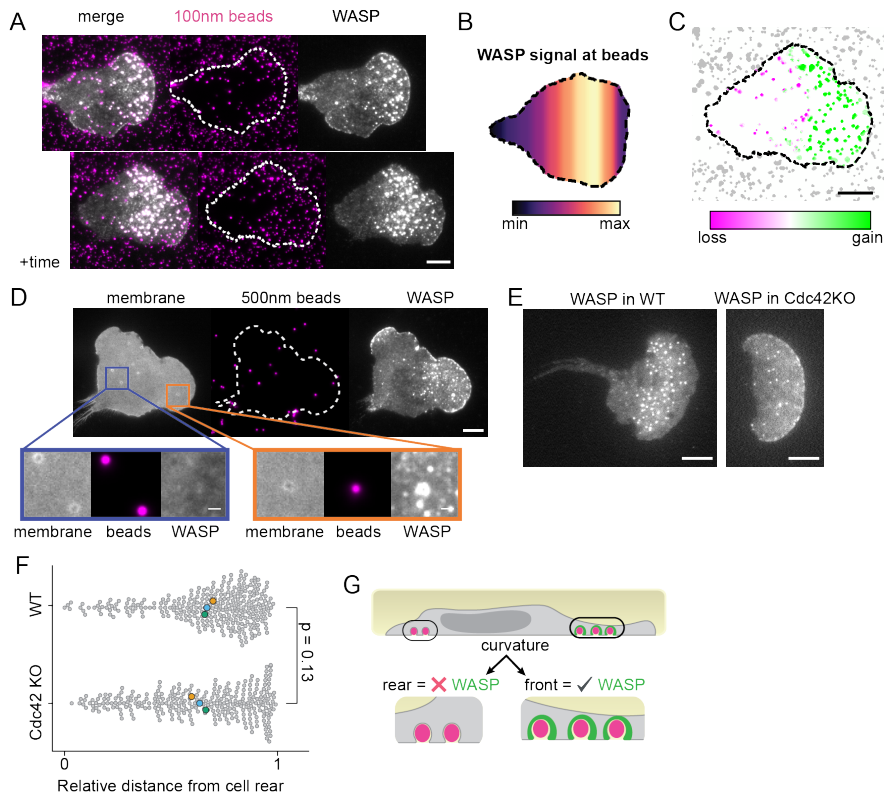
Figure 3.4

Figure 3.4 WASP recruitment depends on both curvature and cell polarity.

(A) WASP enriches to bead-induced membrane deformations only at the cell front. Beads that have signal in the top montage lose signal as they move towards the cell rear. Images are approximately 5 minutes apart.

(B) Spatial distribution of average WASP signal from approximately 135 beads that traverse the cell length. Data was collected across three experiments. The average WASP signal at a bead peaks in the front 20 to 40% of the cell and then falls off despite continued presence of the bead under the cell.

(C) Comparison of WASP signal gain and loss at beads from time point data in (A). Beads at the cell front gain WASP while beads at the cell rear lose WASP.

(D) Membrane labeling confirms that beads continue to deform the membrane as they approach the cell rear yet no longer recruit WASP. Orange inset shows a bead at the front that deforms the membrane and recruits WASP, while the purple inset shows beads at the cell rear that deform the membrane but do not recruit WASP. Scale bar of the inset is 1 μm.

(E) Exogenous WASP forms puncta in Cdc42 KO cells.

164

(F) The position of WASP puncta appearance in both wild type and Cdc42 KO cells is biased toward the cell front and is not significantly different by an unpaired two-tailed t-test on replicate means: p = 0.13. More than 280 total puncta were measured for each cell background in 12 and 14 cells, respectively, that were collected across three experiments. Enlarged markers denote replicate means. Mean relative position of WASP puncta appearance is 0.68 ± 0.01 in wild type cells and 0.64 ± 0.02 in Cdc42 KO cells on the replicate level, with the cell rear defined as 0 and the cell front defined as 1.

(G) Updated model to reflect that that membrane curvature alone is not sufficient to drive WASP recruitment. Scale bars are 5 µm unless otherwise specified.
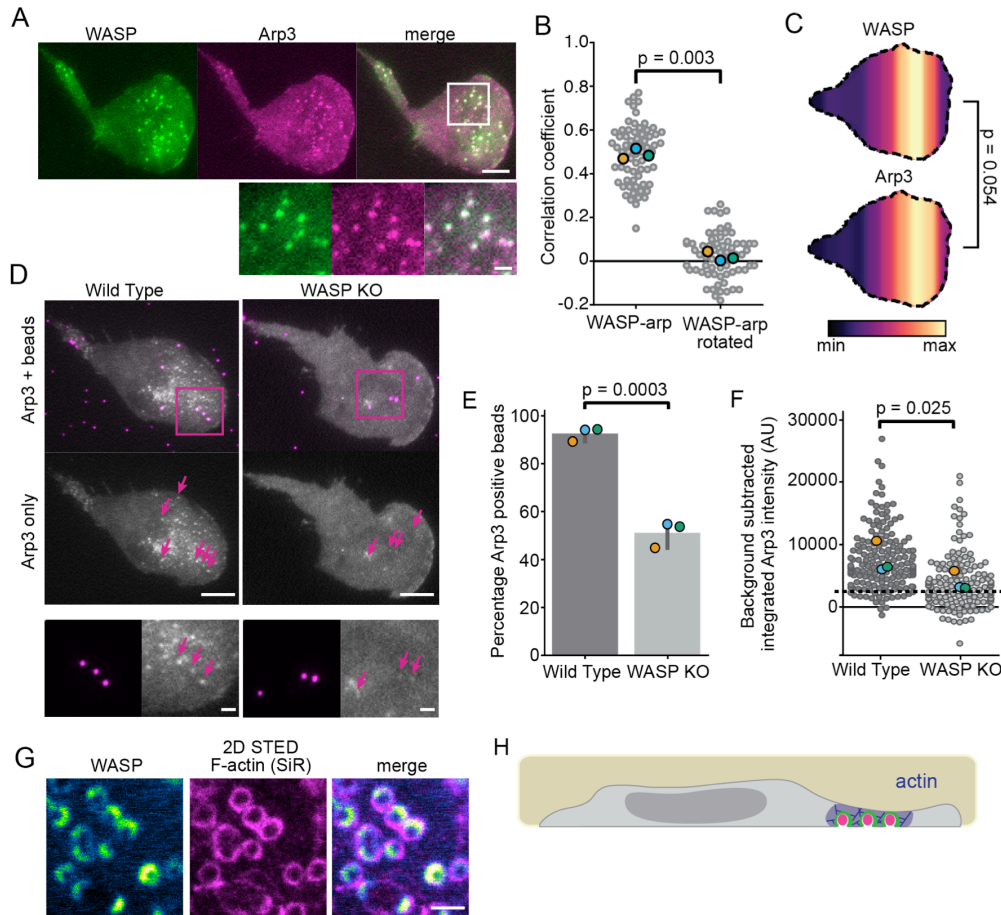
Figure 3.5

Figure 3.5 WASP mediates actin polymerization at sites of membrane deformation.

(A) Endogenous WASP co-localizes with TagRFP-T-Arp3. Scale bars are 5 μm and 1 μm in the inset.

(B) Pearson correlation coefficients of WASP and Arp3 show significant co-localization (r = 0.49 ± 0.01) compared to the correlation coefficients between WASP and a 90° rotation of the Arp3 channel (0.02 ± 0.02). n = 68 7.5X7.5 μm ROIs collected across three experiments. p = 0.003 by a paired two-tailed t-test on replicate means, which are denoted throughout the figure by enlarged markers.

(C) Spatial distributions of WASP and Arp3 puncta reveal similar organization. n = 18 co-expressing cells collected across three experiments with nWASP = 559 and nArp3 = 417 total puncta. The mean relative puncta position is 0.64 ± 0.02 for WASP and 0.65 ± 0.02 for Arp3, with the cell rear defined as 0 and the cell front defined as 1. p = 0.054 by a paired two-tailed t-test on the mean puncta position of each marker in each cell.

(D) WASP-null cells fail to recruit appreciable amounts of the Arp2/3 complex to 100 nm bead-induced invaginations. Arrows denote the position of beads that are under the lamellipod. Below is a zoomed inset of the boxed region. All images are scaled equally. Scale bars are 5 μm and 1 μm in the inset.

(E) Only about half of the beads (51.3 ± 3.1%) confined under lamellipodia in WASP KO cells are able to form Arp2/3 puncta (determined by the ability to fit a Gaussian to Arp3 signal at a bead) compared to 93.7 ± 1.7% of beads for wild type cells. n_{WT} = 172 beads and n_{KO} = 130 beads collected across three experiments. p = 0.0003 by an unpaired two-tailed t-test on replicate means.

(F) Integrated intensity of background subtracted Arp3 signal at beads was calculated for the brightest Arp3 frame. The dashed line marks the approximate threshold needed to fit a Gaussian in panel (E). Measurements below this line are close to background or noise. The mean intensity of Arp3 at beads is 7696 ± 1454 AU in wild type cells and 4020 ± 886 AU in WASP KO cells on the replicate level. n_{WT} = 164 and n_{KO} = 143 beads collected across three experiments. p = 0.025 by a paired t-test on replicate means.

(G) WASP and F-actin (reported with SiR actin) co-localize at bead-induced membrane invaginations at the cell front. Scale bar is 1 μm.

(H) Updated model to reflect polarized WASP-dependent actin polymerization.
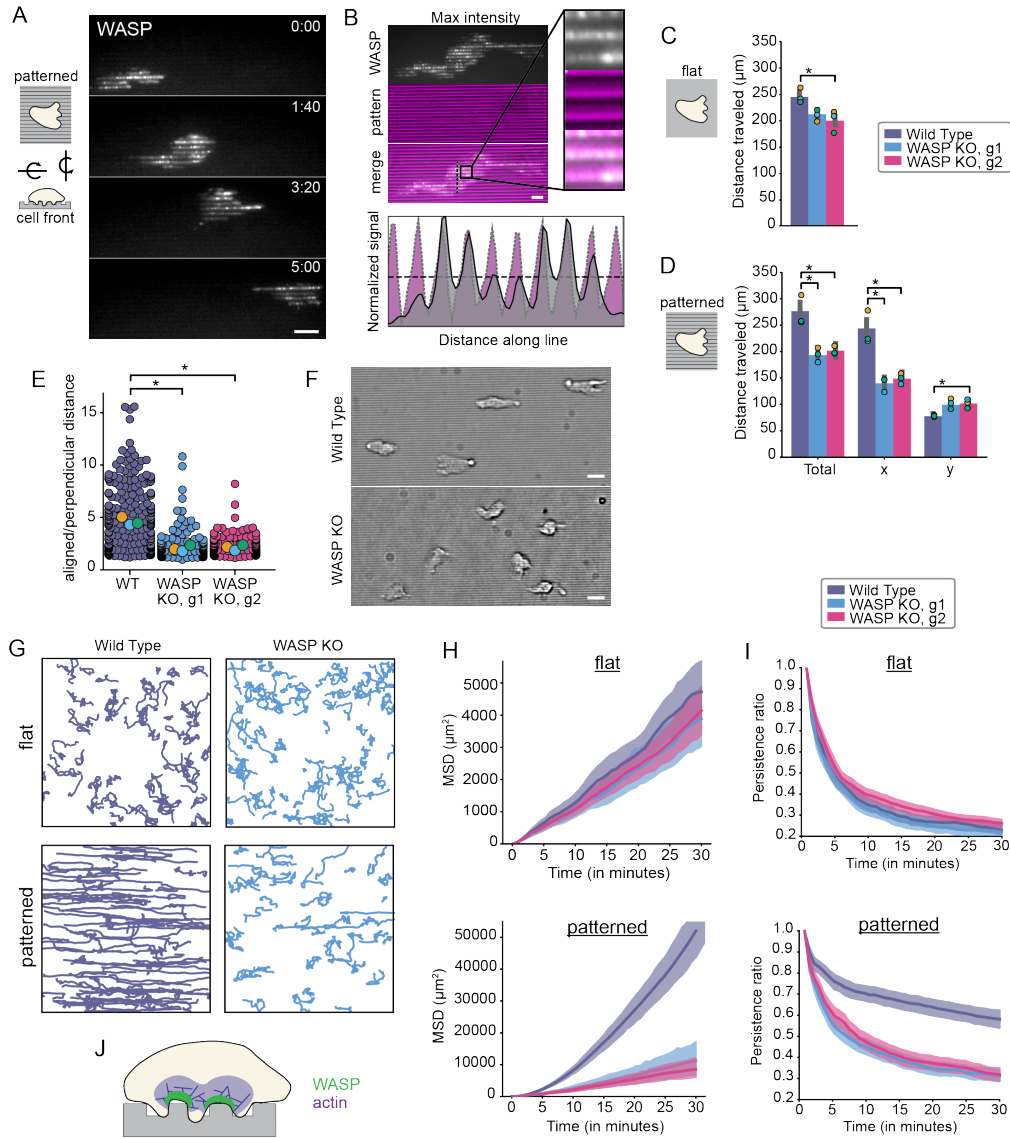
Figure 3.6

Figure 3.6 WASP-null cells are defective in their ability to interpret the topological features of their environment.

(A) WASP puncta enrich at nanoridges as cells migrate over patterns. Scale bar is 10 μm.

(B) Max intensity projection of data in (A) shows that WASP localizes to nanoridge peaks. An intensity profile for WASP and the pattern along the vertical line in the merged image is shown below. Scale bar is 5 μm and the inset is approximately 4x4 μm.

(C) There is a modest difference in the total distance traveled by wild type (purple) and WASP KO (guide 1 = blue, guide 2 = magenta) cells plated on flat substrates. n_{WT} = 253 cells, n_{KO1} = 215 cells, and n_{KO2} = 181 cells collected across three experiments. Total distance traveled: wild type = 246 ± 1 µm, WASP KO1 = 210 ± 6 µm, and WASP KO2 = 201 ± 12 µm on the replicate level. Replicate means are denoted throughout the figure by enlarged markers. Only one of the WASP KO clones was significantly different from wild type. For this case, p = 0.026 by a paired two-tailed t-test on replicate means. In the other case, p = 0.13. See also Video 6.

(D) The total distance traveled by WASP KO cells is significantly less than that of wild type cells on nanoridged substrates due to defective movement along the patterns (here the x-axis). n_{WT} = 188 cells, n_{KO1} = 172 cells, and n_{KO2} = 242 cells collected across three experiments. Total distance traveled: wild type = 273 ± 17 µm, WASP KO1 = 194 ± 8 µm, and WASP KO2 = 202 ± 5 µm on the replicate level. Total distance traveled in x: wild type = 241 ± 19 µm, WASP KO1 = 139 ± 8 µm, and WASP KO2 = 149 ± 6 µm on the replicate level. Total distance traveled in y: wild type = 78 ± 1 µm, WASP KO1 = 102 ± 6 µm, and WASP KO2 = 102 ± 5 µm on the replicate level. Asterisk denotes $p < 0.05$, which was determined by a paired two-tailed t-test on replicate means. Unless labeled, the difference is not significant. p-values: $p_{total,WT/KO1}$ = 0.018, $p_{total,WT/KO2}$ = 0.028, $p_{x,WT/KO1}$ = 0.023, $p_{x,WT/KO2}$ = 0.023, $p_{y,WT/KO1}$ = 0.061, $p_{y,WT/KO2}$ = 0.035. See also Video 7.

(E) Ratio of aligned to perpendicular migration reported in (D) highlights defective nanopattern sensing by WASP KO cell lines. Average ratio of total aligned to total perpendicular distance traveled: wild type = 4.02 ± 0.23, WASP KO1 = 1.47 ± 0.17, and WASP KO2 = 1.57 ± 0.15 on the replicate level. Asterisk denotes $p < 0.05$, which was determined by a paired two-tailed t-test on replicate means. $p_{WT/KO}$ = 0.012 and $p_{WT/KO2}$ = 0.008.

(F) Bright field images reveal clear alignment of wild type cells to horizontal nanoridges while WASP-null cell largely fail to align. Scale bar is 5 µm.

(G) Wild type and WASP-null cell trajectories over one hour for cells migrating on flat substrates (top) and nanoridged substrates (bottom). Image dimensions are approximately 665 x 665 µm.

(H) The mean squared displacements (MSDs) of wild type and WASP-null cells are indistinguishable on flat substrates (top) while the MSDs of WASP-null cells are significantly less than that of wild type cells on nanoridged substrates (bottom). Shading denotes a 95% confidence interval. Trajectories are the same as those assayed in (C) and (D), respectively. Of note, the MSD of wild type cells is ten-fold greater on nanoridged substrates than on flat substrates.

(I) The persistence ratios of wild type and WASP-null cells are indistinguishable on flat substrates (top) while the persistence ratios of WASP-null cells are significantly less than that of wild type cells on nanoridged substrates (bottom). Shading denotes a 95%

confidence interval. Trajectories are the same as those assayed in (C) and (D), respectively.

(J) Model of the role of WASP and WASP-mediated actin polymerization in topology sensing and contact guidance.
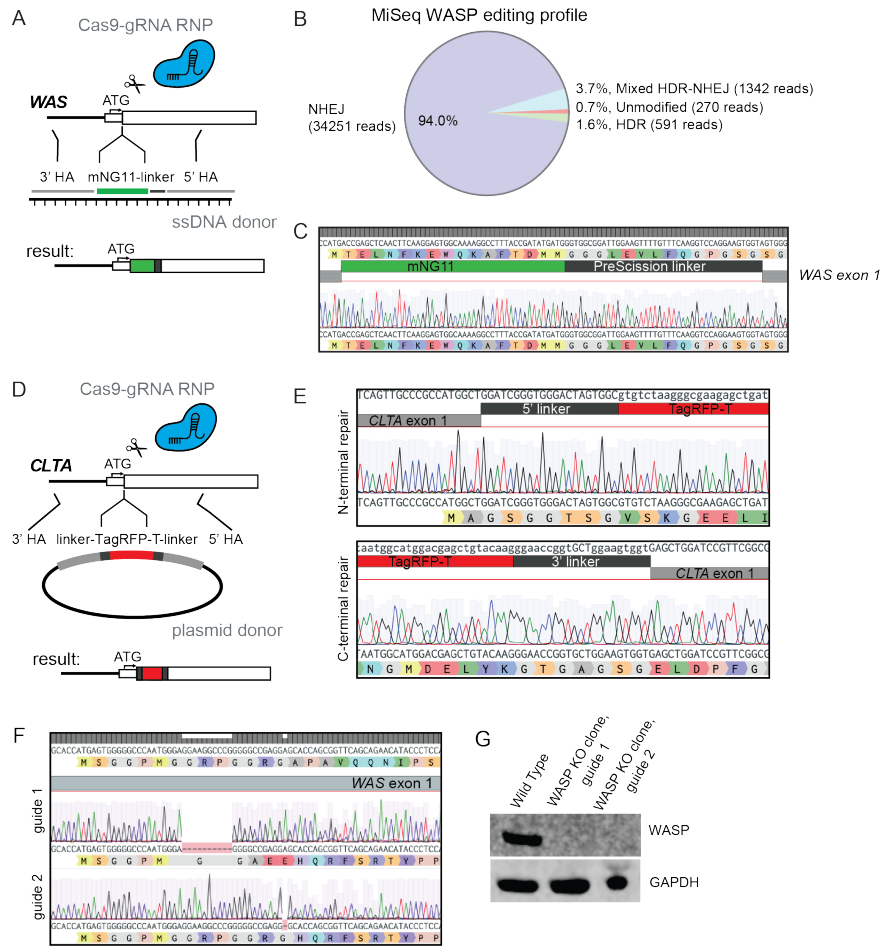
Figure S3.1

Figure S3.1 Genetic engineering of HL-60 cells.

(A) Strategy for endogenous tagging of WASP with split mNeonGreen2 using a Cas9-sgRNA RNP complex and ssDNA donor.

(B) MiSeq results from (A) reveal high cutting efficiency in HL-60s but poor homology directed repair. Analysis of paired end reads was done with CRISPResso2 (Clement et al., 2019).

(C) Sequencing of WASP knock-in cells confirms correct insertion of mNeonGreen2$_{11}$ tag.

(D) Strategy for endogenous tagging of clathrin light chain A with full length TagRFP-T using a Cas9-sgRNA RNP complex and plasmid donor.

(E) Sequencing of an isolated homozygous *CLTA* knock-in clone shows correct repair at both ends of the cut site.

(F) Sequence validation of the two clonal WASP KO lines assayed. Both lines have deletions that lead to a frame shift, nonsense, and termination following the end of the first exon.

(G) Western blot confirms that WASP is absent in both assayed clonal lines.
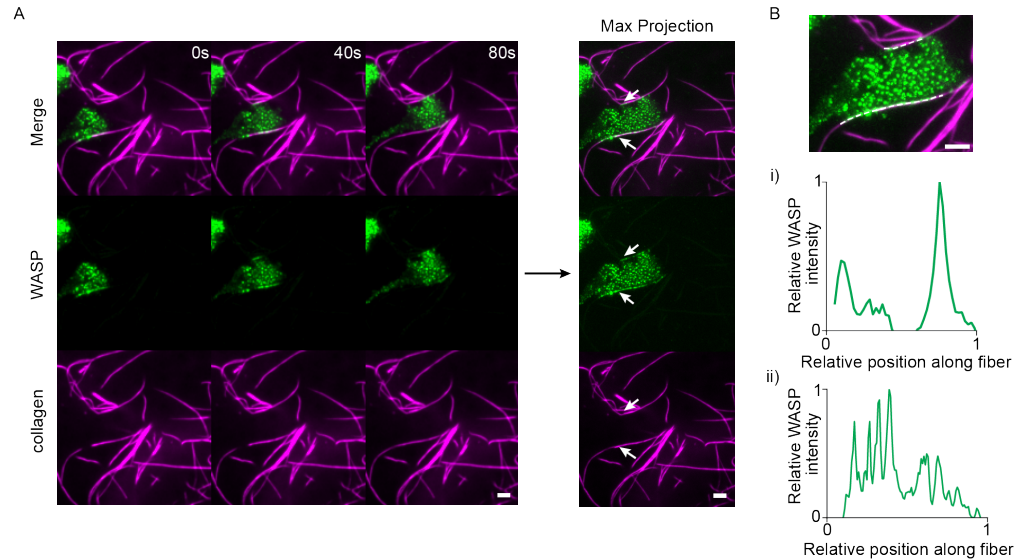
Figure S3.2

Figure S3.2 WASP enriches at sites of collagen-induced membrane deformation.

(A) Endogenous WASP is recruited to sites of cell contact with collagen fibers. Right hand side shows the maximum intensity projection over time, which highlights the enrichment of WASP to cell-fiber interfaces. Stretches of contact are marked with arrows.

(B) Relative background-subtracted maximum WASP signal along the two fibers marked in (A). (i) is along the upper fiber and (ii) is along the lower fiber, which are marked by dashed lines in the top image. Scale bars are 5 µm. Imaged with TIRF microscopy.
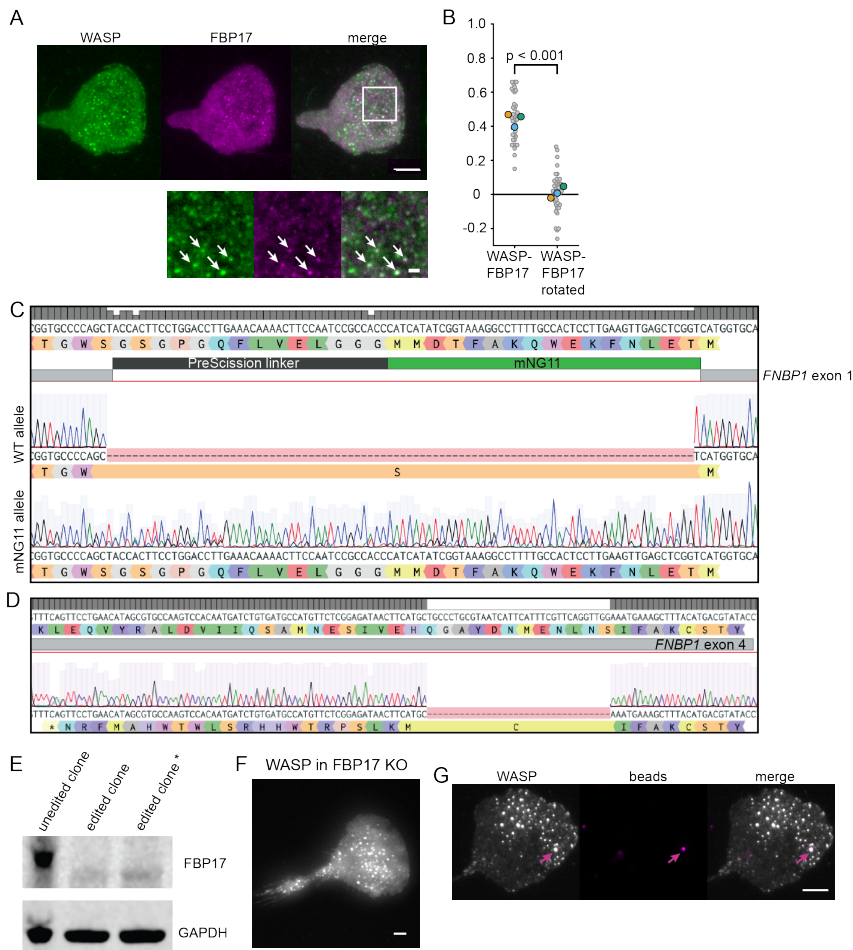
Figure S3.3

Figure S3.3 FBP17 co-localizes with WASP but is not required for WASP curvature sensitivity.

(A) Overexpressed WASP and endogenous FBP17 co-localize. Below shows a zoomed inset with arrows marking example positions of overlap. Scale bar is 1 µm in the inset.

(B) Pearson correlation coefficients between WASP and FBP17 in 38 7.5X7.5 µm ROIs reveal significant co-localization (r = 0.44 ± 0.02) compared to a 90 degree rotated control (0.01 ± 0.02). Data is collected over three experiments. p = 1.51E-17 by a paired two- tailed t-test on the full distribution.

(C) Sequencing shows a wild type allele and a correct insertion of mNG2$_{11}$ in the isolated heterozygous FBP17 knock-in clone.

(D) Sequencing of an FBP17 KO line shows homozygous deletion of 34 base pairs after amino acid 74, which causes a frame shift and early termination that disrupts the BAR domain (amino acids 1-264).

174

(E) Western blot confirms absence of FBP17 in the assayed FBP17 clonal line (marked with an asterisk).

(F) Overexpressed WASP continues to form puncta in an FBP17 KO background.

(G) Overexpressed WASP continues to enrich to bead-induced membrane invaginations in the absence of FBP17. Scale bar is 5 μm.
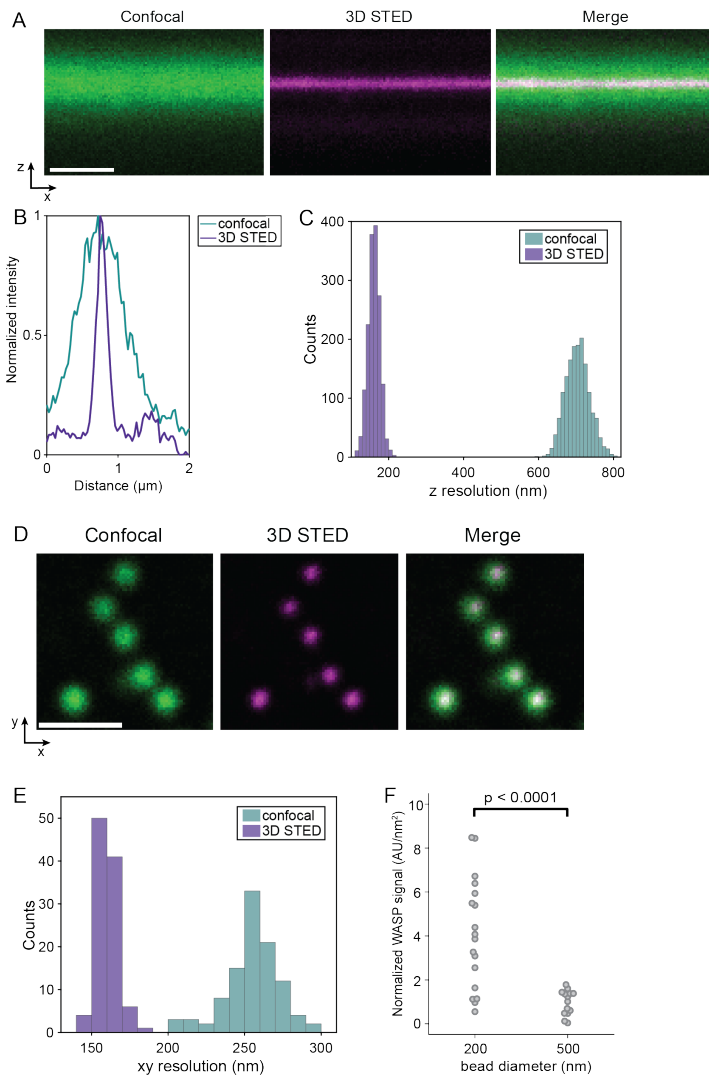
Figure S3.4

Figure S3.4 Increased spatial and axial resolution achieved by 3D STED in HL-60 cells.

(A) Confocal (left), 3D STED (middle) and merged (right) image of an XZ slice of the ventral membrane of an HL-60 cell labeled with CellMask Deep Red. Scale bar is 1 μm.

(B) Representative fluorescence intensity profile along the axial direction in confocal (green) and 3D STED (magenta).

(C) Histogram of axial resolution in confocal (green) and 3D STED (purple) imaging mode. 3D STED imaging provides a 4.4x increased axial resolution (160 ± 16 nm for 3D STED versus 704 ± 31 nm for confocal). The axial resolution is determined by the full-

width half-maximum of a Gaussian fit to axial intensity profiles of the confocal and 3D STED images (n = 1600 profiles).

(D) Estimation of the lateral (XY) spatial resolution offered by 3D STED through imaging fluorescent beads (40 nm) in confocal (left) and 3D STED (right) mode with the same settings as in live-cell experiments.

(E) Histogram of spatial resolution in confocal (green) and 3D STED (purple) imaging mode. 3D STED imaging provides a 1.6x increased spatial resolution (160 ± 6 nm for 3D STED versus 255 ± 17 nm for confocal). Spatial resolution is calculated by the full-width half-maximum of 2D Gaussian fits to the beads (n = 102 beads). Scale bar is 1 µm.

(F) Integrated intensity of thresholded WASP signal across XYZ stacks reveals significant enrichment of WASP to 200 nm beads compared to 500 nm beads (non-neck invaginations) when normalized to bead surface area. Mean normalized WASP intensity per unit area is 4.08 ± 0.59 AU/nm^2 for 200 nm beads and 0.97 ± 0.15 AU/nm^2 for 500 nm beads. p = 8.81E-05 by an unpaired two-tailed t-test on the normalized WASP intensities at all beads. n_{200nm} = 18 beads collected from two experiments and n_{500nm} = 14 beads collected from one experiment.
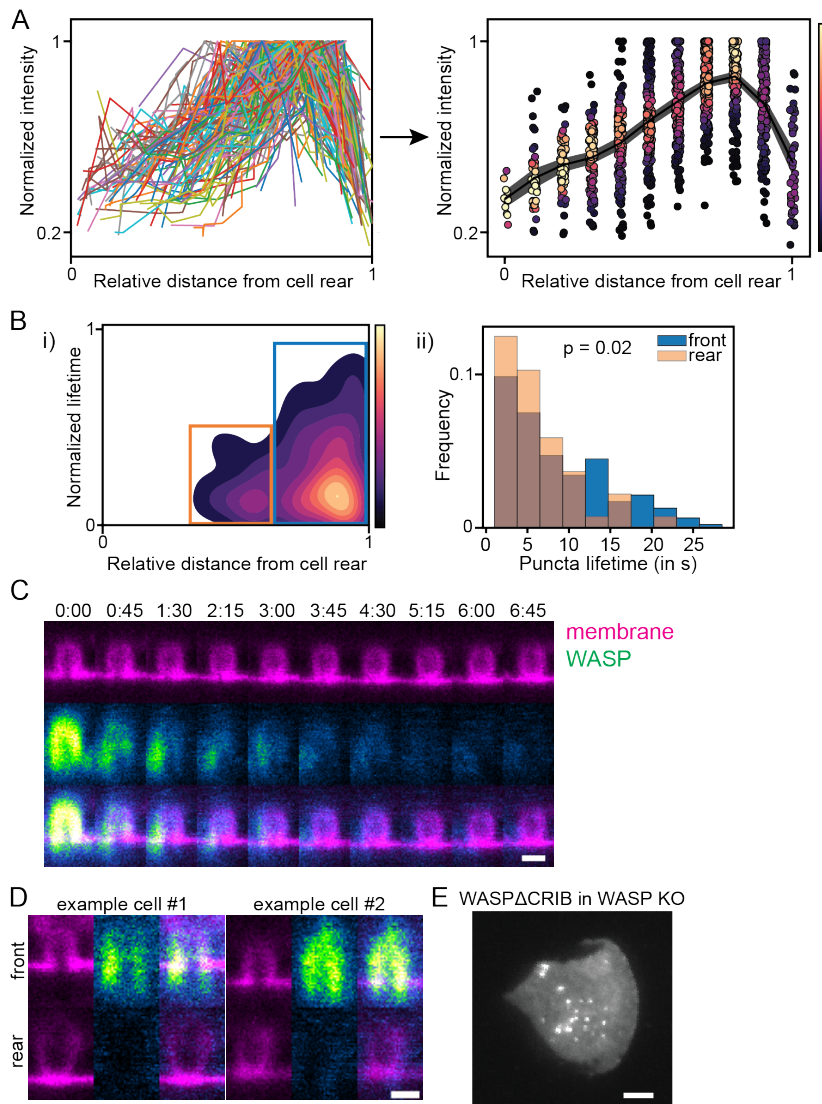
Figure S3.5

Figure S3.5 Further investigation of the effect of polarity on WASP recruitment and dynamics.

(A) Normalized traces of integrated WASP signal at 135 beads that travel the cell length. Data was collected across three experiments. Traces exhibit consistent behavior, peaking in the front half of the cell and falling off as the bead approaches the cell rear. Right side of the panel shows the averaged data with individual points overlaid and colored by data density.

(B) (i) Kernel density estimation comparing the position of puncta appearance with lifetime reveals two populations (boxed). (ii) Histograms of the boxed populations show puncta that appear closer to the cell rear extinguish faster, suggesting that position within the cell influences disappearance. More than 200 puncta were collected across 7

cells from two experiments. Mean lifetime is 8.50 ± 0.49 s for puncta that nucleate in the front 35% of the cell (blue box) and 6.24 ± 0.67 s for puncta that nucleate further back (orange box). p = 0.02 by an unpaired two-tailed t-test on all puncta lifetimes.

(C) Time lapse STED imaging shows membrane invaginations maintain geometry but lose WASP signal as the cell continues moving. Scale bar is 500 nm.

(D) Single XZ STED slices of beads at the cell front and cell rear of the same cell show that despite similar geometry WASP is only recruited to invaginations at the front. Images are scaled to the same intensity. Scale bar is 500 nm.

(E) WASP KO cells rescued with endogenous levels of fluorescent WASPΔCRIB form puncta. Scale bar is 5 µm.

CHAPTER FOUR

RHO GEFS AND GAPS IN CELL POLARITY

SUMMARY

Our current understanding of the Rho GEFs and GAPs involved in cell polarity is limited. Here we present a CRISPR knock-in screen where we endogenously label approximately 50 highly expressed Rho GEFs and GAPs in HEK293T cells. Through a localization screen we arrive at eight candidate Rho GEFs and GAPs that enrich to membrane protrusions in chemically polarized HEK293T cells. We outline future directions to follow up these candidates, including targeted knockout in HEK293T cells and small localization and loss-of-function screens in the harder-to-edit neutrophil-like HL-60 cell line. This project aims to provide insight into the complex mechanisms underlying polarized Rho GTPase regulation and ultimately neutrophil polarity.

INTRODUCTION

Polarized Rho GTPases pattern branched actin polymerization at the leading edge of motile neutrophils (Fenteany and Glogauer, 2004; Yang et al., 2016). These GTPases are regulated in part by Rho GEFs and GAPs, but the exact GEFs and GAPs involved in protrusion generation remain unclear. This is due in part to complex crosstalk among both Rho GTPases and their GEFs and GAP (Müller et al., 2020; Pestonjamasp et al., 2006). Additionally, there exist more than one hundred (potentially redundant) proteins with GEF or GAP domains (Bos et al., 2007).

Localization studies have been used to identify candidate GEFs and GAPs involved in cell polarity (Nguyen et al., 2016) and wound healing (Vaughan et al., 2011). However, overexpression of these proteins can obscure GTPase dynamics and induce aberrant cell morphologies. Here we leverage CRISPR and high rates of homology directed repair in HEK293T cells to make a library of approximately 50 endogenously tagged Rho GEFs and GAPs.

To repurpose HEK293Ts as a model system for cell polarity, we find conditions that cause them to polarize and form lamellipodia. We next use a cytosolic normalization scheme to measure membrane enrichment of our endogenous Rho GEFs and GAPs in these chemically polarized HEK293Ts. Finally, we provide an assay for phenotyping migration defects in candidate knockout HEK293T cell lines and present a Rac1 knockout line as a positive control. Promising candidates from subsequent localization and loss-of-function screens in HEK293T cells would warrant advancement to

neutrophil-like HL-60 cells. Observations in this motile cell line could provide insight into cell polarity establishment and regulation.

RESULTS

Library design and cell generation

Endogenous tagging has allowed us to assess native protein localization and dynamics with virtually no drawbacks. However, a limitation of this technique is that only about 50% of the proteome provides enough signal to be imaged above background noise (Cho et al., 2021). Still, advances are being developed to combat this, including tandem fluorophore knock-in (Kamiyama et al., 2016). We took this concern into consideration when constructing our Rho GEF and GAP library. We chose proteins with a TPM (transcripts per million) value of >10, but proteins close to this threshold did prove difficult to image. We started with 47 Rho GEFs and GAPs that met the TPM threshold according to RNA-seq of HEK293T cells (**Table 1**) and successfully tagged 45 of the 47 targets. Localization of these proteins in HEK293T cells is presented in **Figure 1**.

Polarization of HEK293T cells

HEK293T cells offer high efficiencies for endogenous tagging, however, they are not necessarily the best system to study cell polarity. We took this into consideration and tested a number of perturbations to induce actin fronts in HEK293Ts and other cell lines with established high-throughput editing strategies (**Fig 2**). We found that the Protein Kinase C activator phorbol 12-myristate 13-acetate (PMA) robustly induced lamellipodia in all three cell-types tested. Notably, PMA caused more robust lamellipod formation in HEK293T cells than it did in HT1080 and U2OS cells, supporting our choice to move forward with this cell line. We repeated imaging in polarized HEK293T cells and saw that a number of our candidates underwent localization changes (**Fig 3**), which was

184

fitting given overall changes in cell morphology. Of note, PMA treatment takes affect immediately, so dynamic protein and cytoskeletal rearrangement can be observed. Time lapse imaging of a subset of the library could provide further insight into GEF/GAP function.

Cytosolic reporter generation and image normalization

Despite clear changes in the localization of our targets, enrichment to protrusions can be subtle. Additionally, we needed an unbiased metric to equally compare all candidate proteins to one another. To accomplish this we used a cytosolic normalization scheme as described in (Van Haastert et al., 2017). Briefly, the difference between the channel for the protein of interest and a weighted cytosolic channel (weighted here by the ratio of intracellular signal from the protein of interest to intracellular signal from the cytosolic marker) is normalized to the mean intracellular signal of the protein of interest. This yields an image where values greater than zero represent fold increase over cytosolic localization while those less than zero represent depletion. This scheme also highlights membrane localization, which is particularly apparent in lamellipodia due to their high surface area to volume ratio. We chose this approach over a membrane normalization scheme because we are interested in general localization to the membrane since this is where GEFs and GAPs are active. Controls and the eight candidates to emerge from this normalization screen are presented in **Figure 4**. Of note, only 34 of the original 45 proteins were taken through this screen because of signal to noise limitations (**Table 1**).

An important consideration we did not anticipate was bleed through from other channels. Endogenous tagging often results in low signal to noise, requiring long exposure times to resolve signal. Because of this, it is important to be mindful of the intensity of the normalization probe. We used lentivirus to transduce an mScarlet-conjugated cytosolic reporter and found significant bleed through into the 488 nm channel despite using a low multiplicity of infection. Because of this, we needed to swap our fluorescent marker to one with dim signal and had success with mCherry.

Phenotyping loss of function in candidate KO cell lines

With candidates in hand, the next step is to determine the contribution of these proteins to cell polarity and migration. We found that PMA-treated HEK293T cells migrate significantly over a four-hour time window. To test whether we could detect migration defects in these usually stationary cells, we compared wild type to Rac1 knockout HEK293T cells. We found that, unsurprisingly, loss of Rac1 deeply impairs cell migration (**Fig 5**). This assay can now be extended to phenotyping candidate knockout lines.

DISCUSSION

Following up candidates from the normalization screen

We initially proposed to conduct loss-of-function experiments for GEF and GAP

candidates in HEK293T cells. However, this cell line is mostly triploid (Bylund et al.,

2004), making sequence validation of clones more difficult. Since beginning this project

we have achieved high rates of non-homologous end joining in HL-60 cells, so we now

propose following up the eight screen candidates directly in this cell line. Because of the

work needed to establish and validate clonal lines, we first advocate overexpression of

the candidates in HL-60 cells. Those that exhibit polarity, which should be more obvious

in persistently polarized and migratory HL-60 cells than in HEK293T cells, would

warrant generating a CRISPR knockout. In addition to migration defects, one can assay

GTPase activity using biosensors, as done in (Yang et al., 2016).

Overview of the returned screen candidates

ARHGAP35

Immunofluorescence of ARHGAP35 reveals enrichment to the tips of lamellipodia

(Binamé et al., 2016; Bravo-Cordero et al., 2013). ARHGAP35 is thought to primarily

function through negative regulation of RhoA and RhoC. Overexpression of ARHGAP35

mutants found in cancers affects the migration of MDA-MB-231 cells (Binamé et al.,

2016).

ARHGAP8

The functional role of ARHGAP8 is poorly annotated. Its primary reference is its identification paper (Johnstone et al., 2004). In this paper, it is reported that ARHGAP8 has a similar sequence to ARHGAP1 and is overexpressed in cancer, which the authors suggest could be the cell's way of coping with increased levels of Rho, Rac, and Cdc42 expression.

DEPDC1B

Ectopic expression of DEPDC1B increases the migratory and invasive capacity of non-small cell lung cancer cells while DEPDC1B knockdown suppresses these traits (Yang et al., 2014). This paper highlights a role for DEPDC1B in Wnt/β-catenin signaling but fails to mention GTPases. However, Rac1 has been implicated in β-catenin accumulation and nuclear translocation (Esufali and Bapat, 2004). A recent paper highlights a role for this protein in increased cell migration and invasion via Rac1 (Zhang et al., 2020).

DOCK7

DOCK7 has been implicated in Schwann cell migration through activation of Rac1 and Cdc42 (Yamauchi et al., 2008). In an *in vivo* neuronal model, DOCK7 depletion leads to shorter leading processes and decreased migration of neuroblasts (Nakamuta et al., 2017). DOCK7 has also been implicated in filopod generation in cancer cells (Yamamoto et al., 2013).

MYO9B

MYO9B was shown to be necessary for lamellipod formation in primary murine macrophages (Hanley et al., 2010). New work from this group explores the molecular mechanism of this phenotype: Rac activations leads to actin polymerization and MYO9B recruitment, which, in turn, locally inhibits Rho and promotes migration and lamellipod formation (Hemkemeyer et al., 2021).

PIK3R1

PIK3R1 (also known as p85α) is a regulatory subunit of Phosphatidylinositol 3-kinase (PI3K), which is an important contributor to cell polarity. While closely related to oncogenic PIK3R2, PIK3R1 exhibits opposite, tumor-suppressive properties. Namely, depletion of PIK3R1 promotes cellular transition from epithelial to mesenchymal states (Lin et al., 2015). However, overexpression of PIK3R1 can also promote migration via transient Cdc42 activation (Jiménez et al., 2000).

ARHGEF7

ARHGEF7 (also known as β-pix) is a Rac1 and Cdc42 GEF. In developing mesoderm, ARHGEF7 mutant cells struggle to coordinate their migration and fail to form sensory filopodia (Omelchenko et al., 2020). ARHGEF7 was also identified through an RNAi screen as a Rac1 regulator, and depletion of this protein leads to randomly directed protrusive activity during collective endoderm migration (Omelchenko et al., 2014). ARHGEF7 is frequently upregulated in cancers and its expression correlates with migration and invasiveness (Lei et al., 2018).

ARHGEF12

ARHGEF12 (also known as LARG) activates RhoA. In endothelial cells, force application to ICAM-1 clusters induces cell stiffening and increased RhoA activity through ARHGEF12 (Lessey-Morillon et al., 2014). This protein has also been implicated in RSK2-mediated cell migration (Shi et al., 2017). Preliminary work presents ARHGEF12 as an important regulator of pro-migratory phenotypes among ETV6-RUNX1+ B-cell precursor acute lymphoblastic leukemia (Polak et al., 2015).

Reflection on candidates

Interesting targets arose from our screen. The fact that PIK3R1, a protein associated with PI3K, which is important for polarity in HL-60 cells, shows up in our final candidate list supports that the screen is correctly identifying polarity regulators. Interestingly, the majority of our final candidates have not been studied in immune cells. The one that has, MYO9B, was found to be essential for lamellipod formation in macrophages (Hanley et al., 2010). These "sanity checks" lead us to believe that there are important players lurking in this small list.

Candidates that fell through the cracks

Due to signal to noise limitations, potential candidates were missed. Obvious points where this occurred are (1) in our initial candidate selection where we gated on TPM values and (2) in the decreased number of candidates assayed in the normalization screen. To combat this in the future, the use of brighter fluorophores (including SNAP

and HALO-tags) as well as tandem-fluorophore knock-in (Kamiyama et al., 2016) could help us extend our imaging into lower expressed candidates. Alternatively, if we continue on this track, safeguards like using highly sensitive imaging set-ups and the dim fluorophores in other channels during co-labeling experiments will be essential. While signal-to-noise concers limited this screen to a small pool of candidates, it did allow us to quickly converge on a feasible number of GEF and GAP leads. Even with this shallow sampling, interesting candidates emerged.

MATERIALS AND METHODS

Endogenous tagging of HEK293T cells with split mNeonGreen2

For the library we used split mNeonGreen2 (Feng et al., 2017). The parental HEK293T cell line used was positive for the 1-10 segment of mNeonGreen2. This protein is not fluorescent on its own, but becomes fluorescent upon introduction of its compliment, mNeonGreen2$_{11}$. Expression of mNeonGreen$_{1-10}$ was confirmed by electroporating cells with an mCherry-conjugated mRNA of mNeonGreen$_{11}$. mNeonGreen2$_{1-10}$-positive cells became fluorescent in both the green and red channels, and cells with a single insertion of mNeonGreen2$_{1-10}$ were selected using fluorescence-activated cell sorting (FACS). The mRNA was degraded by the cell over the next few days, leading to a loss of fluorescence in both channels.

Non-fluorescent mNeonGreen$_{1-10}$ cells were electroporated with a Cas9-sgRNA complex targeting the gene of interest and a single-stranded donor sequence containing mNeonGreen2$_{11}$. Guides were designed using Benchling and selected for their proximity to the terminus of interest and for low predicted off-target cutting rates. The terminus to be targeted was based on overexpression constructs used in the literature. Donor sequences were 200 base pairs long and, in addition to mNeonGreen2$_{11}$, contained a small, cleavable linker and ~55 base pairs of homology to each end of the cut site.

Cells were pre-treated overnight with nocodazole to increase rates of homology-directed repair (Lin et al., 2014). Electroporation was conducted using an Amaxa 96-well shuttle

Nucleofector. Sample preparation was done in accordance with the manufacturer instructions and the electroporation program CM130 was used.

Sorting of positive knock-in lines

Cells that underwent correct insertion of mNeonGreen2$_{11}$ became fluorescent. Low-expression targets yielded FACS profiles similar to background. Additionally, HEK293T cells are largely triploid (Bylund et al., 2004), meaning that fluorescence can be explained by one, two, or three insertions. To enrich for homozygous insertion, which is critical for dim targets, cells in the top 0.5% of the FACS plot were isolated. Cell lines were then expanded and population level editing profiles were determined using MiSeq.

Polarization of HEK293T cells

In order to make HEK293Ts a better suited system for studying cell polarity, we piloted a number of stimulatory signals: PMA (Sroka et al., 2007), ALF$_4^-$ (Schmidt et al., 1998; Sallese et al., 2000), and acute serum addition (Machesky and Hall, 1997). For PMA, we settled on a saturating dose of 300 nM. For AlF$_4^-$, we treated cells with 30 mM as in (Sallese et al., 2000). For acute serum addition, we starved cells overnight and then introduced serum-containing media. We used phalloidin staining to assess actin levels and actin organization in response to these stimulations in HEK293T cells as well as HT1080 and U2OS cells. HT1080 and U2OS cells were chosen for their ability to form lamellipodia and for their high rates of homology directed repair. Surprisingly, PMA was able to induce robust lamellipodia in HEK293T cells but was not as effective in HT1080 or U2OS cells. Additionally, lamellipodia formed immediately in HEK293T cells after

PMA treatment and exhibited fast (minute time-scale) dynamics. Meanwhile AlF$_4^-$

induced lamellipodia in HT1080 and U2OS cells but not in HEK293T cells. Lamellipodia

that formed in this setting were actin-dense and contained large stress fibers. Finally,

acute addition of serum induced actin polymerization in all three cell-types but

lamellipodia in HEK293T and HT1080 cells were small. Conversely, acute addition of

serum led to the formation of large lamellipodia in U2OS cells. However, these

lamellipodia were again characterized by large stress fibers. Since neutrophils do not

form stress fibers, we decided the most structurally similar actin networks were those

seen in the lamellipodia of PMA-trated HEK293T cells, motivating us to move forward

with this cell line and this treatment condition.

Transduction with and normalization to a cytosolic marker

Because many of our targets were dim and close to background noise, partial

enrichment to a cellular compartment like lamellipodia would be hard to detect.

Additionally, we needed an unbiased, robust metric that could be applied across

candidates. To address this we used a cytosolic normalization scheme as presented in

(Van Haastert et al., 2017). Briefly, we compute $\Psi(i)$ = $(G_i\text{-}cR_i)/\langle G_c\rangle$ where $\Psi(i)$ is the

amount of candidate enrichment to the membrane (activity) at pixel i, G and R are the

background-subtracted green (target) and red (normalization) channels, c is a scaling

factor representing the ratio of green to red intracellular intensities, and $\langle G_c\rangle$ is the

mean intracellular signal of the target channel. Intracellular values are calculated from

small, uniform ROIs that were manually selected in FIJI. This approach yields an up to

10-fold increase in sensitivity (Kortholt et al., 2013). Analysis was performed on the

single cell level to account for differences in the expression level of the normalization marker. Additionally, to increase signal and to collapse analysis to 2D, normalization was performed on max intensity projections of z-stacks.

For our normalization probe we used a lentivirally-encoded NES-conjugated mCherry. We used HEK293T cells to make lentivirus at scale (in a 10 cm dish) to ensure enough material for the entire library. We transduced in a 96-well plate with 7 µL of virus per well, which should have yielded a multiplicity of infection of less than one. Our reporter also contained a puromycin resistance cassette. However, our infection rate was high and therefore did not require we select for expression.

HEK293T cells are good at taking up lentivirus and, despite our dilution, the cells ended up expressing high levels of the reporter. This was originally a problem since we used a bright fluorophore (mScarlet) in the reporter, and it bled into the target channel (488). It is not often appreciated how difficult it can be to image dim endogenous targets. Special attention must be paid to the fluorophores used for tagging and for any additional channels that are added. For example, bright cell stains like CellMask also bled through. Ultimately, switching to an mCherry-conjugated reporter resolved these issues.

Of note, our current normalization scheme to a cytosolic label can convolute enrichment to the membrane with enrichment to protrusions. This is because lamellipodia are thin and have a high membrane to cytosol ratio. Therefore, membrane associated proteins may appear to enrich at protrusions. For our application this is okay since GEFs and

GAPs at the membrane are active and therefore something we are interested in capturing. However, if one wanted to exclusively measure protrusion enrichment, it would warrant repeating this normalization scheme with a membrane label.

Microscopy

For the original library imaging +/- PMA, cells were imaged on a DMI-8 inverted microscope (Leica) equipped with a Dragonfly spinning-disk confocal system (Andor), a 63x 1.47NA oil objective (Leica), and a 16-bit iXon Ultra 888 EMCCD camera (Andor).

For the normalization experiments cells were imaged with a Nikon Eclipse Ti inverted microscope equipped with a Borealis beam conditioning unit (Andor), a CSU-W1 Yokugawa spinning disk (Andor), a 60X PlanApo TIRF 1.49 numerical aperture (NA) objective (Nikon), an iXon Ultra EMCCD camera (Andor), and a laser module (Vortran Laser Technology) equipped with 405, 488, 561, and 642 nm laser lines.

ACKNOWLEDGEMENTS

REFERENCES

Binamé, F., A. Bidaud-Meynard, L. Magnan, L. Piquet, B. Montibus, A. Chabadel, F. Saltel, V. Lagrée, and V. Moreau. 2016. Cancer-associated mutations in the protrusion-targeting region of p190RhoGAP impact tumor cell migration. *J. Cell Biol.* 214:859–873. doi:10.1083/jcb.201601063.

Bos, J.L., H. Rehmann, and A. Wittinghofer. 2007. Review GEFs and GAPs : Critical Elements in the Control of Small G Proteins. 865–877. doi:10.1016/j.cell.200.

Bravo-Cordero, J.J., V.P. Sharma, M. Roh-Johnson, X. Chen, R. Eddy, J. Condeelis, and L. Hodgson. 2013. Spatial regulation of RhoC activity defines protrusion formation in migrating cells. *J. Cell Sci.* 126:3356–3369. doi:10.1242/jcs.123547.

Bylund, L., S. Kytölä, W.O. Lui, C. Larsson, and G. Weber. 2004. Analysis of the cytogenetic stability of the human embryonal kidney cell line 293 by cytogenetic and STR profiling approaches. *Cytogenet. Genome Res.* 106:28–32. doi:10.1159/000078556.

Cho, N.H., K.C. Cheveralls, A.-D. Brunner, K. Kim, A.C. Michaelis, P. Raghavan, H. Kobayashi, L. Savy, J.Y. Li, H. Canaj, J.Y. Kim, E.M. Stewart, C. Gnann, F. McCarthy, J.P. Cabrera, R.M. Brunetti, B.B. Chhun, G. Dingle, M.Y. Hein, B. Huang, S.B. Mehta, J.S. Weissman, R. Gómez-Sjöberg, D.N. Itzhak, L.A. Royer, M. Mann, M.D. Leonetti, C. Zuckerberg Biohub, and S. Francisco. 2021. OpenCell: proteome-scale endogenous tagging enables the cartography of human cellular organization. *bioRxiv*. 2021.03.29.437450.

Esufali, S., and B. Bapat. 2004. Cross-talk between Rac1 GTPase and dysregulated Wnt signaling pathway leads to cellular redistribution of β-catenin and TCF/LEF-mediated transcriptional activation. *Oncogene.* 23:8260–8271. doi:10.1038/sj.onc.1208007.

Feng, S., S. Sekine, V. Pessino, H. Li, M.D. Leonetti, and B. Huang. 2017. Improved split fluorescent proteins for endogenous protein labeling. *Nat. Commun.* 8:370. doi:10.1038/s41467-017-00494-8.

Fenteany, G., and M. Glogauer. 2004. Cytoskeletal remodeling in leukocyte function. *Curr. Opin. Hematol.* 11:15–24. doi:10.1097/00062752-200401000-00004.

Van Haastert, P.J.M., I. Keizer-Gunnink, and A. Kortholt. 2017. Coupled excitable Ras and F-actin activation mediates spontaneous pseudopod formation and directed cell movement. *Mol. Biol. Cell.* 28:922–934. doi:10.1091/mbc.E16-10-0733.

Hanley, P.J., Y. Xu, M. Kronlage, K. Grobe, P. Schön, J. Song, L. Sorokin, A. Schwab, and M. Bähler. 2010. Motorized RhoGAP myosin IXb (Myo9b) controls cell shape and motility. *Proc. Natl. Acad. Sci. U. S. A.* 107:12145–12150. doi:10.1073/pnas.0911986107.

Hemkemeyer, S.A., V. Vollmer, V. Schwarz, B. Lohmann, U. Honnert, M. Taha, H.J. Schnittler, and M. Bähler. 2021. Local Myo9b RhoGAP activity regulates cell motility. *J. Biol. Chem.* 296:100136. doi:10.1074/jbc.RA120.013623.

Jiménez, C., R.A. Portela, M. Mellado, J.M. Rodríguez-Frade, J. Collard, A. Serrano, C. Martínez-A, J. Avila, and A.C. Carrera. 2000. Role of the PI3K regulatory subunit in the control of actin organization and cell migration. *J. Cell Biol.* 151:249–261. doi:10.1083/jcb.151.2.249.

Johnstone, C.N., S. Castellví-Bel, L.M. Chang, X. Bessa, H. Nakagawa, H. Harada, R.K. Sung, J.M. Piqué, A. Castells, and A.K. Rustgi. 2004. ARHGAP8 is a novel member of the RHOGAP family related to ARHGAP1/CDC42GAP/p50RHOGAP: Mutation and expression analyses in colorectal and breast cancers. *Gene.* 336:59–71. doi:10.1016/j.gene.2004.01.025.

Kamiyama, D., S. Sekine, B. Barsi-Rhyne, J. Hu, B. Chen, L.A. Gilbert, H. Ishikawa, M.D. Leonetti, W.F. Marshall, J.S. Weissman, and B. Huang. 2016. Versatile protein tagging in cells with split fluorescent protein. *Nat. Commun.* 7:1–9. doi:10.1038/ncomms11046.

Kortholt, A., I. Keizer-Gunnink, R. Kataria, and P.J.M.V. Haastert. 2013. Ras activation and symmetry breaking during dictyostelium chemotaxis. *J. Cell Sci.* 126:4502–4513. doi:10.1242/jcs.132340.

Lei, X., L. Deng, D. Liu, S. Liao, H. Dai, J. Li, J. Rong, Z. Wang, G. Huang, C. Tang, C. Xu, B. Xiao, and T. Li. 2018. ARHGEF7 promotes metastasis of colorectal adenocarcinoma by regulating the motility of cancer cells. *Int. J. Oncol.* 53:1980–1996. doi:10.3892/ijo.2018.4535.

Lessey-Morillon, E.C., L.D. Osborne, E. Monaghan-Benson, C. Guilluy, E.T. O'Brien, R. Superfine, and K. Burridge. 2014. The RhoA GEF, LARG, mediates ICAM-1-dependent mechanotransduction in endothelial cells to stimulate transendothelial migration. *J Immunol.* 192:3390–3398. doi:10.4049/jimmunol.1302525.The.

Lin, S., B.T. Staahl, R.K. Alla, and J.A. Doudna. 2014. Enhanced homology-directed human genome engineering by controlled timing of CRISPR/Cas9 delivery. *Elife*. 3:e04766. doi:10.7554/eLife.04766.

Lin, Y., Z. Yang, A. Xu, P. Dong, Y. Huang, H. Liu, F. Li, H. Wang, Q. Xu, Y. Wang, D. Sun, Y. Zou, X. Zou, Y. Wang, D. Zhang, H. Liu, X. Wu, M. Zhang, Y. Fu, Z. Cai, C. Liu, and S. Wu. 2015. PIK3R1 negatively regulates the epithelial-mesenchymal transition and stem-like phenotype of renal cancer cells through the AKT/GSK3β/CTNNB1 signaling pathway. *Sci. Rep.* 5:1–12. doi:10.1038/srep08997.

Machesky, L.M., and A. Hall. 1997. Role of actin polymerization and adhesion to
extracellular matrix in Rac- and Rho-induced cytoskeletal reorganization. *J. Cell Biol.*
138:913–926. doi:10.1083/jcb.138.4.913.

Müller, P.M., J. Rademacher, R.D. Bagshaw, C. Wortmann, C. Barth, J. van Unen, K.M. Alp, G.
Giudice, R.L. Eccles, L.E. Heinrich, P. Pascual-Vargas, M. Sanchez-Castro, L.
Brandenburg, G. Mbamalu, M. Tucholska, L. Spatt, M.T. Czajkowski, R.W. Welke, S.
Zhang, V. Nguyen, T. Rrustemi, P. Trnka, K. Freitag, B. Larsen, O. Popp, P. Mertins, A.C.
Gingras, F.P. Roth, K. Colwill, C. Bakal, O. Pertz, T. Pawson, E. Petsalaki, and O. Rocks.
2020. Systems analysis of RhoGEF and RhoGAP regulatory proteins reveals spatially
organized RAC1 signalling from integrin adhesions. *Nat. Cell Biol.* 22:498–511.
doi:10.1038/s41556-020-0488-x.

Nakamuta, S., Y.T. Yang, C.L. Wang, N.B. Gallo, J.R. Yu, Y. Tai, and L. Van Aelst. 2017. Dual
role for DOCK7 in tangential migration of interneuron precursors in the postnatal
forebrain. *J. Cell Biol.* 216:4313–4330. doi:10.1083/jcb.201704157.

Nguyen, T.T.T., W.S. Park, B.O. Park, C.Y. Kim, Y. Oh, J.M. Kim, H. Choi, T. Kyung, C.H. Kim, G.
Lee, K.M. Hahn, T. Meyer, and W. Do Heo. 2016. PLEKHG3 enhances polarized cell
migration by activating actin filaments at the cell front. *Proc. Natl. Acad. Sci. U. S. A.*
113:10091–10096. doi:10.1073/pnas.1604720113.

Omelchenko, T., A. Hall, and K. V. Anderson. 2020. β-Pix-dependent cellular protrusions
propel collective mesoderm migration in the mouse embryo. *Nat. Commun.* 11.
doi:10.1038/s41467-020-19889-1.

Omelchenko, T., M.A. Rabadan, R. Hernáandez-Martínez, J. Grego-Bessa, K. V. Anderson, and A. Hall. 2014. B-Pix Directs Collective Migration of Anterior Visceral Endoderm Cells in the Early Mouse Embryo. *Genes Dev.* 28:2764–2777. doi:10.1101/gad.251371.114.

Pestonjamasp, K.N., C. Forster, C. Sun, E.M. Gardiner, B. Bohl, O. Weiner, G.M. Bokoch, and M. Glogauer. 2006. Rac1 links leading edge and uropod events through Rho and myosin activation during chemotaxis. *Blood*. 108:2814–2820. doi:10.1182/blood-2006-01-010363.

Polak, R., M.B. Bierings, R. Pieters, M. Buitenhuis, and M.L. Den Boer. 2015. Small Molecule Inhibition of LARG/RhoA Signaling Blocks Migration of ETV6-RUNX1 Positive B-Cell Precursor Acute Lymphoblastic Leukemia. *Blood*. 126:1293–1293. doi:10.1182/blood.V126.23.1293.1293.

Sallese, M., S. Mariggiò, E. D'Urbano, L. Iacovelli, and A. De Blasi. 2000. Selective regulation of Gq signaling by G protein-coupled receptor kinase 2: Direct interaction of kinase N terminus with activated G(αq). *Mol. Pharmacol.* 57:826–831. doi:10.1124/mol.57.4.826.

Schmidt, M., B. Lohmann, K. Hammer, S. Haupenthal, M. Voß, C. Nehls, and K.H. Jakobs. 1998. G(i)-and protein kinase C-mediated heterologous potentiation of phospholipase C signaling by G protein-coupled receptors. *Mol. Pharmacol.* 53:1139–1148.

Shi, G.X., W.S. Yang, L. Jin, M.L. Matter, and J.W. Ramos. 2017. RSK2 drives cell motility by serine phosphorylation of LARG and activation of Rho GTPases. *Proc. Natl. Acad. Sci. U. S. A.* 115:E190–E199. doi:10.1073/pnas.1708584115.

Sroka, J., A. Antosik, J. Czyż, I. Nalvarte, J.M. Olsson, G. Spyrou, and Z. Madeja. 2007. Overexpression of thioredoxin reductase 1 inhibits migration of HEK-293 cells. *Biol. Cell*. 99:677–687. doi:10.1042/bc20070024.

Vaughan, E.M., A.L. Miller, H.Y.E. Yu, and W.M. Bement. 2011. Control of local Rho GTPase crosstalk by Abr (Current Biology (2011) 21 (270-277)). *Curr. Biol.* 21:623. doi:10.1016/j.cub.2011.03.053.

Yamamoto, K.I., H. Murata, E.W. Putranto, K. Kataoka, A. Motoyama, T. Hibino, Y. Inoue, M. Sakaguchi, and N.H. Huh. 2013. DOCK7 is a critical regulator of the RAGE-Cdc42 signaling axis that induces formation of dendritic pseudopodia in human cancer cells. *Oncol. Rep.* 29:1073–1079. doi:10.3892/or.2012.2191.

Yamauchi, J., Y. Miyamoto, J.R. Chan, and A. Tanoue. 2008. ErbB2 directly activates the exchange factor Dock7 to promote Schwann cell migration. *J. Cell Biol.* 181:351–365. doi:10.1083/jcb.200709033.

Yang, H.W., S.R. Collins, and T. Meyer. 2016. Locally excitable Cdc42 signals steer cells during chemotaxis. *Nat. Cell Biol.* 18:191–201. doi:10.1038/ncb3292.

Yang, Y., L. Liu, J. Cai, J. Wu, H. Guan, X. Zhu, J. Yuan, and M. Li. 2014. DEPDC1B enhances migration and invasion of non-small cell lung cancer cells via activating Wnt/β-catenin signaling. *Biochem. Biophys. Res. Commun.* 450:899–905. doi:10.1016/j.bbrc.2014.06.076.

Zhang, S., W. Shi, W. Hu, D. Ma, D. Yan, K. Yu, G. Zhang, Y. Cao, J. Wu, C. Jiang, and Z. Wang. 2020. DEP domain-containing protein 1B (DEPDC1B) promotes migration and invasion in pancreatic cancer through the Rac1/PAK1-LIMK1-cofilin1 signaling pathway. *Onco. Targets. Ther.* 13:1481–1496. doi:10.2147/OTT.S229055.
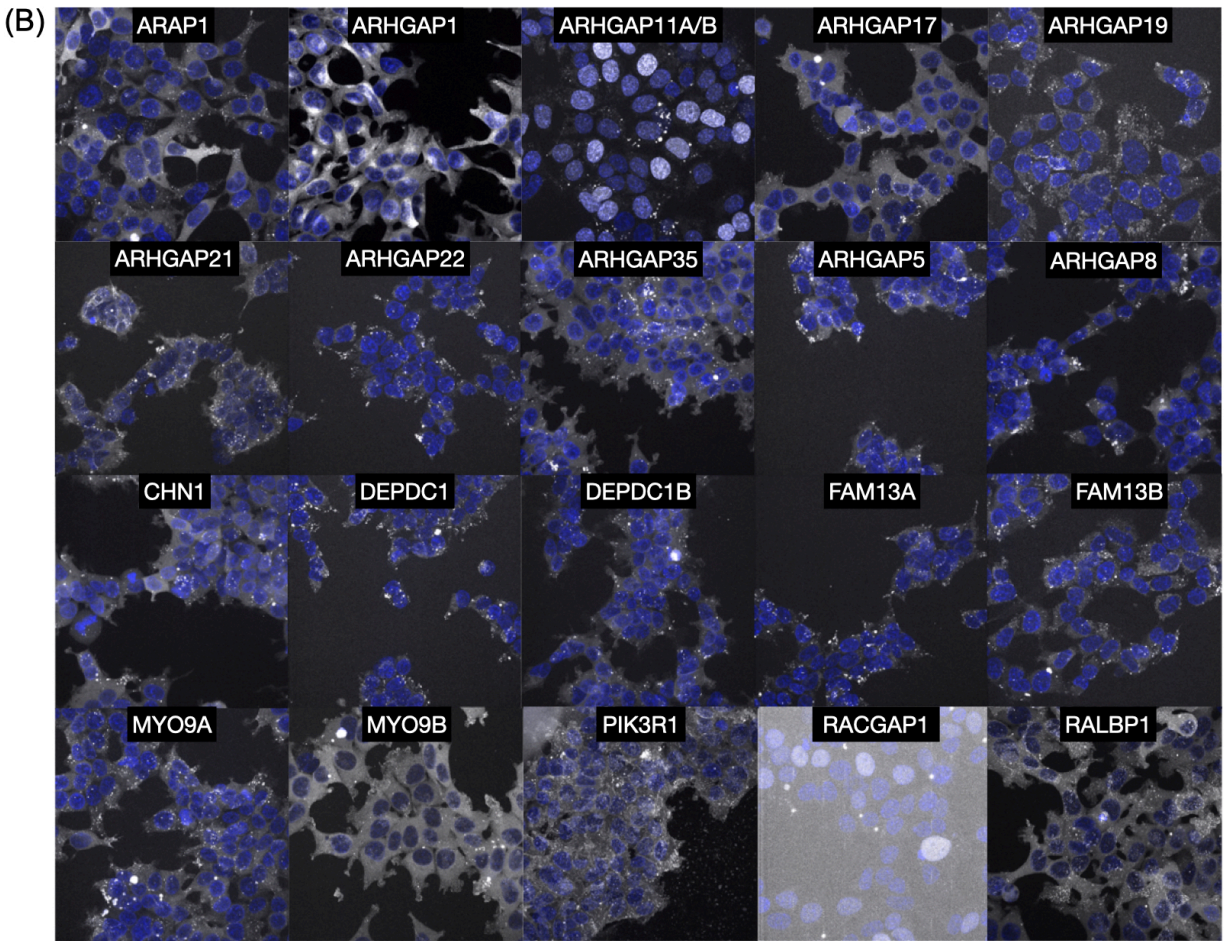
Figure 4.1

(A)
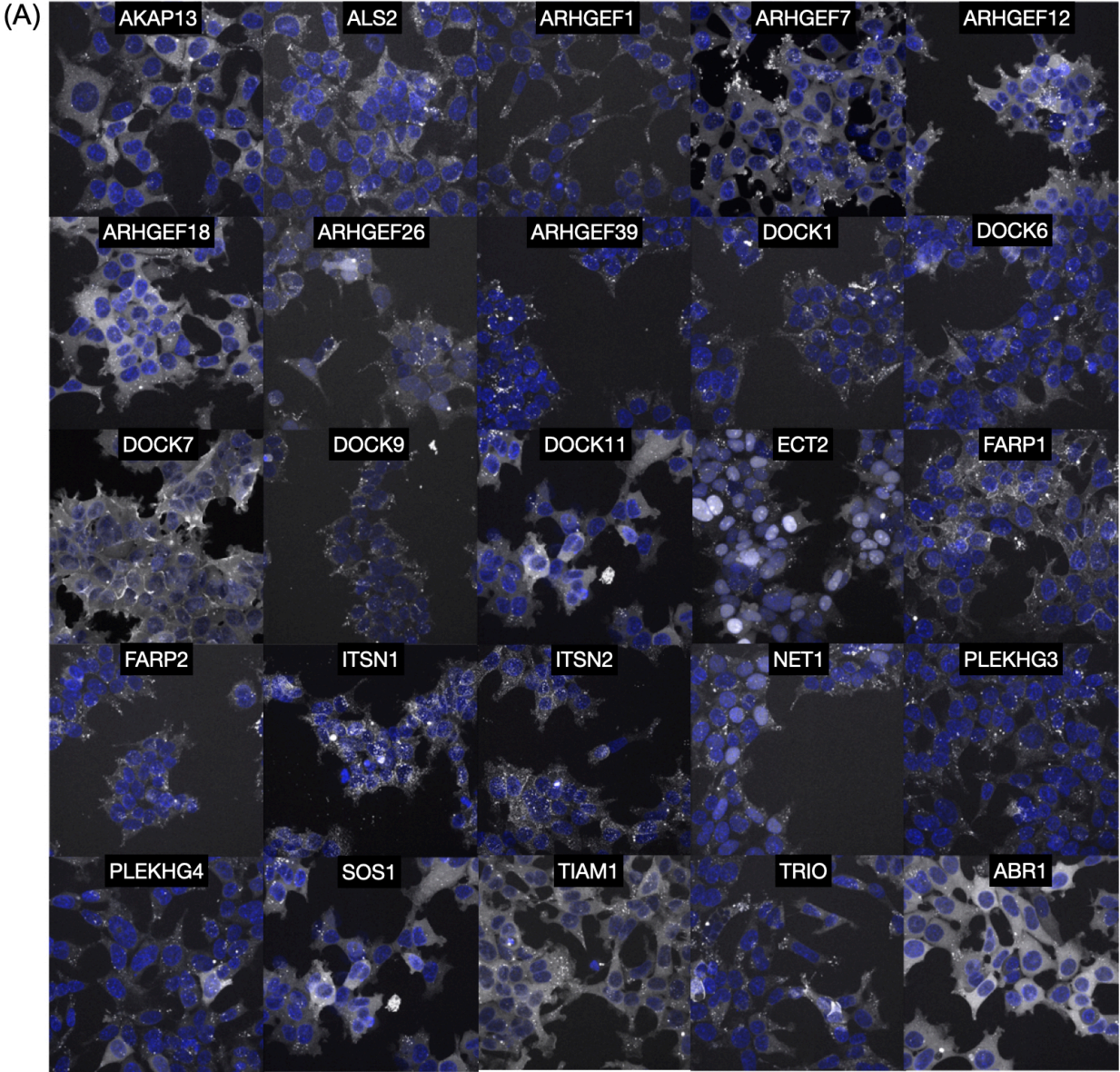
Figure 4.1 Localization of endogenously tagged Rho GEFs (A) and GAPs (B) in HEK293T cells.
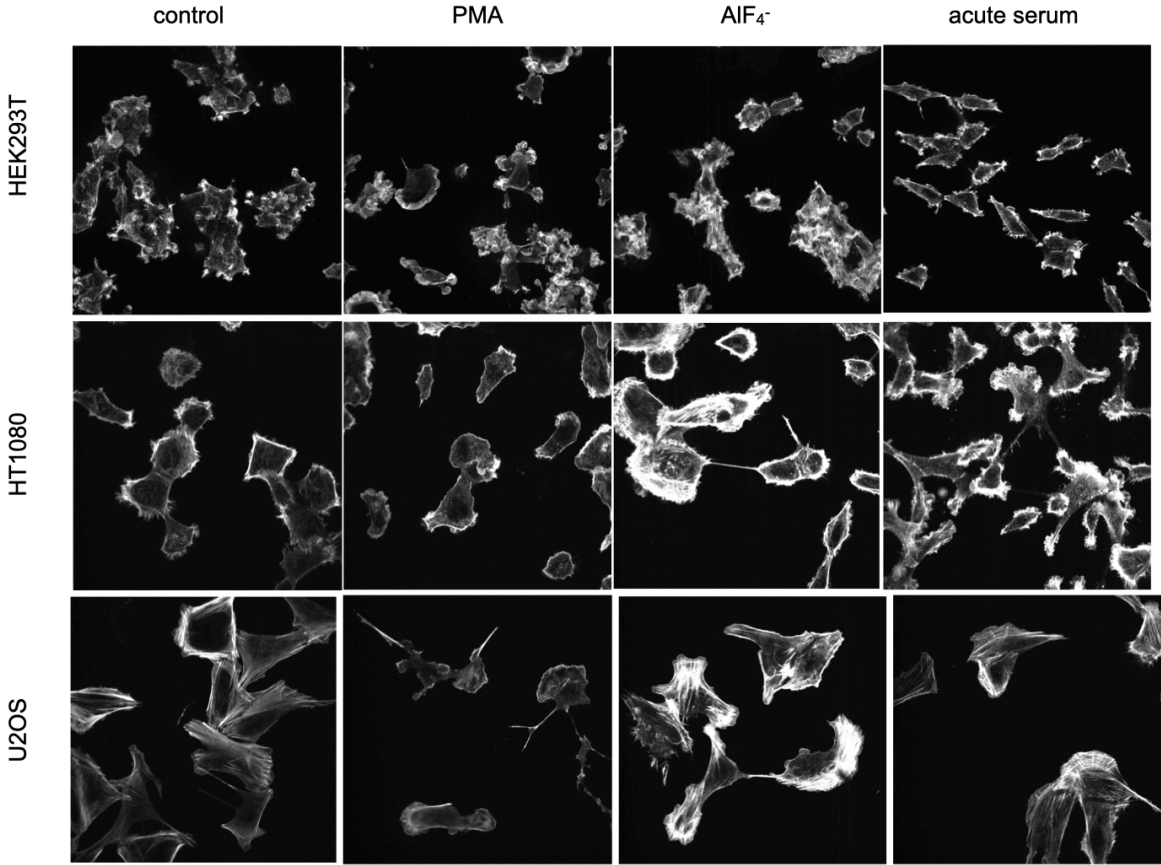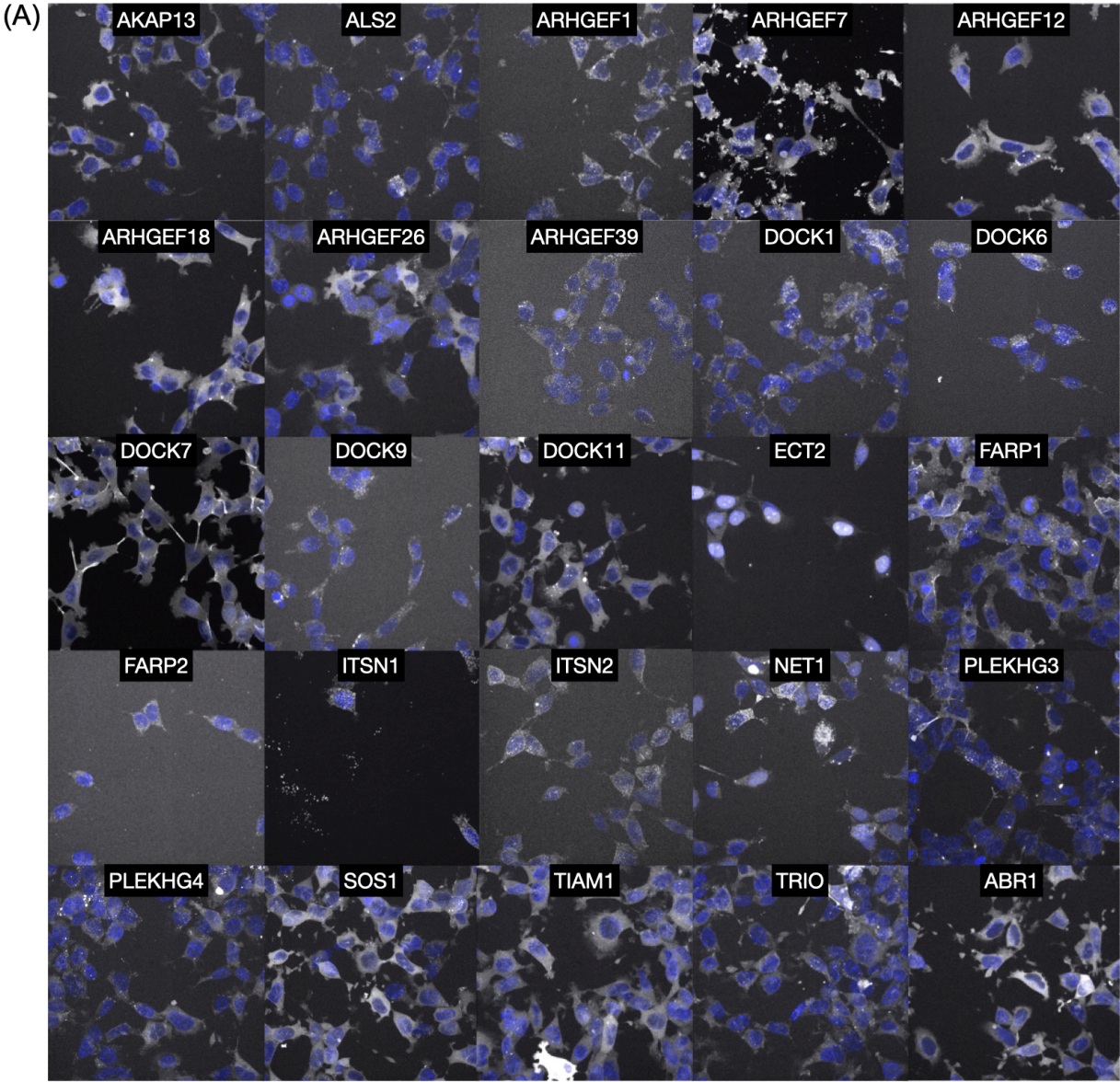
Figure 4.2

Figure 4.2 Phalloidin staining of HEK293T, HT1080, and U2OS cells treated with stimulatory signals highlight the ability of these cells to polarize and form actin-rich protrusions.
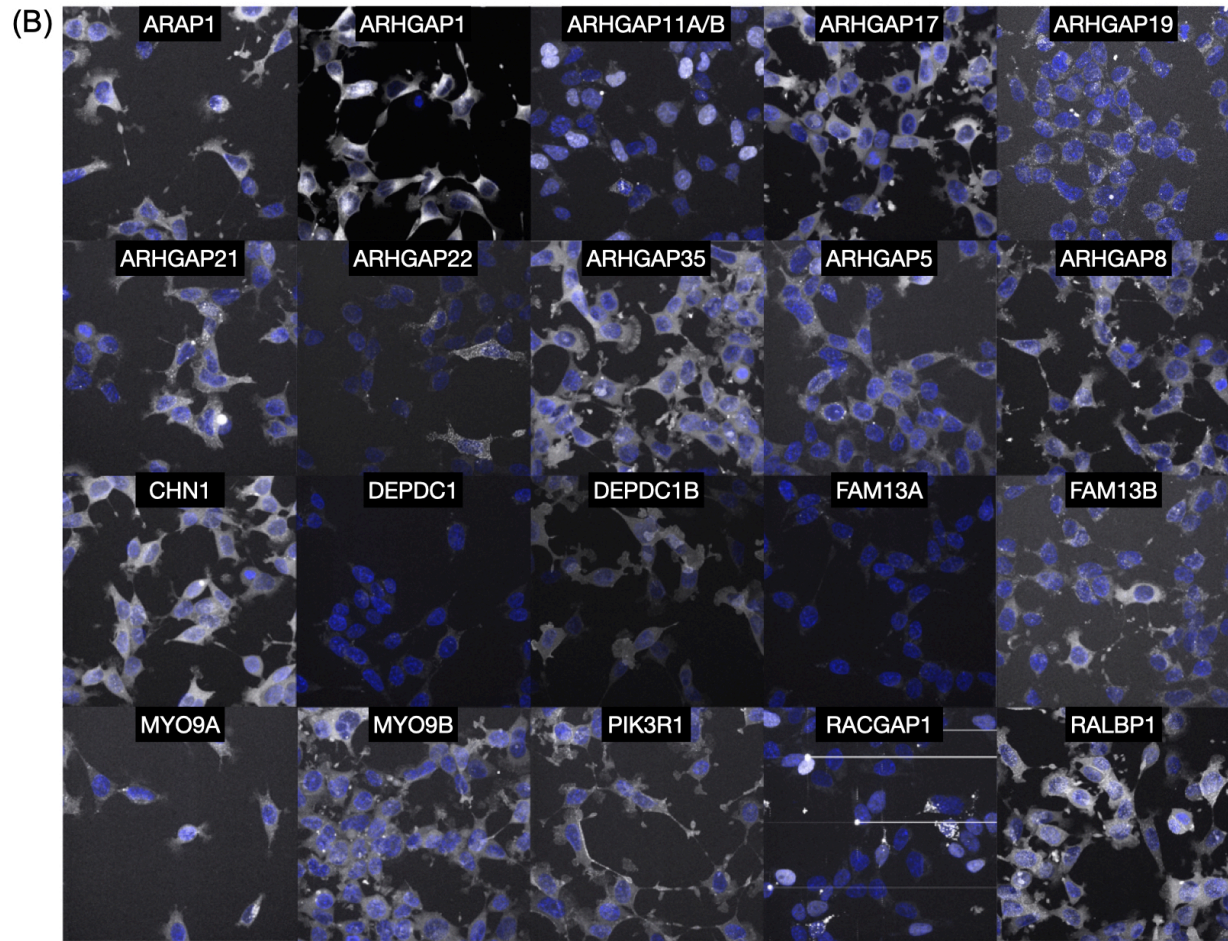
Figure 4.3

(A)

Figure 4.3 Localization of endogenously tagged Rho GEFs (A) and GAPs (B) in HEK293T cells treated with 300 nM PMA.
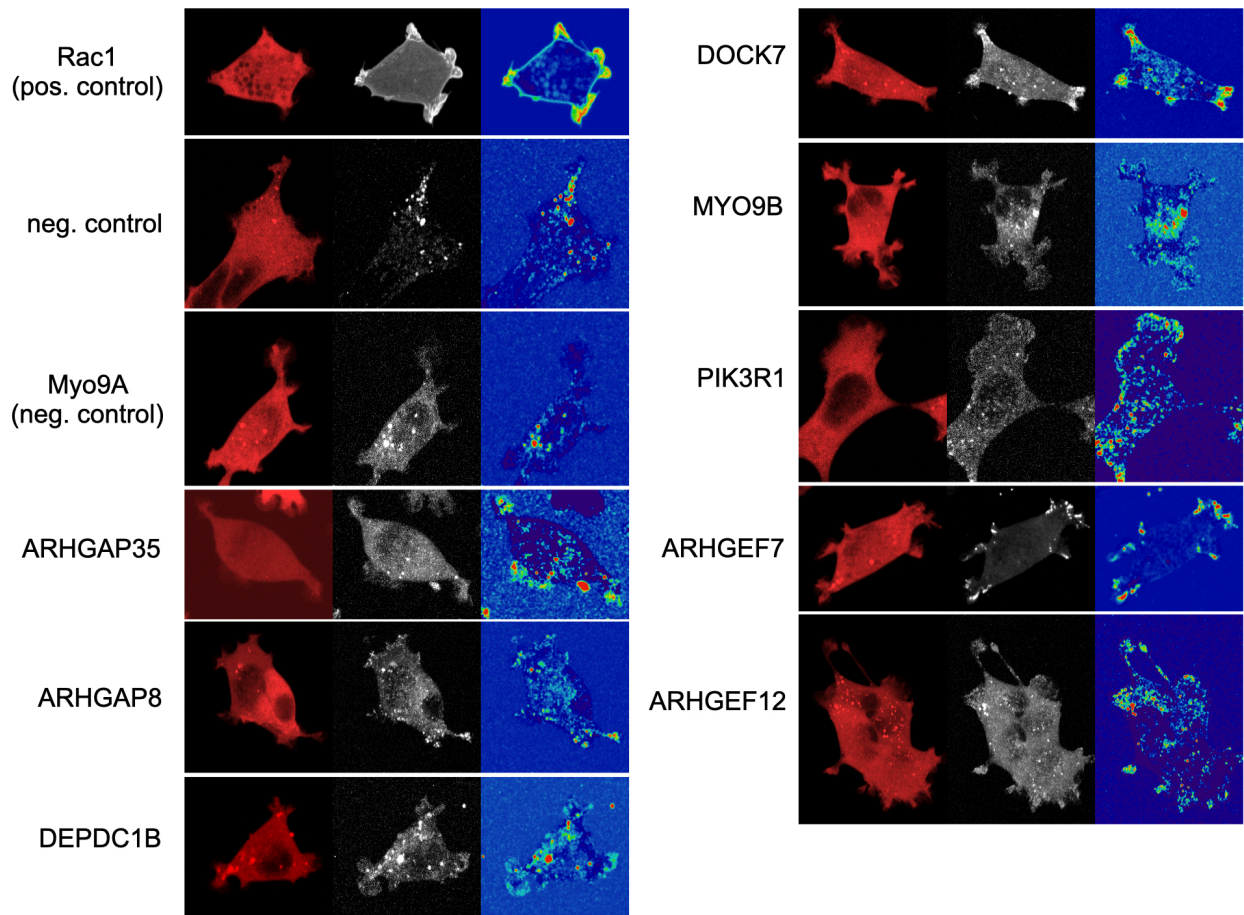
Figure 4.4

Figure 4.4 Normalization of endogenous protein signal to a cytosolic marker highlights membrane or protrusion enrichment of target GEFs and GAPs.

Rac1, a GTPase involved in protrusion generation, is shown as a positive control. We also provide a negative control that has no knock-in fluorescence as well as a negative control where tagging worked, but the protein of interest is not enriched to the membrane or to protrusions (MYO9A). Images of our eight final candidates are shown here: ARHGAP35, ARHGAP8, DEPDC1B, DOCK7, MYO9B, PIK3R1, ARHGEF7, and ARHGEF12

Figure 4.5

(A)

negative control, no PMA   negative control, 300nM PMA   Rac1 population KO, 300nM PMA

(B)
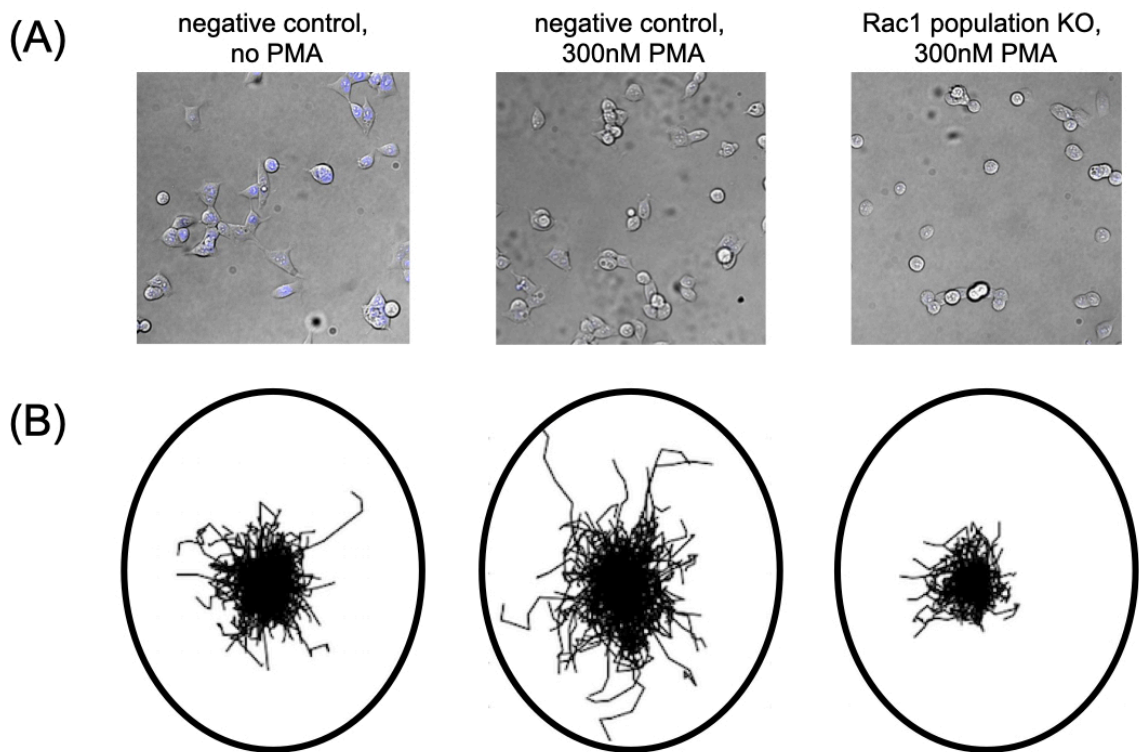
Figure 4.5 Example of phenotyping migration defects in PMA-treated HEK293T cells.

(A) Insets of HEK293T cells +/- 300 nM PMA as well as a PMA-treated population level knockout of Rac1, a known contributor to protrusion generation. Cell nuclei are labeled with NucBlue dye for tracking.

(B) Worm plots showing the trajectories of nuclei tracked over four hours of migration. PMA treatment induces motility of HEK293T cells, but this effect is lost when the migration machinery is compromised, here Rac1.

Table 4.1

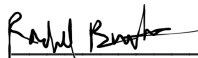| Gene	HEK293T TPM	GEF or GAP	Quality	Normalization Screened	Final Candidate
ARAP1	39.6	GAP	PASS	YES	NO
ARHGAP1	19.8	GAP	PASS	YES	NO
ARHGAP11A/B	57.7	GAP	PASS	YES	NO
ARHGAP17	54.8	GAP	PASS	YES	NO
ARHGAP19	23.7	GAP	PASS	NO	NO
ARHGAP21	27.4	GAP	PASS	YES	NO
ARHGAP22	18.1	GAP	PASS	YES	NO
ARHGAP25	21.9	GAP	FAIL	NO	NO
ARHGAP35	22.3	GAP	PASS	YES	YES
ARHGAP5	31.2	GAP	PASS	NO	NO
ARHGAP8	35.9	GAP	PASS	YES	YES
CHN1	21.4	GAP	PASS	YES	NO
DEPDC1	68.1	GAP	PASS	NO	NO
DEPDC1B	28.6	GAP	PASS	YES	YES
FAM13A	16.3	GAP	PASS	NO	NO
FAM13B	15.3	GAP	PASS	YES	NO
MYO9A	16.6	GAP	PASS	YES	NO
MYO9B	25.9	GAP	PASS	YES	YES
PIK3R1	10	GAP	PASS	YES	YES
RACGAP1	81	GAP	PASS	YES	NO
RALBP1	41.1	GAP	PASS	YES	NO
AKAP13	17	GEF	PASS	YES	NO
ALS2	19.2	GEF	PASS	NO	NO
ARHGEF1	34.1	GEF	PASS	NO	NO
ARHGEF7	27.3	GEF	PASS	YES	YES
ARHGEF12	37	GEF	PASS	YES	YES
ARHGEF18	20.5	GEF	PASS	YES	NO
ARHGEF26	15.5	GEF	PASS	YES	NO
ARHGEF39	24.8	GEF	PASS	NO	NO
DOCK1	18.4	GEF	PASS	NO	NO
DOCK6	15	GEF	PASS	YES	NO
DOCK7	62.1	GEF	PASS	YES	YES
DOCK9	18.5	GEF	PASS	NO	NO
DOCK11	10.8	GEF	PASS	YES	NO
ECT2	51.3	GEF	PASS	YES	NO

Gene	HEK293T TPM	GEF or GAP	Quality	Normalization Screened	Final Candidate
FARP1	22.2	GEF	PASS	YES	NO
FARP2	35.3	GEF	PASS	NO	NO
ITSN1	38.2	GEF	PASS	YES	NO
ITSN2	18.7	GEF	PASS	YES	NO
NET1	38.3	GEF	PASS	YES	NO
PLEKHG3	23.7	GEF	PASS	NO	NO
PLEKHG4	17.4	GEF	PASS	YES	NO
SOS1	22.8	GEF	PASS	YES	NO
TIAM1	19.1	GEF	PASS	YES	NO
TRIO	25.9	GEF	PASS	YES	NO
ABR	29.1	BOTH	PASS	YES	NO
BCR	48	BOTH	FAIL	NO	NO

Publishing Agreement

It is the policy of the University to encourage open access and broad distribution of all theses, dissertations, and manuscripts. The Graduate Division will facilitate the distribution of UCSF theses, dissertations, and manuscripts to the UCSF Library for open access and distribution. UCSF will make such theses, dissertations, and manuscripts accessible to the public and will take reasonable steps to preserve these works in perpetuity.

I hereby grant the non-exclusive, perpetual right to The Regents of the University of California to reproduce, publicly display, distribute, preserve, and publish copies of my thesis, dissertation, or manuscript in any form or media, now existing or later derived, including access online for teaching, research, and public service purposes.

_____
Author Signature

6/9/2021
_____
Date